uOttawa

L'Université canadienne
Canada's university

FACULTÉ DES ÉTUDES SUPÉRIEURES ET POSTOCTORALES

uOttawa

L'Université canadienne
Canada's university

FACULTY OF GRADUATE AND POSDOCTORAL STUDIES

Philip Andrew Corber
AUTEUR DE LA THÈSE / AUTHOR OF THESIS

M.A.Sc. (Mechanical Engineering)
GRADE / DEGREE

School of Information Technology and Engineering
FACULTÉ, ÉCOLE, DÉPARTEMENT / FACULTY, SCHOOL, DEPARTMENT

The Performance of a Pressure Atomizer with a Flow Obstruction Upstream of the Nozzle
TITRE DE LA THÈSE / TITLE OF THESIS

Stavos Tavoularis
DIRECTEUR (DIRECTRICE) DE LA THÈSE / THESIS SUPERVISOR

CO-DIRECTEUR (CO-DIRECTRICE) DE LA THÈSE / THESIS CO-SUPERVISOR

EXAMINATEURS (EXAMINATRICES) DE LA THÈSE / THESIS EXAMINERS

M. Johnson

R. Milane

Gary W. Slater
Le Doyen de la Faculté des études supérieures et postdoctorales / Dean of the Faculty of Graduate and Postdoctoral Studies

The Performance of a Pressure Atomizer with a Flow Obstruction Upstream of the Nozzle

By

P. Andrew Corber

A thesis presented to the
Faculty of Graduate and Postdoctoral Studies
in partial fulfillment of the
requirements for the degree of

MASTER OF APPLIED SCIENCE
in
MECHANICAL ENGINEERING

Ottawa-Carleton Institute for Mechanical and Aerospace Engineering
Department of Mechanical Engineering
University of Ottawa
Ottawa, Ontario, Canada

May 2009

Your file Votre référence
ISBN: 978-0-494-61203-3
Our file Notre référence
ISBN: 978-0-494-61203-3

Abstract

The internal flow and the spray formed by a pressure atomizer with an orifice diameter of 1 mm and a length to diameter ratio of 10 were studied at injection pressures between 70 and 5000 kPa. Obstructions to flow were also introduced inside the injector to examine their effect on the injector's performance. Visualization of the flow inside the injector indicated that the obstructions caused the flow to cavitate. However, even without any obstruction, cavitation occurred at injection pressures as low as 170 kPa. These results also showed that cavitation can occur in four different modes, depending on the mass flow rate of fuel through the nozzle and the type of obstruction. Images of the resulting spray indicated that the cavitation enhances atomization significantly. Single-component phase Doppler particle analysis and laser diffraction particle sizing were conducted 50 mm, 100 mm and 150 mm downstream of the nozzle face to examine the size and velocity distributions of the droplets in the spray. These measurements indicated that for a given liquid flow rate the droplet size was not affected by the structure of the cavitation. Velocity measurements in the spray indicated that the cavitation produces a wider spray cone angle at lower mass flow rates.

Acknowledgements

I would like to express my thanks to my thesis supervisor Professor Tavoularis for his direction, advice and patience throughout this work. His guidance has been invaluable in completing my thesis. I also thank my thesis examiners, Professors Roger Milane and Matthew Johnson, for their valuable comments on an earlier version of the thesis.

The financial and technical support of the National Research Council of Canada's Gas Turbine Laboratory is gratefully acknowledged, with special thanks to Mike Player and Michel Charbonneau. Without their assistance and technical expertise this work could not have been completed. I would also like to thank the three musketeers, Ali Mahallati, Mike Benner and George Zhang for their help.

Finally, I would like to thank Wajid Chishty, whose door was always open.

Contents

Nomenclature

A	area
b_n	constant in Fourier series expansion
C_c	contraction coefficient
C_d	discharge coefficient
d	jet diameter
D	droplet diameter and diameter of orifice
d_f	distance between PDPA probe volume fringes
E_s	potential surface energy
K	cavitation parameter
L	length of orifice
n	integer
m	mass flow
Oh	Ohnesorge number
P	pressure
q	growth rate of a disturbance
R	radius
Re	Reynolds number
u	velocity
We	Weber number
Z	breakup length

Greek Symbols

σ	liquid surface tension
γ	dimensionless wave number
λ	wavelength of a disturbance on the surface of the liquid jet
δ_o	amplitude of a disturbance
ρ	density
μ	viscosity
Δ	denotes a finite difference
θ_b	angle between PDPA beams
θ_s	angle of scattered light from PDPA probe volume
ψ	angle of elevation of PDPA detector
Φ	Phase

Subscripts

air	denotes an air property
crit	denotes critical condition
eff	denotes an effective value
liq	denotes a liquid property
m	maximum
vap	denotes a vapour property

Acronyms

AHFSF	Atmospheric High Flow Spray Facility
CCA	Constant Current Anemometer
CPL	Canadian Photonics Lab
CTA	Constant Temperature Anemometer
CVA	Constant Voltage Anemometer
HCA	Half Cone Angle
ICLASS	International Conference on Liquid Atomization and Spray Systems
LDV	Laser Doppler Velocimetry
PDPA	Phase Doppler Particle Analyzer
SDL	Spray Dynamics Lab

List of Tables

List of Figures

Chapter 1 - Introduction

Sprays are at the core of many the world's energy production systems, they are used in the engines of our planes, trains and automobiles, and they are utilized to dispense liquids in a multitude of domestic and industrial applications on a daily basis. Around the house they are used for painting, cooling, misting, cleaning, washing, coating and lubricating. They are further used in a variety of combustion systems, agriculture, food processing, medicine and numerous industrial processes. In nature sprays can be seen in the forms of clouds, waterfalls and rain (Lefebvre, 1989).

Despite the importance of sprays, the science of sprays and atomization is relatively new. Fourty years ago there were no text books, conferences, journals or university courses devoted to spray technology (Chigier, 2006). That is not to say that there was no research on the subject; the behaviour of liquid columns has been studied for nearly two hundred years. Much has changed in the last two decades as there is now an international conference on the subject (ICLASS – International Congress on Liquid Atomization and Spray Systems) and a Journal of Atomization and Sprays, with large numbers of scientists and engineers researching various spray phenomena from spray interaction to single droplet dynamics.

Perhaps the lack of formal academic acceptance of this subject through most of the last century is due to the common misconception that producing a spray is simple: pressurize a liquid in a tank and then force it through a small opening. Certainly in many situations this is no doubt true. Around the house, for example, the dispensing of a cleaning solution to a dirty surface is done efficiently using a spray bottle; this is an

application of little academic value with no need for an engineering analysis. In many circumstances, however, the performance of the spray must be tightly controlled. Toxic waste incineration, for example, requires 99.999% combustion efficiency. The generation of even a few large droplets by the injector could result in a shut-down of the incinerator to prevent release of unacceptable amounts of pollutants. Other very challenging areas for spray control include combustion systems, medical devices such as inhalers, agricultural crop dusting, and industrial coating processes such as painting.

Another factor that may have also been responsible for limiting the scientific attention to sprays is the difficulty in characterizing them. Fourty years ago there were no tools for efficiently examining spray features such as droplet size and velocity. Spray quality was often assessed by eye. Two enabling technologies emerged in the 1980s, which have allowed for drastic advancements in the study and understanding of sprays: optical diagnostics and computational fluid dynamics. The former allows for detailed measurements of droplet size, velocity, number density, mass flux, liquid and vapour distribution as well as temperature and gas concentration. The latter, along with the advent of supercomputers, have been valuable in assessing the importance of various input parameters, and in providing some insight into problems for which measurements are too difficult and/or expensive. Imaging still remains an essential method to determine overall spray qualities. Significant advances in digital photography have also helped, allowing images of sprays to be taken with exposures of durations of a few nanoseconds. The results achieved from the combined application of non-intrusive diagnostics and numerical simulations have brought the study of sprays to the forefront of scientific

interest. Recently, the U.S. Argonne National Laboratory investigated the near-nozzle region of a diesel spray using X-ray instrumentation valued at one billion dollars.

It is not too surprising to see the growth of interest in sprays, if one considers the large number of industries in which they play a role. Despite the wide range of applications for sprays, historically the bulk of the research efforts on the subject have been focused on fuel injection for combustion systems such as gas turbines and diesel engines. This trend is changing slowly; at the last ICLASS in Kyoto in 2006, of the 300 papers presented almost 30% were related to combustion. Further promoting this trend in the research are the environmental implications of burning liquid fuels. Climate change has become a major global concern, and, with atmospheric pollution being suspected as the root cause, much attention is being given to the sprays employed in combustion systems in an attempt to reduce harmful emissions such as nitrous oxides and soot. This, combined with the daily growth of global need for electrical and mechanical power and the ever increasing price of crude oil, is forcing society to maximize the potential of our fuel supplies. With the spray playing such a large role in many of these systems, this trend will likely continue.

Being able to control the size and velocity of the droplets produced by an injector is critical to the performance of the overall system. In combustion systems, for example, it is preferable that the droplet size and breakup length be as small as possible so that the air and fuel can mix to the appropriate stoichiometry and burn in an efficient and clean manner. In other applications, such as manufacturing, it is necessary that the fluid column remain intact so that the necessary lubricating film is produced on the surface of the part. Agricultural sprays are somewhere in between. For this application it is

important that the droplets be large enough to resist transport and dispersion by the wind, to avoid unwanted drift of insecticides to neighbouring crops.

The breakup process of the liquid column into droplets is very important to the quality of the spray. It depends on many parameters, including the nozzle geometry, the jet velocity as well as the physical properties of the liquid and the surrounding gas. Liquid flow characteristics, such as turbulence and cavitation, can also play significant roles in the breakdown of the bulk liquid into droplets. The latter has been examined in detail over the last two decades; however it is difficult to separate the two because the formation and collapse of cavitation bubbles produces turbulence and, conversely, high-intensity turbulence may induce cavitation.

Typically the management of droplet size and velocity is done by selecting an appropriate atomizer for the application. However, for many systems the best possible injector can not be used due to high cost and/or complexity. Consequently, control over all or at least some of the spray parameters must be achieved by nozzle design. With a better understanding of how the internal nozzle flow affects the spray, atomizers can be designed more efficiently to produce the desired spray characteristics and consequently improve the performance of the overall system.

The objective of the present research is to expand the available experimental database on the effects of the flow characteristics of the liquid inside the nozzle on the properties of the generated spray.

Chapter 2 - Literature Review

2.1 Classical Theory of Atomization

When liquid exits a round orifice into air or other gas, it forms a nearly cylindrical column. The study of the dynamics of liquid columns has attracted interest for almost 200 years in the context of a great variety of technical applications, including, for example, fire-hose nozzles and steel teeming practice (McCarthy and Molloy, 1974). The first quantitative experiments on the break-up of a liquid jet were performed by Savart (1833). He observed a liquid column as seen in Figure 2.1 and put forward the following hypotheses:

1. If the diameter of the orifice remains constant, the break up length of the liquid column is proportional to its velocity.

2. If the velocity of the jet remains constant, the break up length is proportional to the orifice diameter.

Figure 2.1: Liquid column break-up as observed by Savart (1833).

Plateau (1873) is cited as being the first to investigate theoretically the stability of a liquid column. He showed that a static cylindrical column of liquid would be unstable if its length exceeded its perimeter because in such case two drops could be formed whose total surface area would be less than that of the cylinder. This theory helped to explain Savart's results, and is considered to be the foundation for Rayleigh's theory.

Lord Rayleigh performed a mathematical analysis of a liquid column, and the conditions which would cause it to collapse due to small disturbances. In his first work (Rayleigh, 1878); he examined an inviscid jet in a vacuum, which closely simulates a low speed water jet in air. He calculated the potential energy of the disturbed jet taking as reference the equilibrium state as

$$E_s = \frac{\pi\sigma}{2d}\left(\gamma^2 + n^2 - 1\right)b_n^2 \qquad (2.1)$$

where E_s is the potential surface energy, σ is the surface tension of the liquid, d is the jet diameter, b_n is a constant in the Fourier series expansion, n is an integer and γ is a dimensionless wave number, defined as

$$\gamma = \frac{\pi d}{\lambda} \qquad (2.2)$$

where λ is the wavelength of the disturbance. The system would be unstable if E_s were negative. This requires $n = 0$ and $\gamma < 1$ giving the result that the jet will break down if $\lambda > \pi d$. It can be concluded from this that, for a laminar inviscid jet, a disturbance will grow if it is greater than the circumference of the column.

Rayleigh extended the theory to predict the growth rate of the disturbance and the distance over which the column would remain continuous. By calculating the kinetic energy per unit length associated with the disturbed surface and combining this with

equation (2.1) where, $n = 0$, $\gamma < 1$ and $b_n^2 \propto e^{(qt)}$ where q is the growth rate of the disturbance, he was able to show that the maximum growth rate is

$$q_m = 0.97\sqrt{\frac{\sigma}{\rho_L d^3}} \tag{2.3}$$

and that the break up length Z is

$$\frac{Z}{d} = 1.03u\left(\ln\frac{d}{2\delta_o}\right)\sqrt{\frac{\rho_L d}{\sigma}} \tag{2.4}$$

where δ_o is the amplitude of infinitesimal disturbance and ρ_L is the density of the liquid. The wavelength of the disturbance corresponding to q_m is

$$\lambda_m = 4.51d \tag{2.5}$$

After the jet breaks up, the segment of the column with a length of $4.51d$ will form a droplet with the same volume, such that

$$4.51d \times \frac{\pi}{4}d^2 = \frac{\pi}{6}D^3 \tag{2.6}$$

$$D = 1.89d \tag{2.7}$$

where D is the droplet diameter.

Equation (2.7) was later supported by the work of Taylor (1963). He examined a disintegrating jet and measured the frequency at which the drops formed. By relating this to the wavelength of the disturbance with the fastest rate of growth, and by using an argument similar to that used to derive equation (2.6), he found the expressions

$$\lambda_m = 4.69d \tag{2.8}$$

$$D = 1.92d \tag{2.9}$$

Rayleigh (1892) attempted to extend his theory to viscous jets. The result was a complicated expression for q, with no useful equations resulting from the work. It was Weber (1931) who was able to extend Rayleigh's theory to include viscous jets.

Weber theorized that if the initial disturbance is small enough the surface tension forces will dampen the motion of the jet. If however, the oscillation is large enough the surface tension forces will increase the disturbance and will cause the jet to break up. Weber's mathematical analysis modeled the jet as mean flow with disturbances overlaying it. For a symmetrical disturbance and using Rayleigh's argument of $\gamma < 1$, along with neglecting small terms, he expressed the maximum rate of growth and break up length as:

$$q_m = \frac{1}{\sqrt{\frac{\rho_L d^3}{\sigma}} + \frac{3\mu d}{\sigma}} \tag{2.10}$$

$$Z = u\left(\ln\frac{d}{2\delta_o}\right)\left(\sqrt{\frac{\rho_L d^3}{\sigma}} + \frac{3\mu d}{\sigma}\right) \tag{2.11}$$

where μ is the viscosity of the liquid. Note that equation 2.10 and 2.11 reduce to a very similar form as equation 2.3 and 2.4 for an inviscid jet. For his efforts, the dimensionless number relating the viscous forces of the liquid to the surface tension was named for him.

$$We = \frac{\rho_L u_L^2 d}{\sigma} \tag{2.12}$$

The experimental compliment to Weber's theory was provided by Haenlein (1932). His experiments examined the liquid jets with fluids of various viscosities and surface tensions. The results helped support Weber's analysis, and allowed Haenlein to identify four distinct break up regimes:

1. Drop formation without the influence of air. The formations of radialy symmetric waves are present in this regime, and there is a linear relationship between the jet velocity and the jet break up length.
2. Drop formation with the influence of air. Once the jet velocity reaches a critical level the aerodynamic forces amplify the disturbances produced in the regime 1.
3. Drop formation due to waves. As the aerodynamic forces continue to increase, relative to the surface tension the jet develops waves which in turn break and produces droplets.
4. Atomization. The jet is completely unstable and disintegrates in a chaotic manner.

While it can be easy to classify qualitatively which of the above states a liquid jet may be in, there was no quantitative way of separating them until the landmark achievement of Ohnesorge (1936). Ohnesorge reviewed the photographic data, and by dimensional analysis determined that the break up regimes could be classified into three groups depending on the Reynolds number of the flow. The stability number, which is named for him, is the Weber number divided by the Reynolds number:

$$Oh = \frac{\sqrt{\frac{u_L^2 \rho_L d}{\sigma}}}{\frac{u_L^2 \rho_L d}{\mu_L}} = \frac{\mu_L}{\sqrt{\rho_L \sigma d}} \qquad (2.13)$$

An Ohnesorge chart, shown in Figure 2.2, shows the three regimes proposed. It is important to note that Oh will be constant if the liquid and injector remain the same. As a result, the regimes are classified by Reynolds number. At low Reynolds number the jet breaks up via the Rayleigh mechanism. At intermediate Reynolds numbers oscillations in the liquid are observed, similar to regimes 2 and 3 in Henlein's classification scheme.

If the flow has a high Reynolds number the atomization will occur a short distance downstream from the injector exit. The dashed line on the Ohnesorge chart was added by Miesse (1955). His experimental results for the transition between Ohnesorge's second and third regimes were found to be described by

$$Oh = 1000\,\mathrm{Re}^{-0.92} \tag{2.14}$$

Reitz (1978) further improved the Ohnesorge chart by giving it four distinct regimes based on Weber number. Reitz's definition of Weber number is different for the one presented previously, as it uses the density of the air rather than that of the liquid:

$$We = \frac{\rho_A u_L^2 d}{\sigma} \tag{2.15}$$

The conclusions of Reitz are summarized in Table 2.1. Table 2.2 offers a summary, and graphical representation of the various break up regimes.

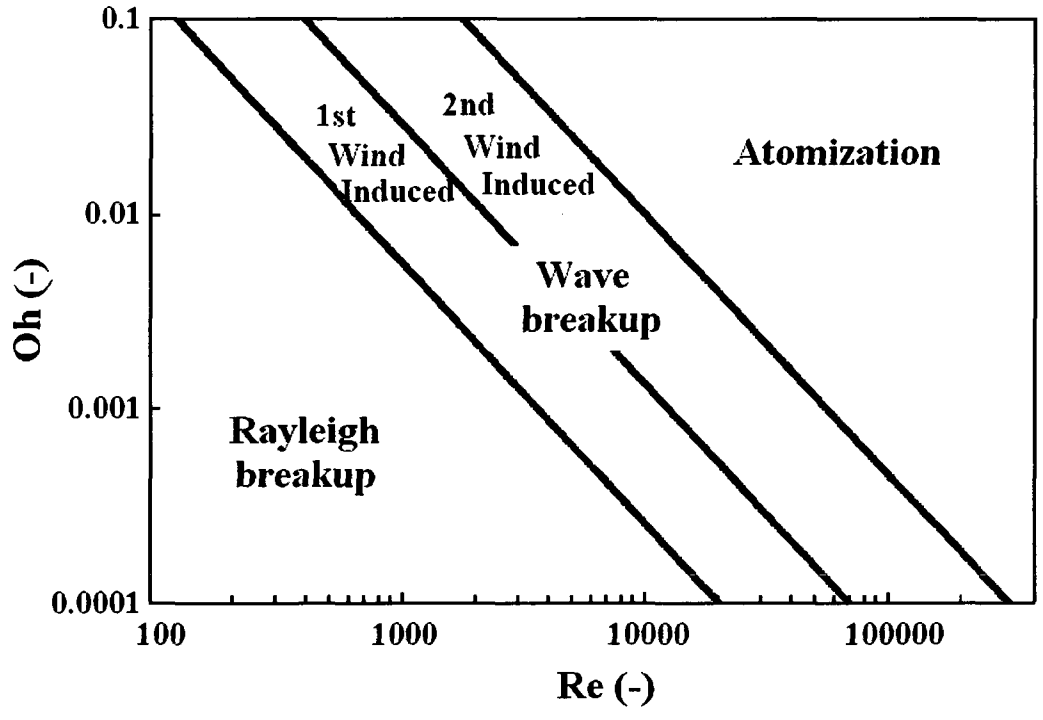

Figure 2.2: Ohnesorge Chart, classifying the disintegration regimes in terms of Ohnesorge and Reynolds numbers (Reitz,1978).

Regime	Description	Drop Formation Mechanism	Drop Size	Criteria for Transition
1	Rayleigh break-up	Surface tension force	> d	We > 0.4
2	First wind induced	Surface tension force and pressure of ambient air	~ d	
3	Second wind induced	Dynamic pressure of ambient air opposed by surface tension force initially	< d	We > 40.3 We > 13
4	Atomization	Unknown	<< d	

Table 2.1: Summary of conclusions made by Reitz (1978).

Spray regime	Picture	Illustration	Predominant drop formation mechanism	Transition to next regime
(1) Rayleigh breakup		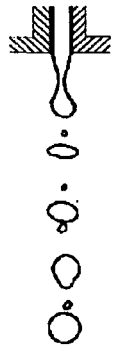	Surface tension force	We > 0.4
(2) First wind-induced breakup	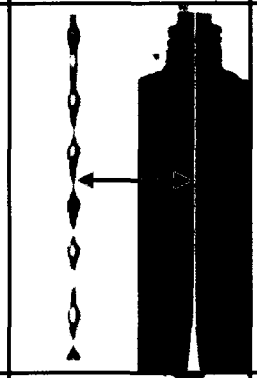		-Surface tension force -Dynamic pressure of ambient air	
(3) Second wind-induced breakup	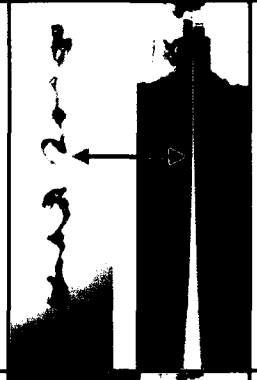		-Surface tension force -Dynamic pressure of ambient air opposed by surface tension force initially	We > 40.3
(4) Atomization			-Aerodynamic and shear forces -Turbulence -Expension -Surface tension force initially	We → ∞

Table 2.2: Classification of the disintegration regimes (Berrocal, 2006).

2.2 Jet Stability Curve

The work of many researches has helped to formulate Figure 2.3. It is interesting to note that the four sections of the plot correlate well with those proposed by Haenlein.

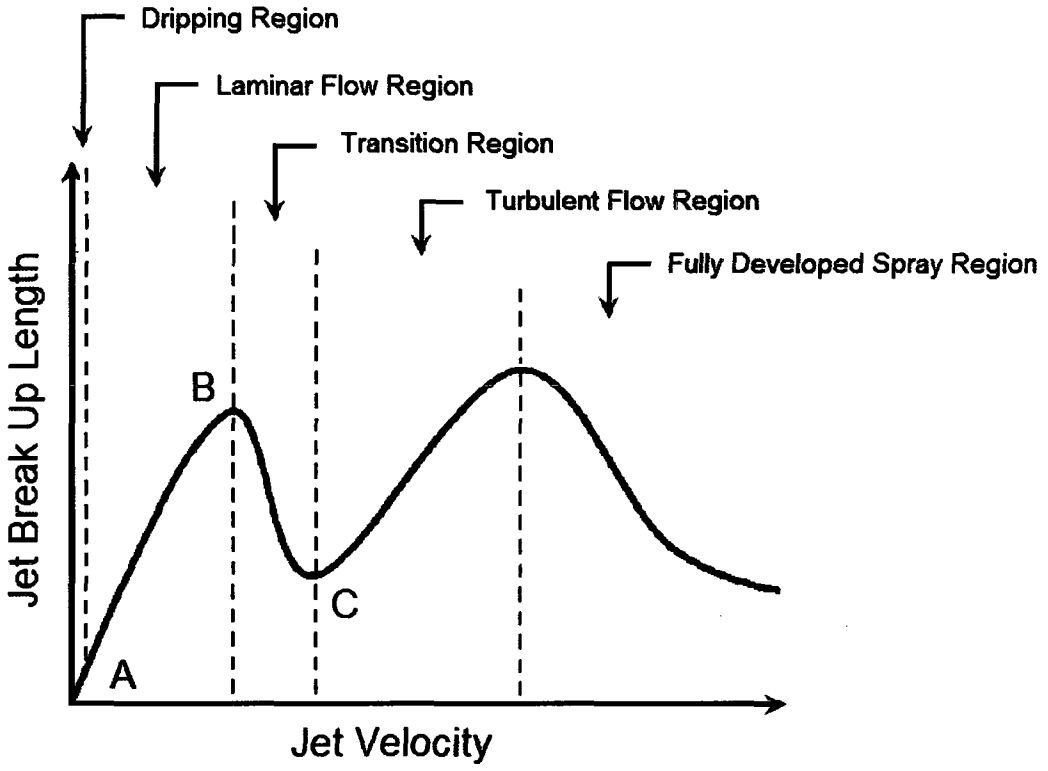

Figure 2.3: Stability curve showing the change in break up length with jet velocity.

Point A represents the transition from a dripping flow to a column flow and is of little importance for the given work. In this region, the break up length varies linearly with jet velocity and the work of Rayleigh (1892) and Weber (1931) applies. Unfortunately, the majority of the experimental evidence does not support equation (2.11). Mahoney and Sterling (1978) improved upon Weber's prediction of the break up length by including a function of Oh and We. As shown in Figure 2.4, this equation has an excellent correlation with their experimental data.

$$Z = \frac{u\left(\ln\frac{d}{2\delta_o}\right)\left(\sqrt{\frac{\rho_L d^3}{\sigma}} + \frac{3\mu d}{\sigma}\right)}{f(Oh, We)} \tag{2.16}$$

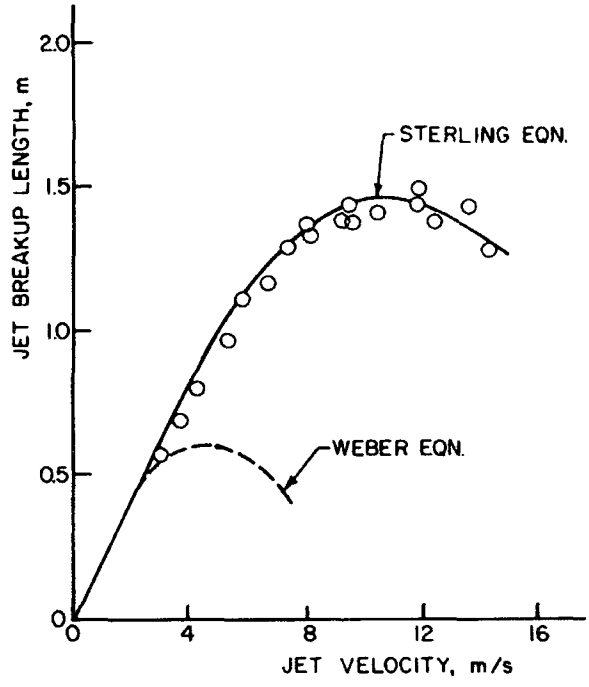

Figure 2.4: Comparison of experimental data with predictions of Webber and Sterling (Lefebrve, 2001).

Another correlation that is useful in the laminar flow region is (2.17). This equation was proposed by Grant and Middleman (1966), and is easier to apply than equation (2.16).

$$Z = 19.5d\sqrt{We}\left(1+3Oh\right)^{0.85} \tag{2.17}$$

Point B in Figure 2.3 is the upper critical point. Haenlein (1932) and Weber (1931) noted that this is the critical velocity at which the jet transitions from a break down mechanism governed by the lack of aerodynamic forces to one where the surface disturbances are assisted by the surrounding air. Smith and Moss (1917) attribute this

point to the onset of turbulence with in the jet. Grant and Middleman (1966) offer an empirical correlation to estimate the critical Reynolds number for this point.

$$\mathrm{Re}_{crit} = 3.25Oh^{-0.28} \qquad (2.18)$$

Between points B and C there is little data in the literature. However, once the jet becomes turbulent at the exit the break up length once again increases with velocity. There are several theories on the mechanics of the break up in the turbulent flow regime. Castleman (1931) theorized that it is the aerodynamic interaction between the surface waves caused by the turbulence and the surrounding air that eventually leads to the growth of the disruption and the eventual disintegration of the jet. Schweitzer (1937) argues that it is the radial component of the turbulent fluctuations that act on the surface of the jet immediately downstream of the nozzle exit that cause the jet to break up. Rupe (1962), attribute the breakdown to velocity relaxation within the jet. Reitz and Braco (1979) concluded based no their work that no single feature is solely responsible, and that depending on the case, combinations of the different mechanisms will be at work.

Numerous researches have proposed correlations for the break up length. Grant and Middleman (1966) offer the following:

$$Z = 8.51dWe^{0.32} \qquad (2.19)$$

Baron (1949) suggests a slightly different equation.

$$Z = 538d\sqrt{We}\,\mathrm{Re}^{-0.625} \qquad (2.20)$$

There is also debate regarding the trend of stability curve as the velocity increases towards infinity. Tanasawa and Toyoda (1954) state that the break up length increases indefinitely with increasing velocity, while Yoshizawa et al. (1964) argues the reverse is true. The data presented by Hiroyasu et al. (1982) and Arai et al. (1985) show that as the

velocity increases the break up length increases up to a point. Once the velocity exceeds said point, the break up length begins to decrease.

2.3 Cavitation

Further complicating the internal flow of the injector is the occurrence of cavitation. Cavitation is a general term used to describe to generation of voids or bubbles in a liquid. In practice, a liquid will develop cavitation bubbles if the local pressure falls significantly below the saturated vapour pressure. In general, cavitation is undesirable and must be avoided, if possible. In many fluid machines, such as hydraulic turbines and pumps, cavitation causes noise and excessive vibration leading to a decrease in the device's efficiency, loss of capacity and potential damage. These problems are the result of the cavitation bubbles collapsing resulting in the formation of shock waves and high temperatures. Over time, this can erode metals, drastically reducing the lifetime of many components.

In contrast to hydraulic machines, in diesel fuel injectors, cavitation is not only desirable but is believed to be necessary in producing a finely atomized spray in a short distance. The exact method by which cavitation helps the process of atomization is not completely understood. The occurrence of cavitation within the nozzle is a very complex, unsteady, three-dimensional, multi-phase phenomenon (Schmidt and Corradini, 1997).

A commonly found parameter describing the inception of cavitation in hydraulic machinery is the cavitation parameter. For injectors, this may be, defined as

$$\sigma = \frac{P_2 - P_v}{\frac{1}{2}\rho u^2} \tag{2.21}$$

where P_2 is the ambient pressure downstream of the nozzle, P_v is the vapour pressure of the liquid, ρ is the density of the liquid and u is the velocity of the liquid in the injection direction.

Many of the studies investigating the inception of cavitation have been performed for the sake of better understanding the performance of diesel injectors. The earliest of the referenced works for this is that of Bergwerk (1959). Bergwerk was interested in understanding the mechanism by which the fuel flow from a diesel injector was breaking up. He observed that the liquid jet emanating from a diesel injector was disrupted immediately downstream of the nozzle exit. At the time, the jet disintegration was attributed to air-friction forces or turbulent velocity fluctuations. Bergwerk felt that these explanations were unsatisfactory and that the flow inside the injector needed to be examined. In order to do this, he used the design shown in Figure 2.5, made of clear acrylic material, so that the flow inside the injector could be observed. The design, which he called a "square-entry nozzle", simulates the flow in a diesel injector with a sharp corner between the sac and the orifice.

Bergwerk observed that, at an injection pressure of 100 kPa, there were bubbles in the liquid inside the injector. When the injection pressure was increased to 165 kPa, a transition occurred with the following characteristics:

1. The disturbances vanished and the jet emerged from the orifice smooth and glass-like; further increases in pressure had no effect on the spray.

2. A cavity was formed that extended from the sharp corner to the end of the injector.

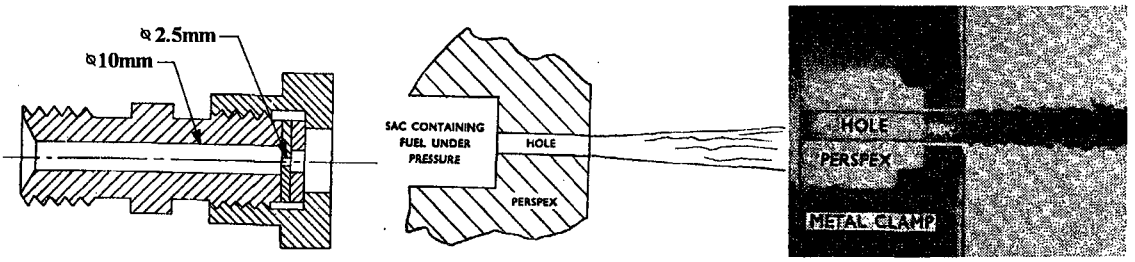

Figure 2.5: "Square-entry" nozzle used by Bergwerk (1959).

He attributed these phenomena to the occurrence of cavitation. The observed transition point occurred when the flow conditions were such that the cavitation number reached a critical value K_{crit}. Bergwerk's observation is known today as "hydraulic flip", a phenomenon to be discussed in this section. He proceeded to experiment with different nozzle geometries and differential injection pressures to determine the dependence of the critical cavitation number on the Reynolds number and the orifice length to diameter ratio.

Bergwerk expressed the cavitation number as:

$$K = \frac{P_1 - P_2}{P_2} \tag{2.22}$$

where P_1 is the injection pressure (or the pressure upstream of the injector) and P_2 is the ambient pressure outside the injector. Note that the cavitation number is commonly defined differently, as:

$$K = \frac{P_1 - P_2}{P_2 - P_v} \tag{2.23}$$

where P_v is the vapour pressure of the liquid. Bergwerk removed the vapour pressure from the equation as it is three orders of magnitude smaller than P_2.

Bergwerk made the following conclusions:

1. K_{crit} decreases with Reynolds number.
2. K_{crit} increases with an increase of l/d_o, and with a decrease of d_o.
3. K_{crit} is greatly affected by nozzle design, as minute manufacturing details can cause asymmetry in flow separation behind the sharp edge.
4. Cavitation would decrease the discharge coefficient.

Bergwerk's work has been recognized as an excellent start; however, it leaves many questions unanswered. In particular, this work has not examined quantitatively the influence of internal flow characteristics on the jet break-up length, the fuel distribution and the droplet size. The majority of the references in the 1950s, 1960s and 1970s are focused on the discharge co-efficient of the orifice and not on the resulting spray (Spikes and Pennington, 1959; Hall, 1963; Nurick, 1976). Another primary focus of the research during this time was the global spray characteristics such as cone angle and physical appearance. It was not until the early 1980s that the effects of the internal nozzle flow on spray properties became a popular research topic.

The next most referenced work is that of Nurik (1976). He used a slightly different form for the cavitation number:

$$K' = \frac{P_1 - P_2}{P_1 - P_v} \tag{2.24}$$

By combining this with the discharge coefficient and continuity equation, one may derive a useful relation for determining the approximate discharge coefficient of a cavitating orifice as

$$C_d^2 = \frac{C_c^2}{K'} \tag{2.25}$$

where C_d is the discharge coefficient and C_c is the contraction coefficient, a geometrically-dependant parameter equal to $\pi/(\pi+2)$, or approximately 0.61 for sharp-edged orifices. These works have been revisited, extended and experimentally supported by several authors including Ruiz (1991), Ohrn et al. (1991a) and Schmidt and Corrradini (1997). Ruiz derived equation (2.26) by calculating the head loss through the injector. He assumed that the exit velocity is equal to the bulk flow speed and that it has a uniform distribution across the injector. He notes that the following equation is for shape-edge orifices and that it can also be used to estimate the discharge coefficient of high Reynolds number non-cavitating orifice flows.

$$C_d = \frac{1}{\sqrt{1.4 + 0.04\frac{L}{D}}} \tag{2.26}$$

Ohrn et al. (1991a) experimented with several nozzle sizes and manufacturing methods to determine which have the greatest effect on the discharge coefficient. Using experimental data and equation (2.27) they found that for a sharp edged orifice the shape and condition of the nozzle inlet have a much greater effect on the discharge coefficient than the length to diameter ratio or the Reynolds number.

$$C_d = \frac{\dot{m}}{\rho A\sqrt{\frac{2\Delta P}{\rho}}} \tag{2.27}$$

Another approach for calculating the effective area and effective exit velocity of a cavitating orifice has been proposed by Schmidt and Corradini (1997). Their derivation uses a momentum balance, neglecting the momentum transfer to the walls. This zero shear model results in the following expressions:

$$V_{eff} = \frac{2C_c P_1 - P_2 + (1 - 2C_c)P_v}{C_c\sqrt{2\rho(P_1 - P_v)}} \tag{2.28}$$

$$A_{eff} = \frac{2C_c^2(P_1 - P_v)}{2C_c P_1 - P_2 + (1 - 2C_c)P_v} A \tag{2.29}$$

The authors emphasize that any simplified analysis such as the one presented in their work can not capture the transient, three-dimensional behaviour of cavitation. They do note however, that this model correlates well with the experimental data collected by Chaves et al. (1995) and Karasawa et al. (1992), as well as results from a fully compressible two-dimensional CFD simulation by Schmidt and Corradini (1997).

The 1990s mark the beginning of extensive research on the effect that internal nozzle flows have on the spray. This may be attributed largely to the development of optical diagnostics techniques and the creation of ILASS. Among the several research groups, Japanese researchers are at the forefront of many investigations. The most frequently cited works have been provided by Hiroyasu, Shimizu, Arai, and Tamaki. Their research originates from the early work of Hiroyasu, who studied the structure of sprays from diesel injectors in the mid 1970s. This group has investigated cavitation and the nozzle's internal flow effect on the spray, including break-up length, spray cone angle, spray tip penetration and droplet size (Tamaki et al., 1998; Arai et al., 1991; Hiroyasu, 2000). They have examined the effects of numerous parameters on the aforementioned spray characteristics, including nozzle geometry, injection pressure and ambient gas density. Their measurements include visualization of the flow inside the nozzle and the generated spray, break up length, and vibrations in the nozzle. Based on their results, they argued against the classical atomization theories that attribute the jet break up to interfacial forces between the liquid and ambient gas. They concluded that

the internal nozzle flows have the dominant effect on jet break-up and specifically that the presence of high turbulence levels in the liquid, caused by the occurrence of cavitation, is what enhances atomization.

They also present in their findings the different possible structures of the cavitation inside the injector. It should be noted that the image of super-cavitation shown in Figure 2.6 is commonly referred to as hydraulic flip by most other researchers.

The team has experimented with several geometries to study cavitation phenomena, with the goal of maximizing injector performance and decreasing break up length. A summary of those employed over the last decade is shown in Table 2.3. The designs used by that team have progressively improved atomization, with the latest version having excellent performance and improving atomization with a two orders of magnitude reduction in injection pressure. This is an important achievement, as a reduction in injection pressure without sacrificing nozzle performance gives substantial energy savings. The exact mechanism by which the 2003 design improves atomization is not completely explained. The team theorizes that the pressure rise in the gap causes the cavitation bubbles to collapse, which results in large disturbances in the flow which in turn improve atomization as shown in Figure 2.7.

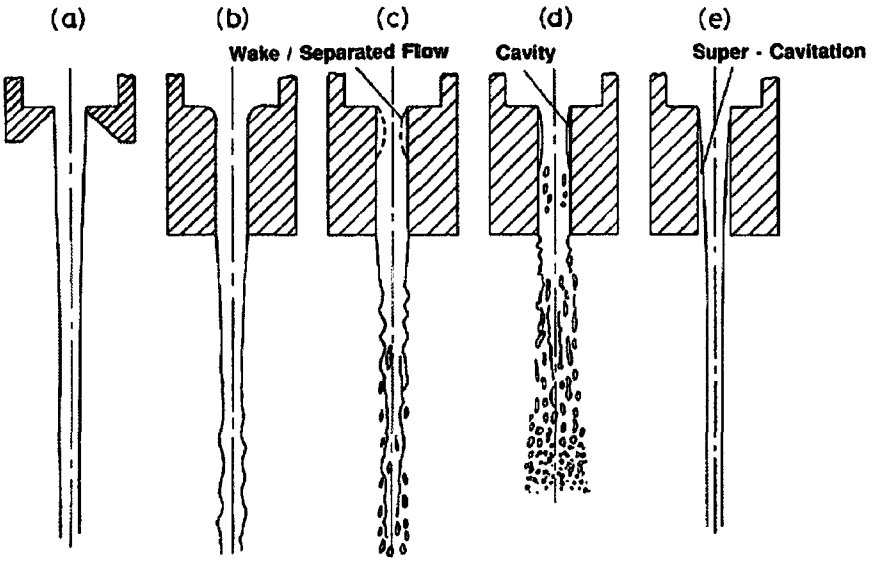

Figure 2.6: Cavitation structure as observed by Hiroyasu et al. (2000).

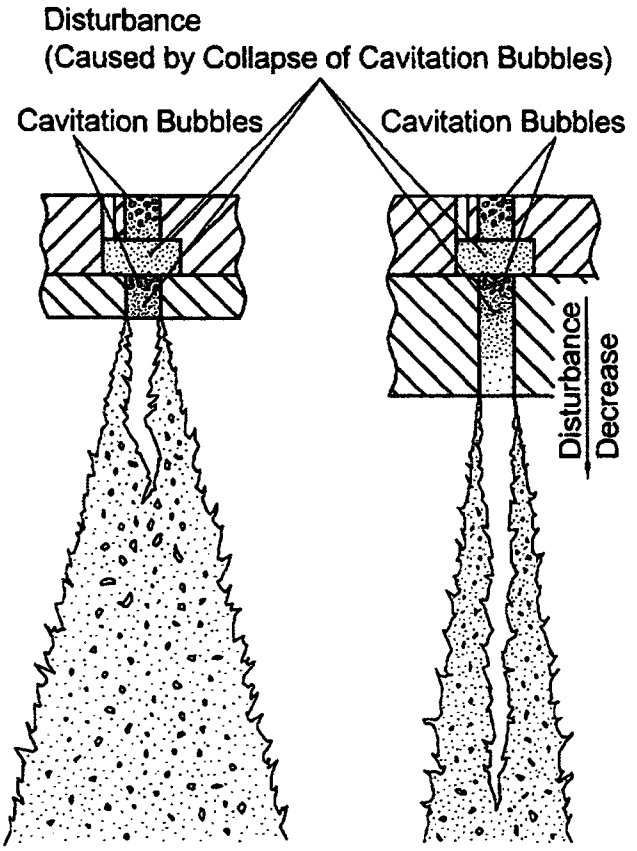

Figure 2.7: Sketch and description of the mechanism by which cavitation improves injector performance (Tamaki et al., 2000).

Year	Injector Design	Notes
1997 and 1998	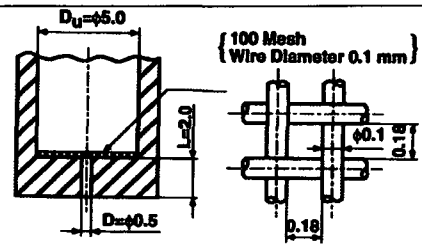	Examined the effect L/D and found that a smaller L/D improved atomization.
2000	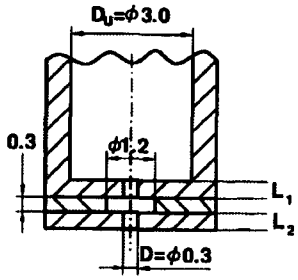	Experimented with different values of L1 and L2. Found that the best atomization and smallest break-up length were achieved with the smallest L1 and L2.
2001	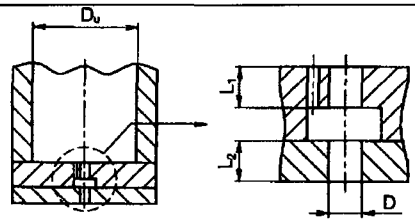	Varied lengths L1 and L2 and found that the greatest amount of atomization is achieved with a small (L1+L2)/D
2003	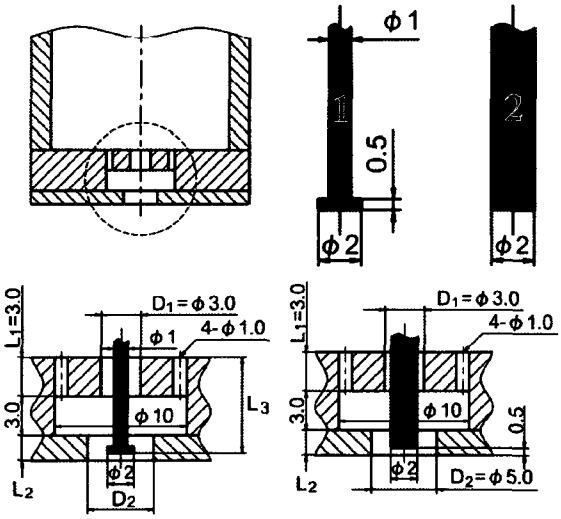	Experimented with two pins (labeled 1 and 2). Determined that better break-up is achieved with pin 1. Experimented with varying the lengths of L2 and L3. Found that the best atomization and smallest break-up length were achieved with the smallest L2 and the longest L3

Table 2.3: Historical summary of injectors used by Hiroyasu, Shimizu, Arai, and Tamaki.

A bibliographical review paper by Dumont et al. (2000) on cavitating flow in diesel injectors summarizes many of the key scientific studies up to 1999. The authors agree that the collapse of gaseous structures is a catastrophic process, however they note that

Winklhofer (1997) has demonstrated that this only results on surface perturbations and does not cause atomization. Dumont et al. (2000) argued that the only effect cavitation has on the spray is to increase the jet velocity by reducing the effective area of the passage. This increase in velocity improves the atomization according to the classical models discussed previously.

The conclusions drawn by the literature review made by Dumont et al. are not widely accepted. Stahl et al. (2005) have made the following statement:

"It is now generally accepted that the strong influence of cavitation on atomization comes primarily through the induced turbulent velocity field."

There is limited research directly examining the effect of turbulence on atomization. One study of note that has produced some interesting results is that of Wu et al. (1995), who performed a comprehensive examination of the initial flow conditions on primary break-up. In a portion of their study, they used an injector that removed the boundary layer from the liquid flow. In doing so, all atomization was suppressed. They concluded that the jet exit conditions, particularly the vorticity due to turbulence, play a dominant role in primary break-up along the surface of the jet. Stahl et al. (2005) noted that the transverse momentum transfer immediately downstream of the nozzle is likely responsible for the jet break-up.

The work of He and Ruiz (1995), coincidentally appearing in the same volume of Atomization and Sprays as Wu's work, supports this "transverse moment theory". He and Ruiz's experiment examined the effects of cavitation on flow and turbulence on a large scale, 1:200 model of an injector passage. The experimental set-up is shown in Figure 2.8. The test section is designed such that a recirculation zone is formed at the

entrance of the test duct. If the flow velocity is high enough, a cavitation bubble can also be produced. Measurements of the horizontal (axial) and vertical (radial or transverse) mean and turbulent velocity components were made on both cavitating and non-cavitating flows. He and Ruiz make two conclusions from these measurements that are pertinent to the argument presented by Stahl.

1. The turbulence intensity behind the vapour filled cavity was consistently 10 to 20% higher than that in a non-cavitating flow.
2. The location of the largest vertical turbulent intensity was closer to the orifice wall in the cavitating flow than in the non cavitating flow.

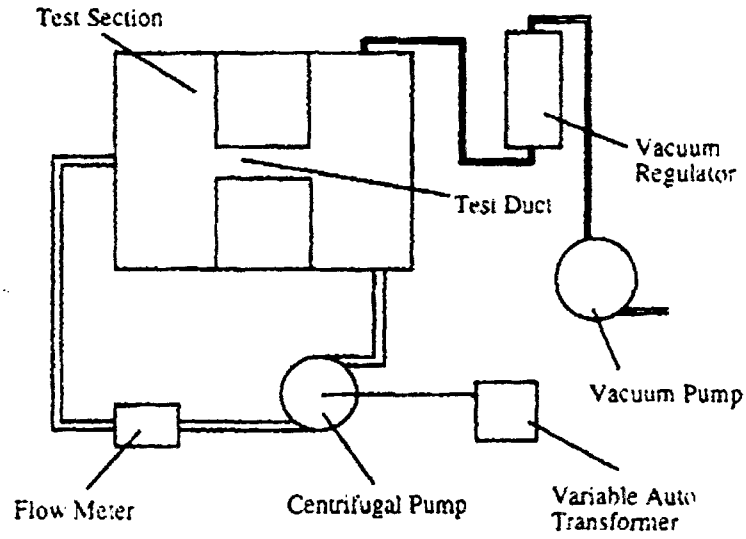

Figure 2.8: Experimental set up used by He and Ruiz (1995) to measure the velocity characteristics downstream of a cavitation bubble.

Stahl et al. (2005, 2006) further examined the effects of internal flows and turbulence on the generated spray. The nozzle geometries they used were similar to those in previous studies (Figure 2.9). Nozzle A is shaped like a funnel to reduce the turbulence and the size of the boundary layer. Nozzle B, despite having a sharp

contraction, was designed to avoid having a cavitating flow. Nozzle C has a similar geometry to Nozzle B however an insert was placed inside the injector to increase the turbulence in the flow. Velocity measurements were taken inside the 1 mm orifice using laser Doppler velocimetry. Measurements were also taken of the droplet size and velocity in the spray. Preliminary results of the resulting flows confirmed what had been observed by other researchers. A spray could not be produced by nozzle A, despite very high injection pressures. Nozzle B and C both produced sprays, with that from C having a wider cone angle and apparently more finely atomized droplets, presumably due to the increase in turbulence. No conclusions about the injector performance were made, because the focus of the work was on making and correcting the LDV measurements in the 1 mm passage.

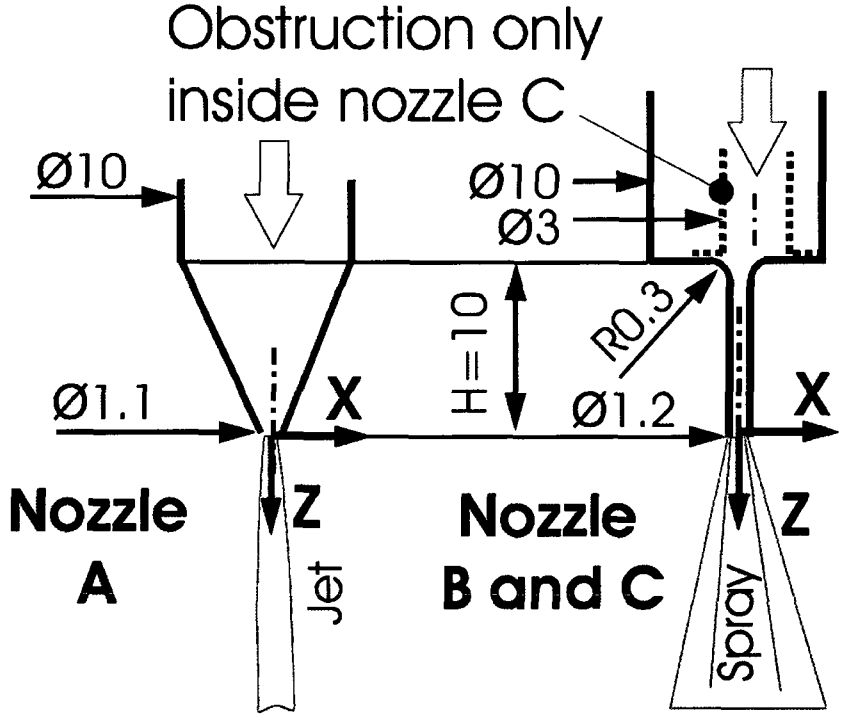

Figure 2.9: Nozzle geometries A, B and C used by Stahl et al. (2005).

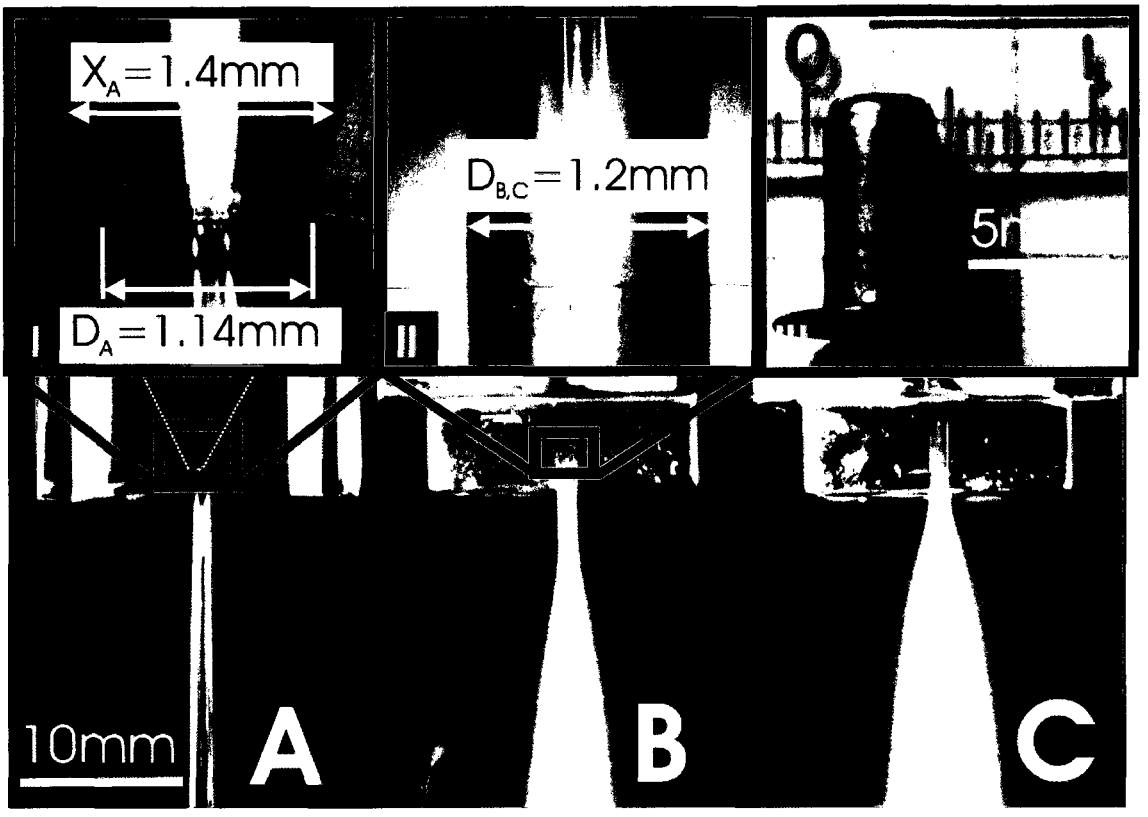

Figure 2.10: Sprays generated by three nozzles with upstream RMS velocity fluctuations equal to 0.03 m/s (A), 4.2 m/s (B) and 10 m/s (C) (Stahl et al., 2005).

Stahl et al. (2006) continued this work focusing on injectors B and C. At the start of the 2005 program, this injector design was believed to produce a flow free of cavitation. However, in the 2006 tests, cavitation was observed in the injector. The authors proceeded to study this cavitation more closely and the data set taken by Stahl et al. (2006) employed a nozzle with a sharper inlet to produce more intense cavitation. The new nozzle used in the 2006 study, henceforth referred to as "D", is shown in Figure 2.11.

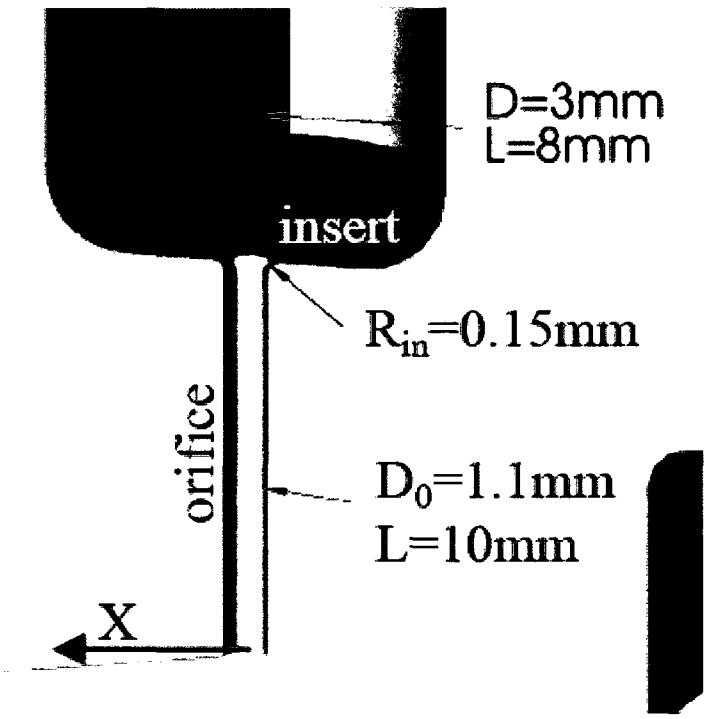

Figure 2.11: Nozzle geometry "D" used by Stahl et al. (2006).

As in the 2005 study, Stahl et al. collected spray cone angle data, velocity measurements of the flow inside the injector, and droplet sizing and velocity of the spray. The flow visualization results are shown in Figure 2.12. Surprisingly, the spray with the smaller cone angle was found to have smaller droplets. This is somewhat counterintuitive, because a spray with a wider cone angle would be expected to be better atomized. The authors attribute this to better secondary droplet break-up due to the faster droplet velocity in the narrow spray.

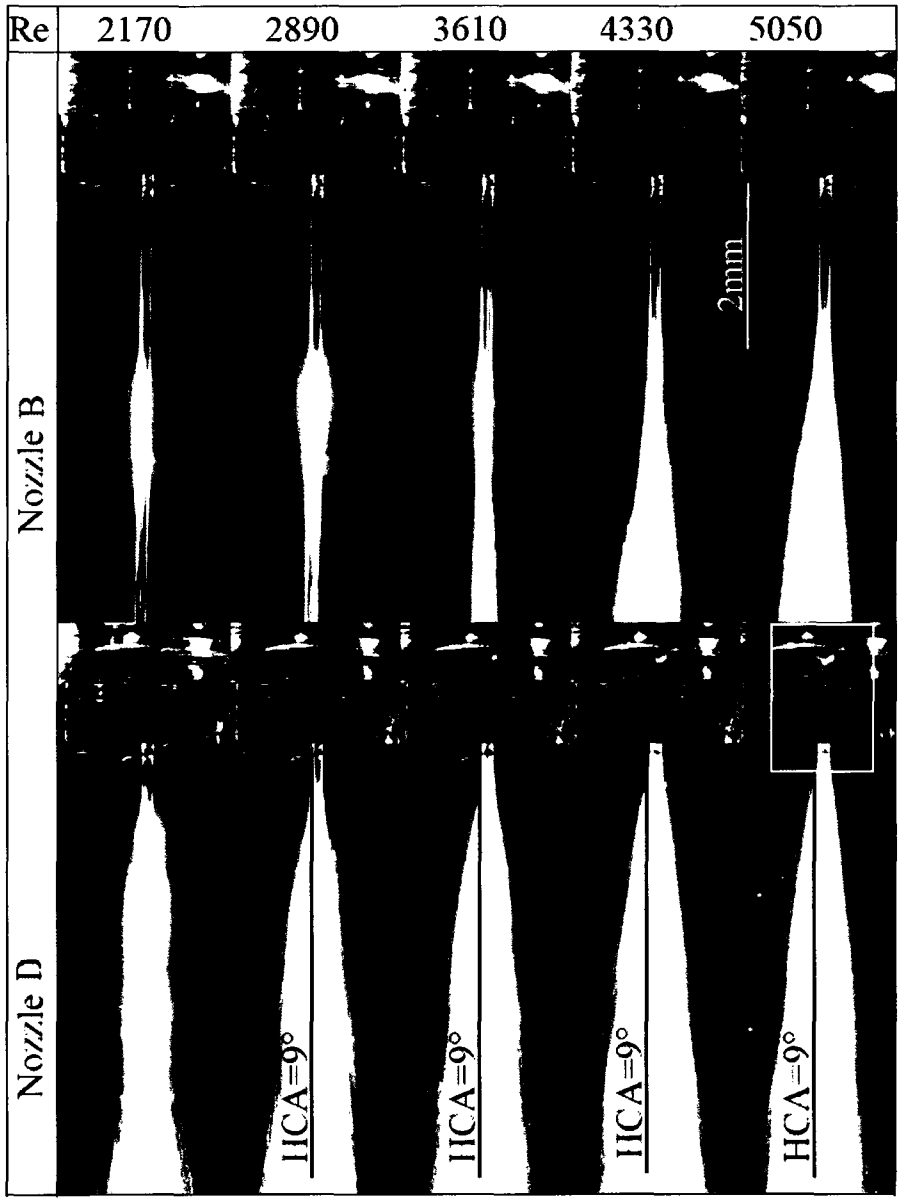

Figure 2.12: Flow visualization at different Reynolds numbers (Stahl et al. (2006); HCA is Half Cone Angle.

The cavitation bubbles were also measured and found to have a mean diameter of 20.5 μm. These bubbles were also observed to increase in diameter as they travel down the injector, which is attributed to the reduction of static pressure along the passage. The sizing of the bubbles was used to calculate a local gas volume fraction. The authors

conclude that a turbulent flow with a gas volume fraction in the orifice is necessary for prompt atomization. The vapour in the flow improves the spray break up in three ways:

1. Vapour disturbs the surface of the jet simplifying the release of droplets.
2. Increased compressibility accelerates the wave growth on the surface of the jet.
3. Decreased viscosity in the multiphase flow region facilitates break up.

They also note that, if the nozzle flow is laminar, unsteady cavitation effects are insufficient to enable jet disintegration in the second wind-induced regime.

2.4 Research Plan

The goal of any "spray engineering" task is typically to control the size, velocity and distribution of the droplets in the spray. Despite the volume of literature, the relationship between the internal nozzle flows and spray that is formed is still not entirely understood. A better understanding of this interaction could lead to finer control over the spray that is achieved. The aim of this research is to expand the data set on this subject by changing the flow inside the injector via an obstruction. This flow will be analyzed using high speed photography, and the spray will be characterized using laser diagnostics to measure the droplet size and velocity in an attempt to find correlations between the internal flows and the spray that is produced.

Chapter 3 - Experimental Facilities, Instrumentation and Measurement

3.1 Experimental Facilities

Two test facilities were used in this study: the National Research Council of Canada, Gas Turbine Laboratory's Spray Dynamics Lab (SDL) and the Atmospheric High Flow Spray Facility (AHFSF). Both of these labs are equipped with air and fuel circuits consisting of pumps, flow meters, valves and thermocouples designed to deliver liquid fuel and air to spray nozzles. Both labs also contain data acquisition systems which control and monitor the experimental operation. A schematic of the flow lines for representative of both facilities is shown in Figure 3.1, and the capacities are shown in Tables 3.1 and 3.2. The SDL is designed to accommodate small spray nozzles and can more accurately monitor and control small air and liquid flows. The AHFSF is designed to house large industrial nozzles and is much better suited for large flow rates. Both labs have two sets flow lines, each suited to different flow ranges. This gives an experimenter four possible sets of instrumentation to choose from, allowing them to pick the most accurate instrumentation for their particular test condition. Note that for the present work, only the liquid delivery system was used.

Both facilities operate on the same design strategy for air and fuel delivery. The liquid fuel is drawn from a reservoir and pumped to the spray nozzle through a line using a variable speed drive pump. Flow control is achieved by tuning the pump and by pneumatic control valves, which allow the operator to adjust the fuel delivery by pressure or by flow rate independently. The fluid flow rates and temperatures are measured by Coriolis meters and a standard K-type thermocouple, respectively. The fuel and air

delivery pressures are measured at the nozzle using pressure transducers. The fuel spray is injected into a catch basin where the liquid is subsequently filtered and pumped back to the reservoir. In order to ensure that fuel properties remain unchanged, samples were collected periodically and inspected visually for signs of degradation.

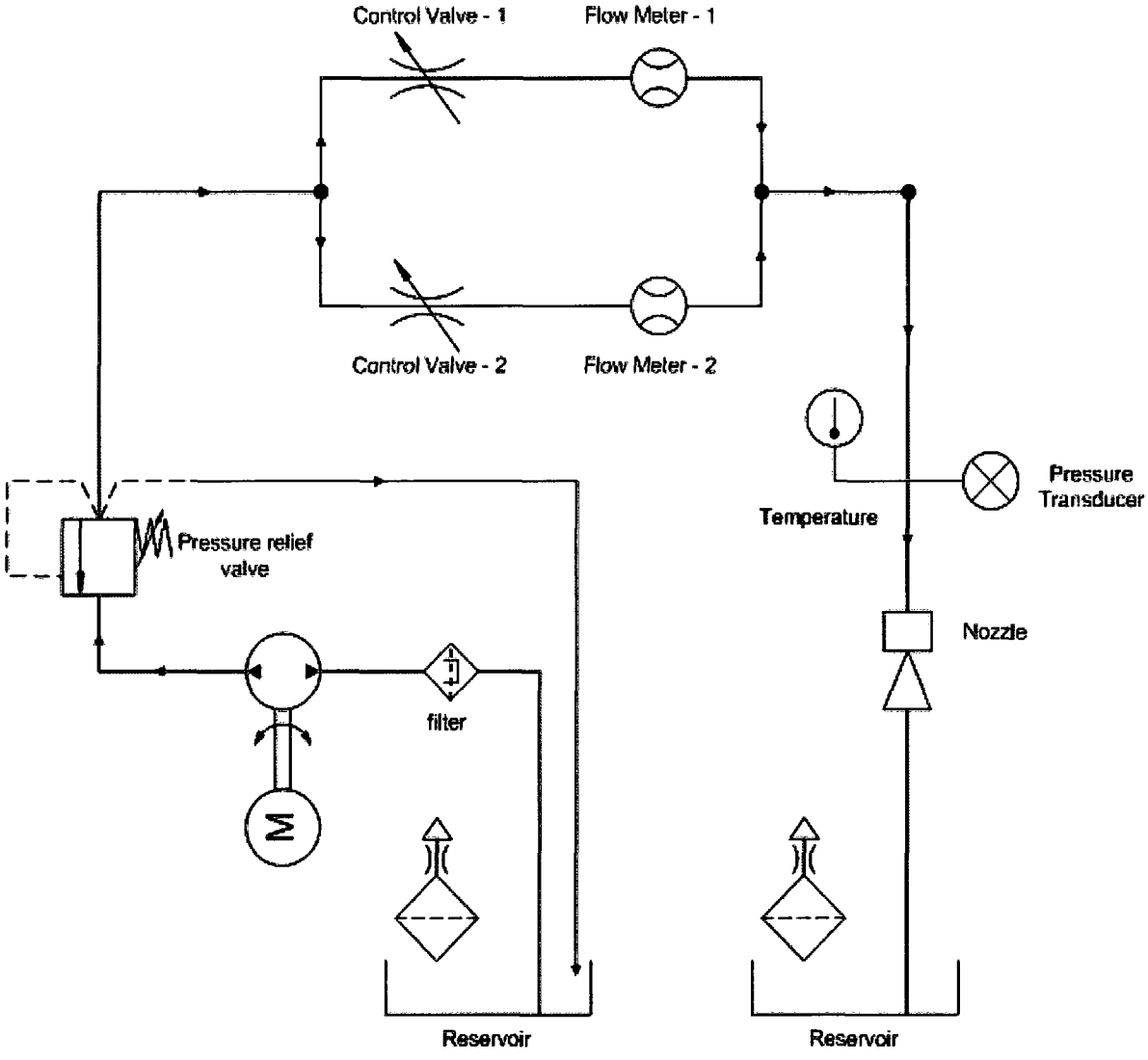

Figure 3.1: Schematic of fuel lines of SDL and AHFSF.

SDL				
Description		**Instrument**	**Calibration Range**	**Uncertainty**
Fuel Temperature		Thermocouple	0 – 120 °C	+/- 2 °C
Fuel Pressure	Low	Transducer	0 – 1379 kPa	+/- 3.4 kPa
	High	Transducer	0 – 3447 kPa	+/- 8.6 kPa
Fuel Flow Rate	Low	Coriolis meter	0 – 5.54 g/s	+/- 0.014 g/s
	High	Coriolis meter	0 – 25.2 g/s	+/- 0.063 g/s

Table 3.1: Instrumentation for the SDL Facility.

AHFSF				
Description		**Instrument**	**Calibration Range**	**Uncertainty**
Fuel Temperature		Thermocouple	0 – 100 °C	+/- 2 °C
Fuel Pressure	Low	Transducer	0 – 3447 kPa	+/- 8.6 kPa
	High	Transducer	0 – 6895 kPa	+/- 17.2 kPa
Fuel Flow Rate	Low	Coriolis meter	0 – 25.2 g/s	+/- 0.063 g/s
	High	Coriolis meter	0 – 110.9 g/s	+/- 0.277 g/s

Table 3.2: Instrumentation for the AHFSF.

The two labs use different data acquisition systems. The SDL employs a National instruments board controlled by LabView software. The AHFSF uses a KEP server, along with LabView software for monitoring the system and National Instruments Lookout software for system control. The SDL has a fixed data collection rate of 4 Hz, while the AHFSF can capture data at a maximum rate of 10 Hz.

Both labs are equipped with three-dimensional linear motion systems. The traversing unit in the SDL is designed to move the injector, while the AHFSF's system

traverses the optics. The former is preferable since traversing the optics runs the risk of having them become misaligned. The linear motion axes are defined in Figure 3.2.

The shortest distance the linear motion system can be moved in a single step is 0.01 mm. This is limited by the control software. In order to assess the repeatability of the system to return to a particular point in space Mitutoyo linear scale counters were employed, model numbers ALC-3705W and AL-315L. These encoders indicated the position of the measurement point to 0.005 mm. The resulting uncertainty for the X, Y and Z axis are 0.075 mm, 0.106 mm and 0.410 mm respectively.

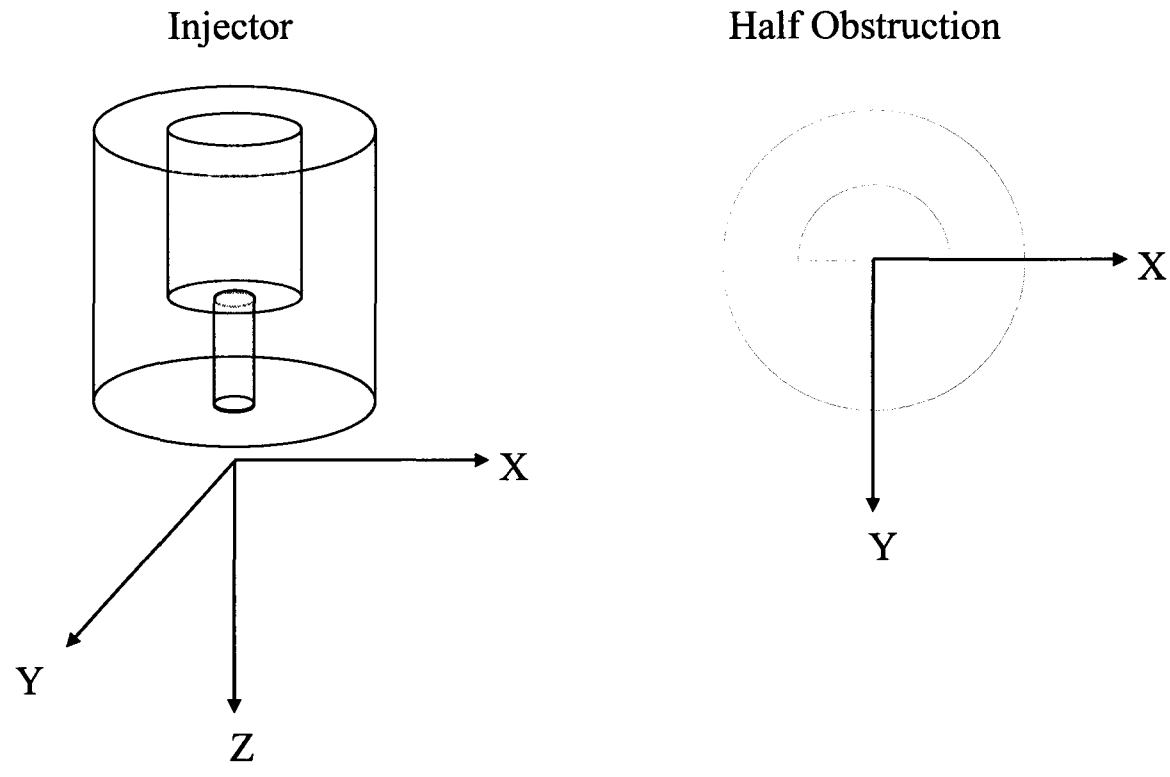

Figure 3.2: Linear motion axis, arrows indicate positive direction. Left: axis relative to injector. Right: axis relative to half obstruction.

The liquid used for all of the tests performed in this study is a nozzle calibration fluid which is commonly referred to as Stoddard solvent. This is a commercially available product which meets all requirements of MIL-PRF 7024E Type II. Its physical properties are listed in Table 3.3. This liquid has similar properties to kerosene, however it is less volatile, and is consequently safer to use in a laboratory environment.

Physical Properties	**MIL-PRF 7024C Type II**	**Kerosene**
Density	762 kg/m^3	822 kg/m^3
Viscosity	7.57 x 10^{-4} kg/ms	1.32 x 10^{-3} kg/ms
Surface Tension	0.0280 N/m	0.0277 N/m
Index of Refraction	1.47	1.47
Vapour Pressure	400 Pa	2200 Pa

Table 3.3: Physical properties of MIL-PRF 7024C Type II and kerosene

3.2 Injector

The injector used in this study is shown in Figure 3.3 and 3.4. It can be classified as a pressure atomizer. The geometry of the nozzle was selected in order to match injectors that have been employed in other successful research programs with similar motivations such as Stahl et al. (2006). It is a simple geometry that has the advantages of being easy and inexpensive to manufacture. The orifice size is large enough so that the flow inside can be examined, and still small enough to produce a spray from moderate injection pressures. The injector is made from acrylic material (Plexiglas) with plane surfaces machined on their sides to reduce visual distortions and so that optical diagnostics can be used to examine the flow inside the nozzles.

Upstream of the injector is a flow conditioning section, shown in Figure 3.3. The purpose of this section is to ensure that a uniform, low-turbulence stream enters the nozzle section, so that the turbulence that is introduced deliberately would have controlled properties and be free of interactions with any upstream disturbances. The device's layout is very similar to that of a wind-tunnel, and its design was done following guidelines by Mehta (1977). It consists of a diffuser, settling chamber and contraction, as well as fine-mesh screens to reduce the turbulence level. Flow enters this section through a ½ inch NPT fitting. The injection pressure is measured upstream of this conditioning section as shown in Figure 3.6.

In order to induce various types of cavitation, the injector was equipped with the obstructions shown in Figure 3.5. The injector is referred to as open or unobstructed if no blockage is present.

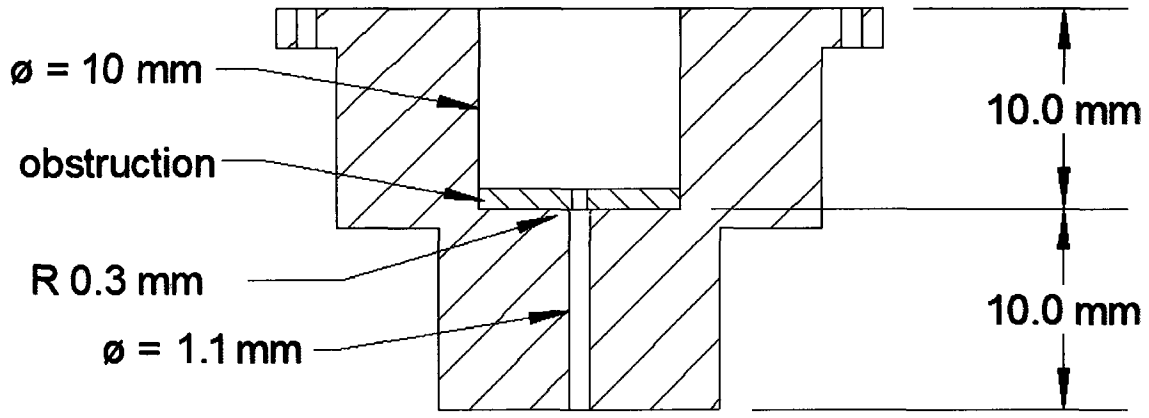

Figure 3.3: Cross-section of injector showing geometry of the liquid passage.

Figure 3.4: Photograph of entire injector showing the conditioning section and Plexiglas nozzle.

Name	Obstruction	Obstruction in Injector	Description
Screen	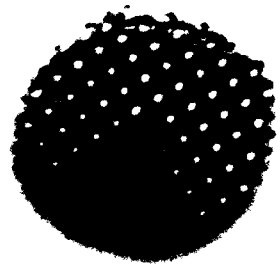	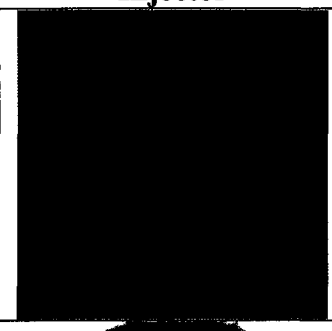	Wire mesh 15.7 wires per cm Wire diameter 0.024
Hole	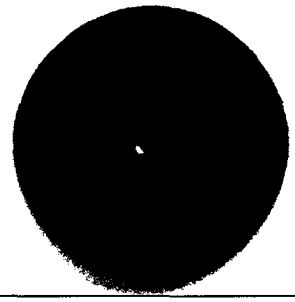	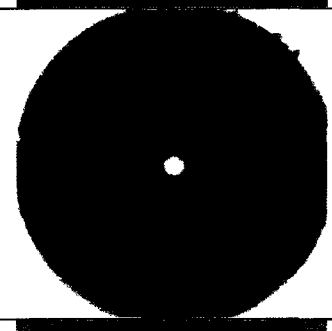	0.8 mm diameter hole
Slot	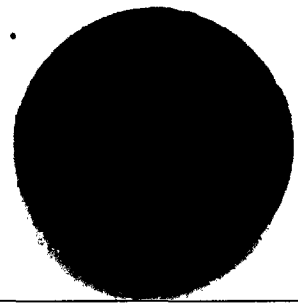	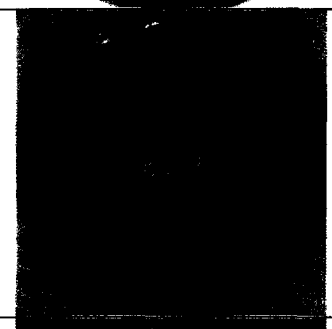	0.5 mm slot spanning across orifice
Half	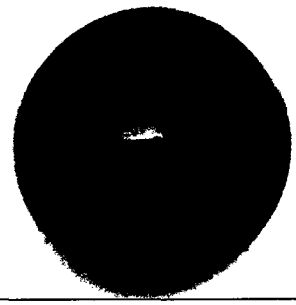	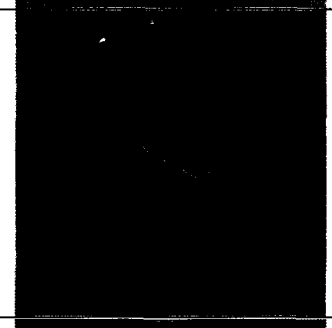	Semi-circular opening that blocks approximately half of the orifice.
Strip	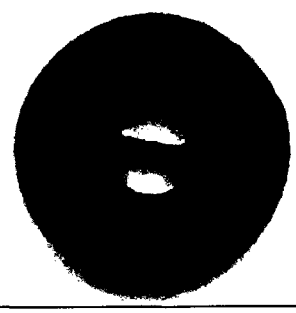	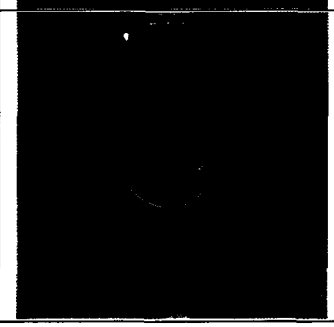	Two semi-circular openings with a 0.5 mm metal strip spanning the orifice

Figure 3.5: The obstructions used in the test shown in and out of the injector.

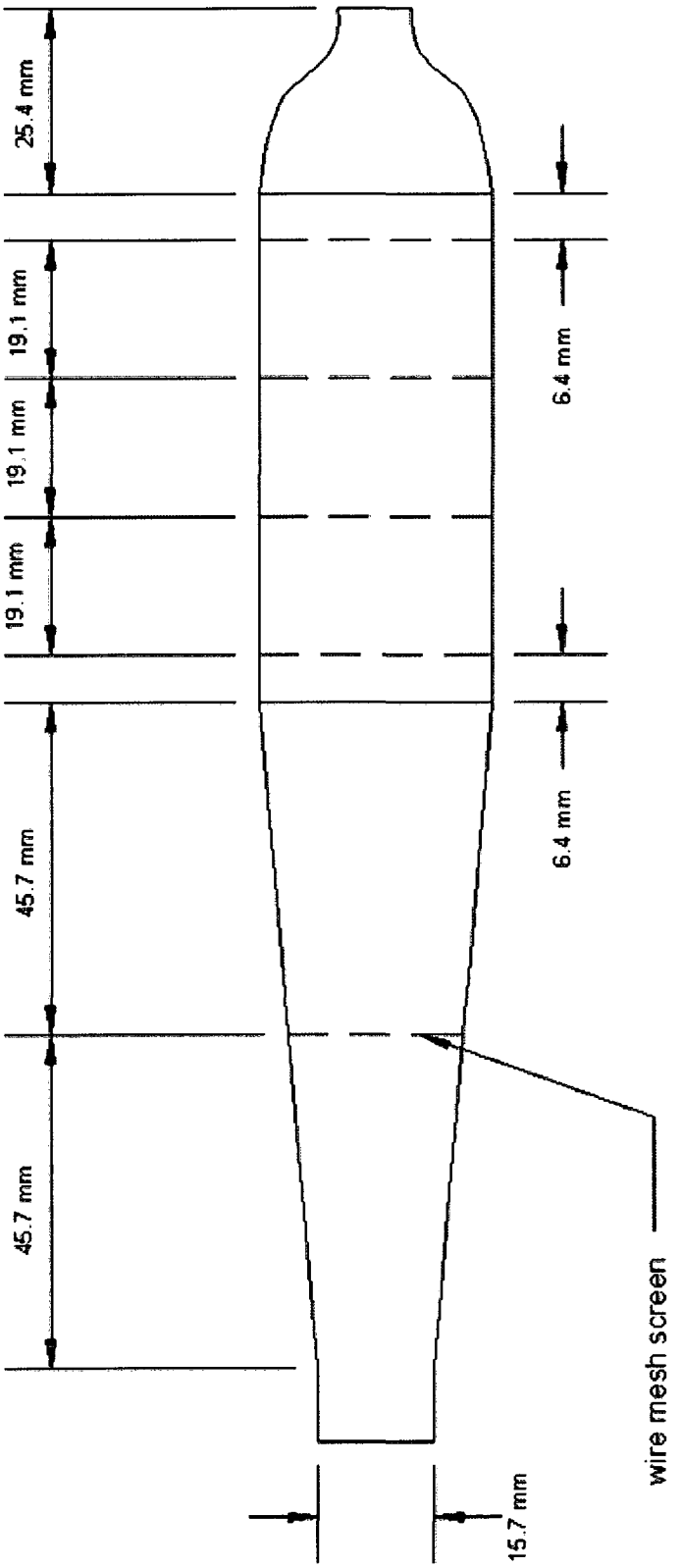

Figure 3.6: Geometry of flow conditioning section upstream of the nozzle. Flow direction is left to right

3.3 Instrumentation and Diagnostics

3.3.1 Pressure Transducers

A pressure transducer converts pressure into an analog electrical signal. There are many types of transducers, among the most common of which are strain-gauge transducers. These consist of a strain gauge which is bonded to a diaphragm. When pressure is applied to the transducer, the deflection of the diaphragm is sensed as a strain. The strain will produce an electrical resistance change proportional to the pressure and generate a current as output. The transducers used in this experiment output a current between 4 and 20 mA, which is large enough to be essentially unaffected by electrical noise and resistance in the signal wires.

Gauge pressure transducers were used to measure the liquid pressure upstream of the nozzle as shown in Figure 3.7. In the AHFSF a 0 – 3447 kPa transducer was used, and in the SDL a 0 – 1379 kPa, model number PTX 1210 Druck. The transducers used had a linear response and were calibrated using a Druck calibrator, model number DPJ802-P.

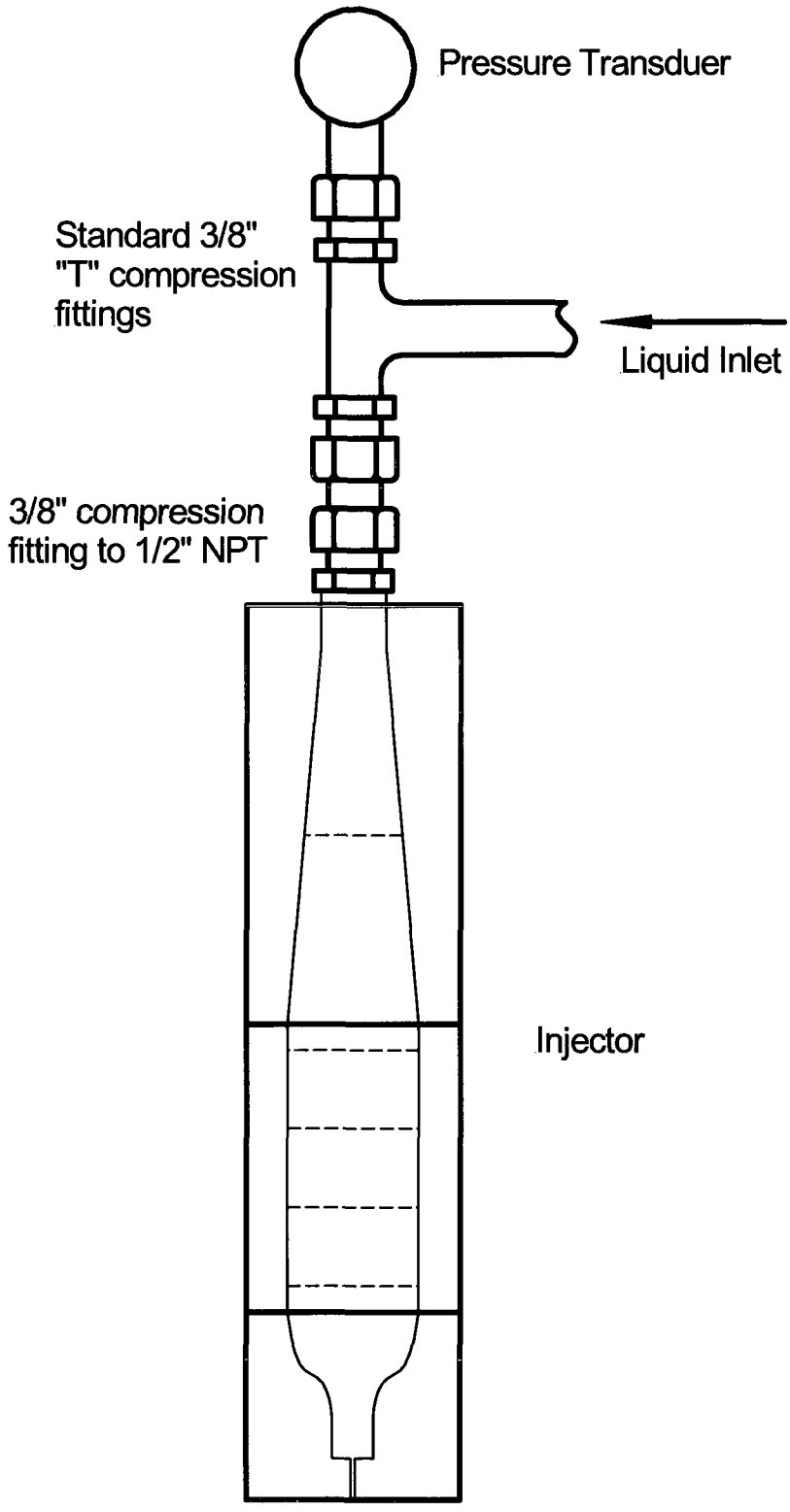

Figure 3.7: Sketch of injection pressure measurement location.

3.3.2 Coriolis Flow Meters

Coriolis flow meters measure the mass flow rate of a given flow. A typical configuration consists of one or two straight or U-shaped tubes that are vibrated by an electrical actuator. The fluid flowing through the tube will induce a rotation or twist to the tube because of the Coriolis acceleration acting in opposite directions on either side of the applied force as shown in Figure 3.8. The Coriolis meter measures this twisting motion, which is directly proportional to the mass flow rate.

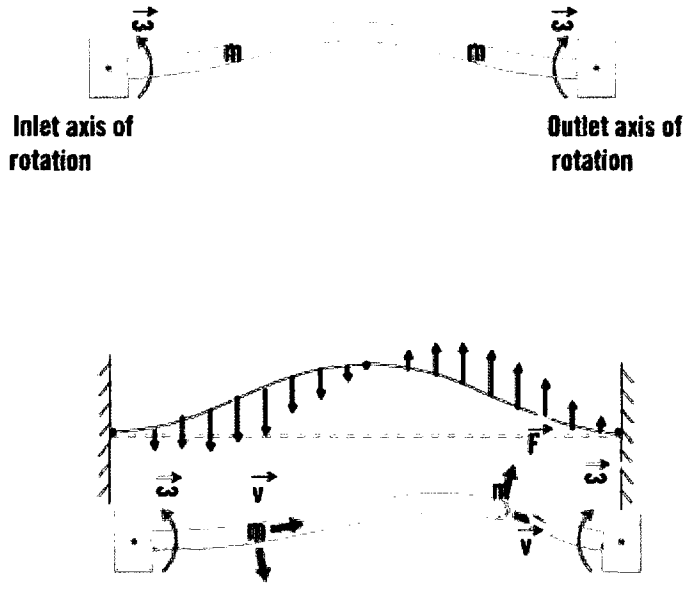

Figure 3.8: Coriolis flow meter operation. Top image shows tube with no flow, bottom image demonstrates the forces due to the moving fluid causing the tubes to twist where m and v are the mass and velocity of the liquid respectively, ω is the angular moment of the tube and F is the resulting Coriolis force exerted on the tube by the liquid.

An advantage of Coriolis flow meters is that they measure the mass flow rate directly, which eliminates the need to compensate for changing temperature, viscosity, and pressure conditions. They are also not affected by impurities in the liquid or non-

Newtonian behaviour (Tavoularis, 2007). The drawbacks are that their cost is generally higher than those of other metering systems and that their ranges are usually limited to smaller line sizes. Furthermore, the dynamic response of Coriolis meters has been proven to be slow when compared to other technologies due to the signal processing and physical characteristics of the meter. Endress and Hauser Coriolis flow meters, model number 63AS04, were used to measure the liquid and air flows through the nozzle. The properties of the flow meters used are shown in Tables 3.1 and 3.2.

3.3.3 High Speed Photography and Video

The photographic method used for both the high speed photographs and video was to use a high output flood lights to back-light the flows inside and outside of the nozzle. A sketch of the configuration is shown in Figure 3.9. This method produced good images for the spray as whole and of the cavitation occurring inside the injector. The short exposures of the spray display the degree to which the bulk liquid is disintegrating. The high speed video of the flows inside the injector allow for the unsteadiness of these flows to be observed. A Nikon D70s single lens reflex (SLR) camera equipped with a 24 - 120 mm 3.5-5.6/f autofocus lens was used to photograph the spray. A Canadian Photonics Lab Inc. (CPL) Mega Speed digital video camera, equipped with a Tamron 180 mm f/3.5 macro autofocus lens was used to film the internal nozzle flows. The CPL camera employs a global electronic shutter, essentially sampling the entire CCD array for a preset exposure time. This video camera was set to capture images at 6000 frames per second with exposure times of 75 μs.

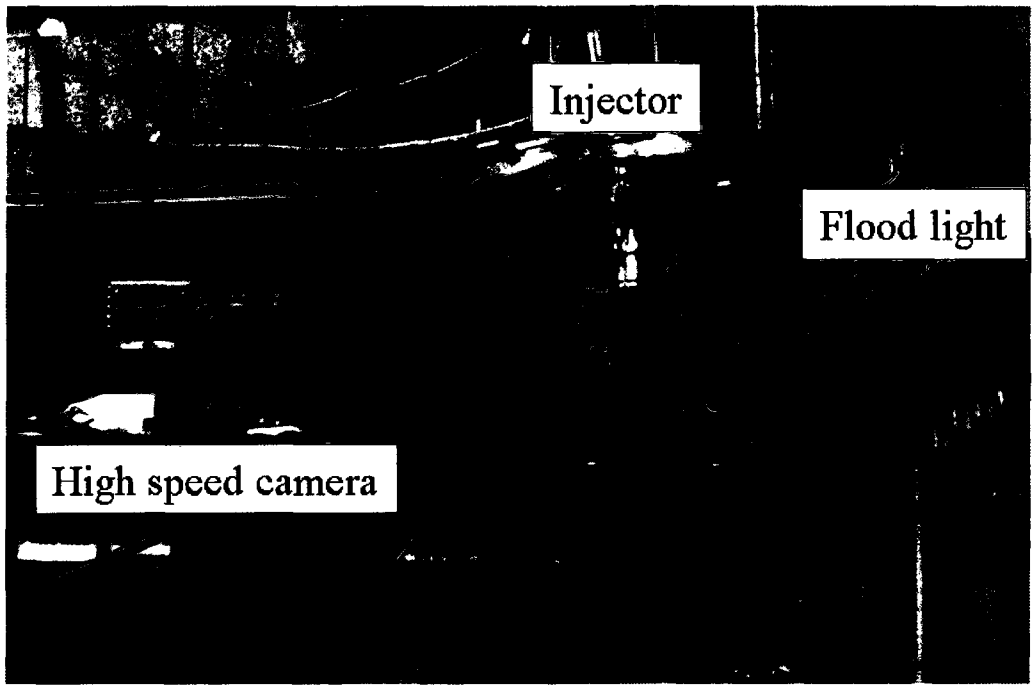

Figure 3.9: Flow visualization experimental set-up.

3.3.5 Laser Diffraction – Malvern Spraytec

Laser diffraction or Low-Angle Laser Light Scattering (LALLS) is an optical diagnostic technique used for measuring droplet size. This method consists of passing a laser through the field of particles of interest, and analyzing the diffraction pattern created by the scattered light from the droplets in the near forward direction. The angle at which the light is diffracted by a particle is a function of the particle's size, with the scattering angle increasing logarithmically as the particle size decreases. The intensity of the scattered light is proportional to the particle's cross-sectional area. The size distribution of the particles is determined by comparing the resulting pattern with an optical model using a mathematical inversion process.

Historically, two models have been used: the Fraunhofer Approximation and the Mie Scattering Theory. The Fraunhofer approximation is the less accurate of the two. It was employed in early particle sizing instruments due to its simplicity. It is based on

similar suppositions to Mie Theory, but with additional simplifying assumptions. Mie Theory provides a more accurate solution by including the particle's absorption effects and the secondary scattering signal caused by light refraction within the particle which is especially important for transparent particles with diameters lower than 50 μm.

In this study, a Malvern Spraytec, which employs a full Mie Scattering Theory, was used for sizing the droplets in the spray. A sketch of system is shown in Figure 3.10, and its specifications are shown in Table 3.5. The system was operated in continuous mode for the tests, which limits the speed of Malvern to 1 Hz. The Malvern is traversed across the spray with 30 sample points collected at each location to produce a spatial and temporal average of the droplets in the spray. Based on the accuracy and precision provided by the manufacturer, the uncertainty of the SMD measured was calculated to be less than 6.6 μm.

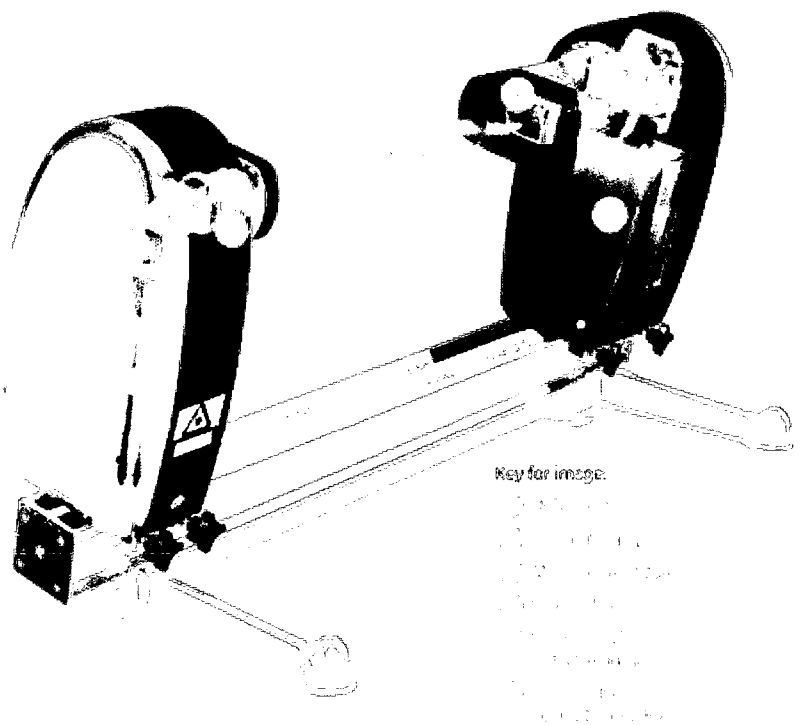

Figure 3.10: Malvern Spraytec particle sizer (Source: Malvern).

Malvern Data Sheet	
Size Range	0.1 μm – 2000 μm
Lens Range	750 mm lens: 2 – 2000 microns (Dv50 : 5 – 1600 microns).
Working Range	0.5 microns: 150mm 5 microns: > 1000 mm 10 microns: > 2000 mm
Concentration Range	Patented Multiple Scattering Correction Minimum acceptable transmission: 5% - dependent on particle size range
Detection system	36 element log-spaced silicon diode detector array
Light source	632.8 nm, 2 mW helium-neon laser
Maximum acquisition rate:	Continuous Mode: 1Hz Rapid Mode (Standard): 2.5kHz Rapid Mode (Enhanced): 10kHz
Maximum measurement time:	Continuous Mode: > 60 mins at 1Hz Rapid Mode: maximum of 120 sec at 2.5 kHz Rapid Mode: maximum of 30 sec at 10 kHz
Accuracy	Better than +/- 1% on the Dv50 for NIST-traceable latex standards
Precision / Repeatability	Better than +/- 1% COV on the Dv50 for NIST-traceable latex standards
Reproducibility between instruments	Better than +/- 1% COV on the Dv50 for NIST-traceable latex standards

Table 3.5 Specifications for Malvern Spraytec particle sizer (Source: Malvern).

3.3.6 Phase Doppler Particle Analyzer

Phase Doppler anemometry or point interferometry, is a laser based diagnostic method that can measure the size and velocity of a particle at a specific location in space. This technique splits a laser beam into two beams, and then crosses these beams to form a measurement volume. The crossed beams form an interference pattern of bright and dark fringes. The distance between the fringes is

$$d_f = \frac{\lambda}{2\sin\theta_b} \tag{3.2}$$

where λ is the wavelength of the laser light, and θ_b is the angle of intersection of the two beams as shown in Figure 3.11. When a particle passes through this area, it scatters the light which is collected by the receiving optics. The frequency of the signal can be used to calculate the velocity of the particle, in a manner similar to laser Doppler velocimetry. If two detectors are used to collect the signal at slightly different scattering angles, they will each measure a different phase. The difference in the phase, ΔΦ of the signal has a linear relation to the diameter of the particle as

$$\Delta\Phi = \frac{2\pi D}{\lambda} \frac{\sin\theta_b \sin\psi}{\sqrt{2(1-\cos\theta_s \cos\psi \cos\theta_b)}} \tag{3.3}$$

where θ_s is the scattering angle, ψ is the elevation angle as shown in Figure 4.7, and D is the diameter.

A TSI Inc. Phase Doppler Particle Analyzer (PDPA) was used to make measurements of the droplet size and one velocity component in the spray. The optics were set up in a 30° forward scatter configuration. A 500 mm focal length transmitter and 500 mm receiver were used in conjunction with a 150 μm receiver slit to minimize

the size of the measurement volume. The specifications for this configuration are shown in Table. 3.6. A picture of the PDPA set up is shown if Figure 3.12.

PDPA Specifications	
Beam Waist	185.1 μm
Beam Separation	20.0 mm
Beam Diameter	1.77 mm
Fringe Spacing	12.9 μm
Nominal Fringe Count	14
Velocity Range	-450 to 2251 m/s
Particle Size Range	1.4 to 558 μm

Table 3.6: TSI Inc. PDPA system specifications.

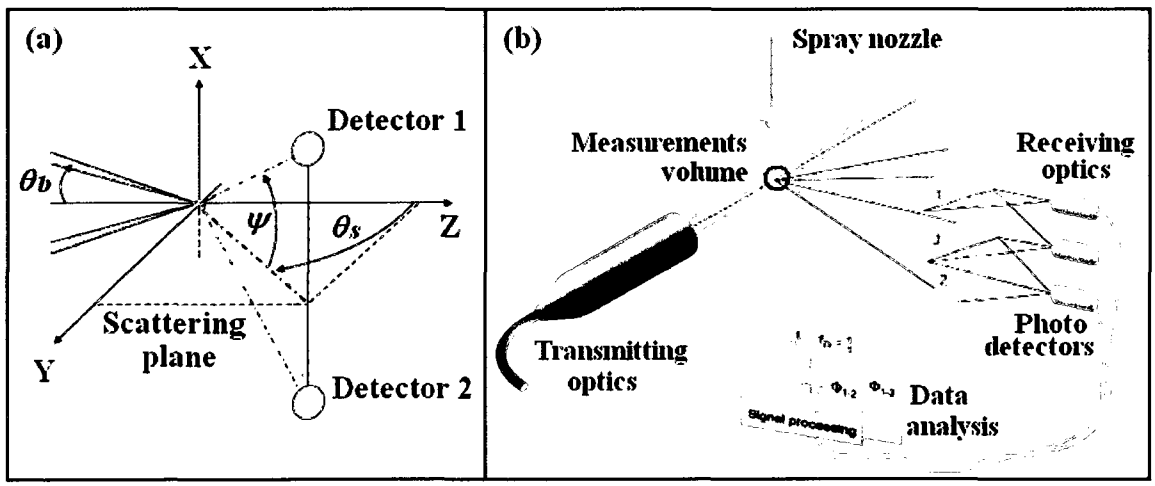

Figure 3.11: Standard configuration of the Phase Doppler Anemometry system. Angles are defined in (a) and the optical arrangement is illustrated in (b) (source: Dantec).

Figure 3.12: PDPA experimental set up.

Chapter 4 – Results

4.1 Injector Flows

This section outlines the flow capacities that are achievable by this injector. A summary of the flow conditions tested is shown in Table 4.1 and results are plotted in Figure 4.1. As expected, the various injector configurations have similar performance curves with the unobstructed injector passing the most fuel for a given injection pressure.

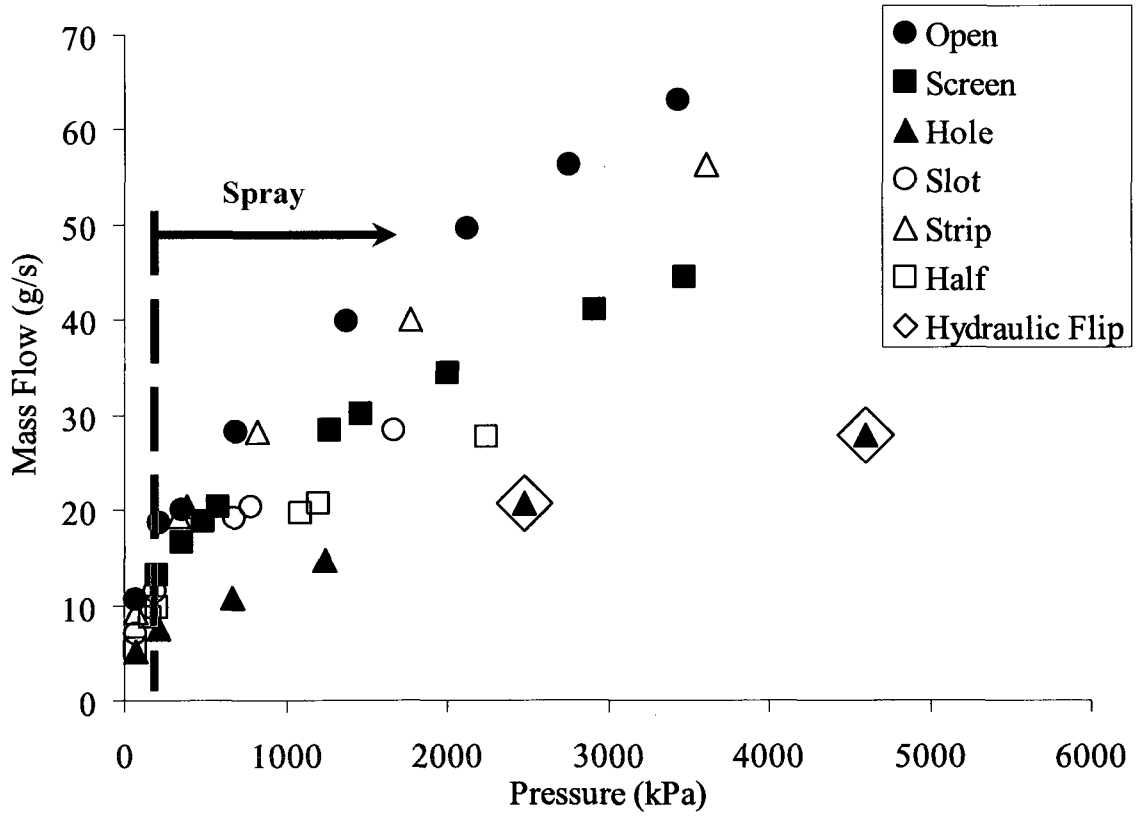

Figure 4.1: Mass flow vs. injection pressure for all obstructions.

Obstruction	Pressure (kPa)	Flow (g/s)	Bulk Exit Velocity (m/s)	Re	We
Unobstructed	70.7	10.6	12.33	14894	369
	211.9	18.7	21.72	31477	650
	350.7	20.1	23.30	33778	698
	686.8	28.2	32.76	47491	981
	1371.5	39.8	46.22	67001	1384
	2125.0	49.7	57.65	83571	1726
	2746.8	56.4	65.41	94810	1958
	3433.7	63.1	73.23	106155	2192
Screen	68.4	10.8	12.48	18088	374
	203.9	13.2	15.34	22231	459
	583.1	20.3	23.56	34146	705
	1266.7	28.5	33.05	47903	989
	1462.3	30.1	34.94	50648	1046
	2005.0	34.4	39.94	57890	1196
	2918.4	41.1	47.72	69168	1428
	3472.9	44.6	51.71	74949	1548
Hole	69.9	5.2	5.99	8679	179
	210.7	7.5	8.64	12531	259
	670.4	10.8	12.48	18087	374
	1241.7	14.6	16.99	24628	509
	2474.1	20.6	23.94	34700	717
	4595.8	28.0	32.44	47028	971
Wire	67.4	9.3	10.81	15671	324
	331.1	19.3	22.39	32461	670
	382.8	20.4	23.69	34335	709
	825.4	28.2	32.73	47448	980
	1764.7	40.1	46.51	67422	1392
	3605.9	56.4	65.40	94794	1958
Half	67.9	5.5	6.37	9236	191
	166.9	8.8	10.15	14718	304
	207.3	9.8	11.38	16491	341
	1081.4	19.7	22.85	33116	684
	1202.7	20.7	23.99	34771	718
	2242.8	27.8	32.22	46700	964
	5071.8	40.7	47.27	68524	1415
Slit	68.7	7.1	8.24	11943	247
	189.5	11.4	13.26	19220	397
	680.3	19.1	22.16	32118	663
	785.8	20.3	23.59	34197	706
	1670.0	28.4	32.90	47694	985
	4928.4	47.9	55.55	80521	1663

Table 4.1: Pressures, flow rates, calculated bulk velocities, Reynolds number and Weber number tabulated for the obstructions tested. The highlighted rows indicate the lowest flow rate at which the liquid column becomes a spray.

4.2 Flow Visualization

4.2.1 Photography

Photographs of the flow inside the injector and the resulting spray are presented in Figure 4.3 – Figure 4.7. The upper row of images show the flow inside the injector, and the resulting spray is shown in the bottom row. Figure 4.2 displays a scale for the flow visualization images. The field of view extends to approximately 150 mm downstream of the injector face.

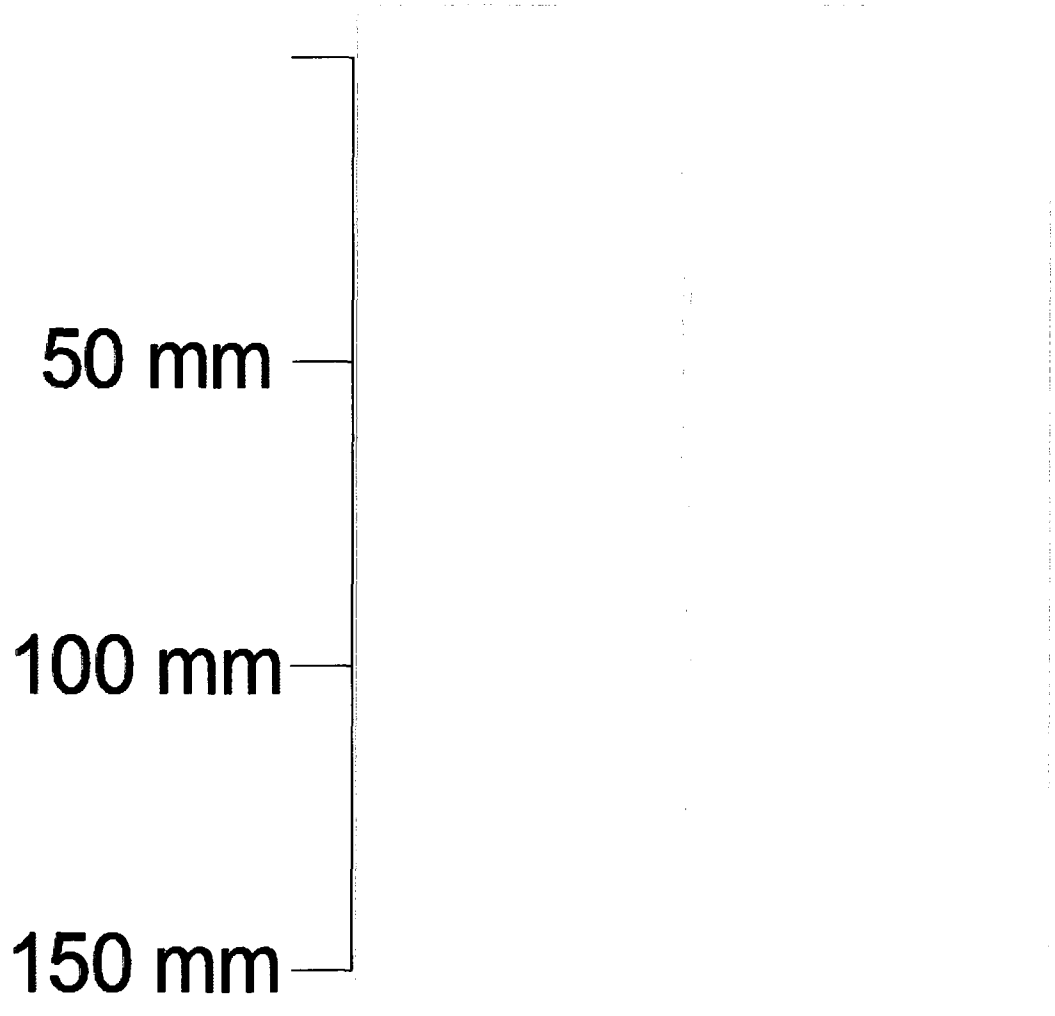

Figure 4.2: Scale of spray photographs.

Unobstructed Injector – Flow Visualization					
	70 kPa	**19g/s – 200 kPa**	**29 g/s**	**40 g/s**	**56 g/s**
Internal Nozzle Flow	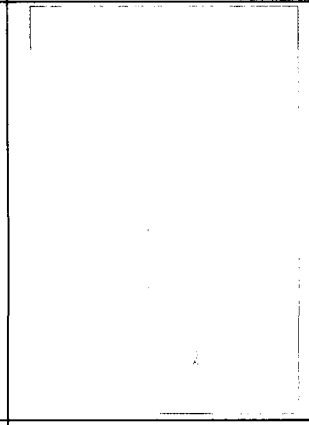	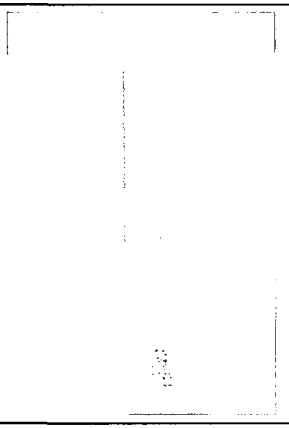	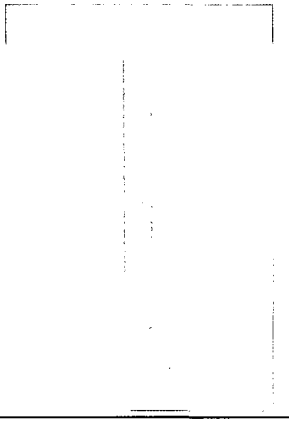	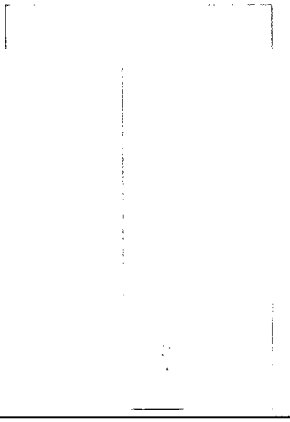	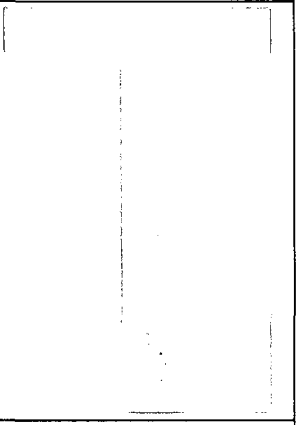
Spray	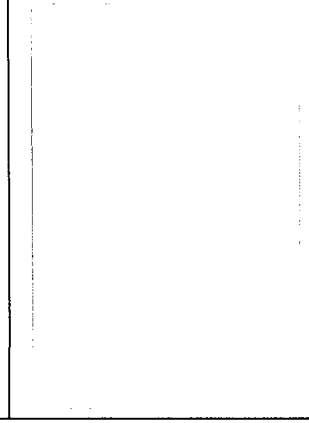	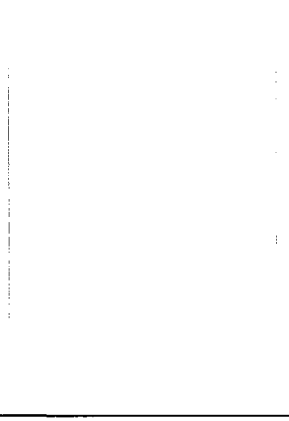		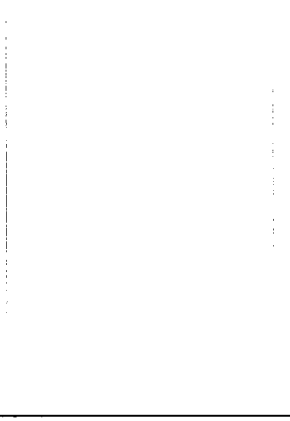	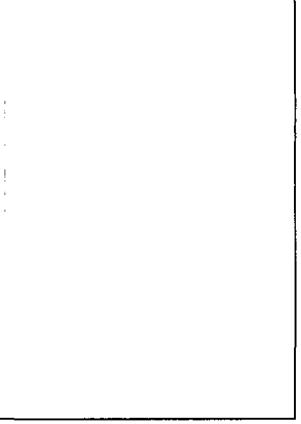

Figure 4.3: Internal nozzle flow and resulting spray for the unobstructed injector. The image of the internal nozzle flow is a 75 μs exposure. The image of the spray is a 1/8000 second exposure.

Screened Injector – Flow Visualization					
	70 kPa	**13g/s – 200 kPa**	**19 g/s**	**29 g/s**	**41 g/s**
Internal Nozzle Flow				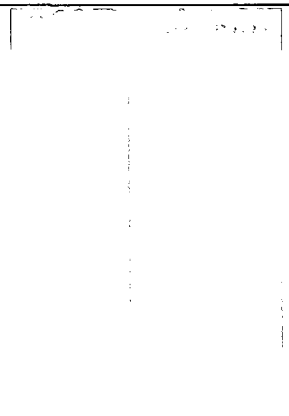	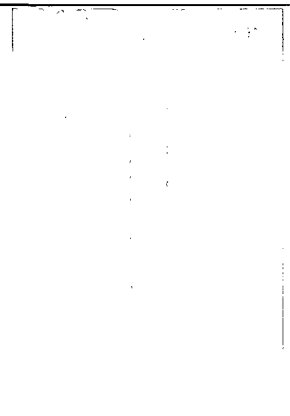
Spray					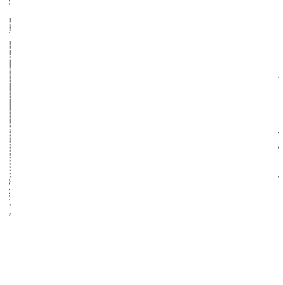

Figure 4.4: Internal nozzle flow and resulting spray for the unobstructed injector. The image of the internal nozzle flow is a 75 μs exposure. The image of the spray is a 1/8000 second exposure.

Hole – Flow Visualization					
	70 kPa	**8 g/s – 200 kPa**	**19 g/s**	**29 g/s**	**41 g/s**
Internal Nozzle Flow		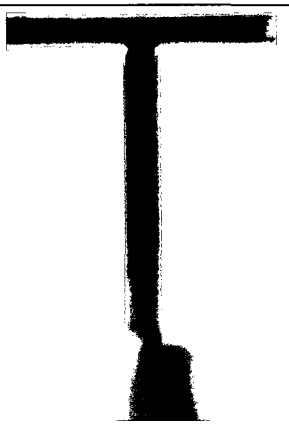	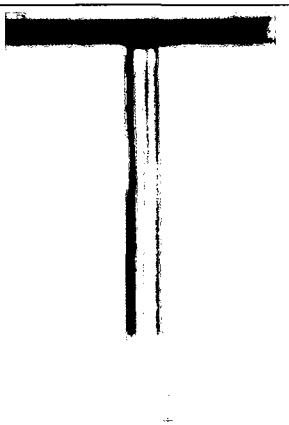	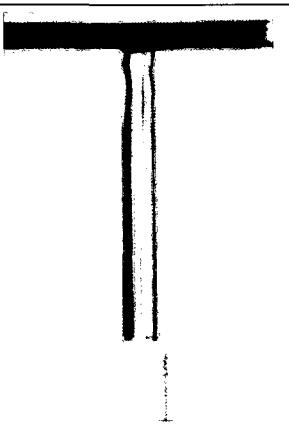	Flow Rate Not Achievable
Spray	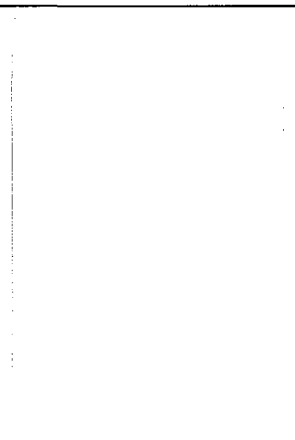	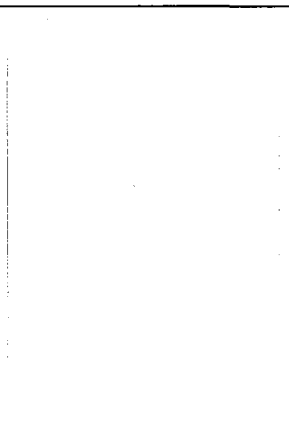	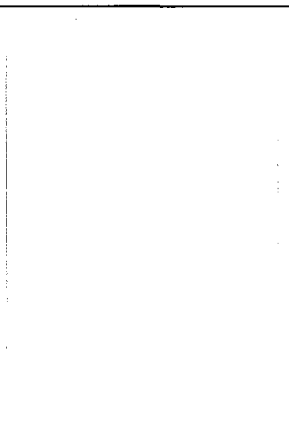	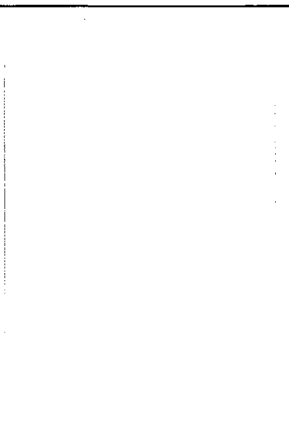	Flow Rate Not Achievable

Figure 4.5: Internal nozzle flow and resulting spray for the injector with the hole obstruction. The image of the internal nozzle flow is a 75 μs exposure. The image of the spray is a 1/8000 second exposure.

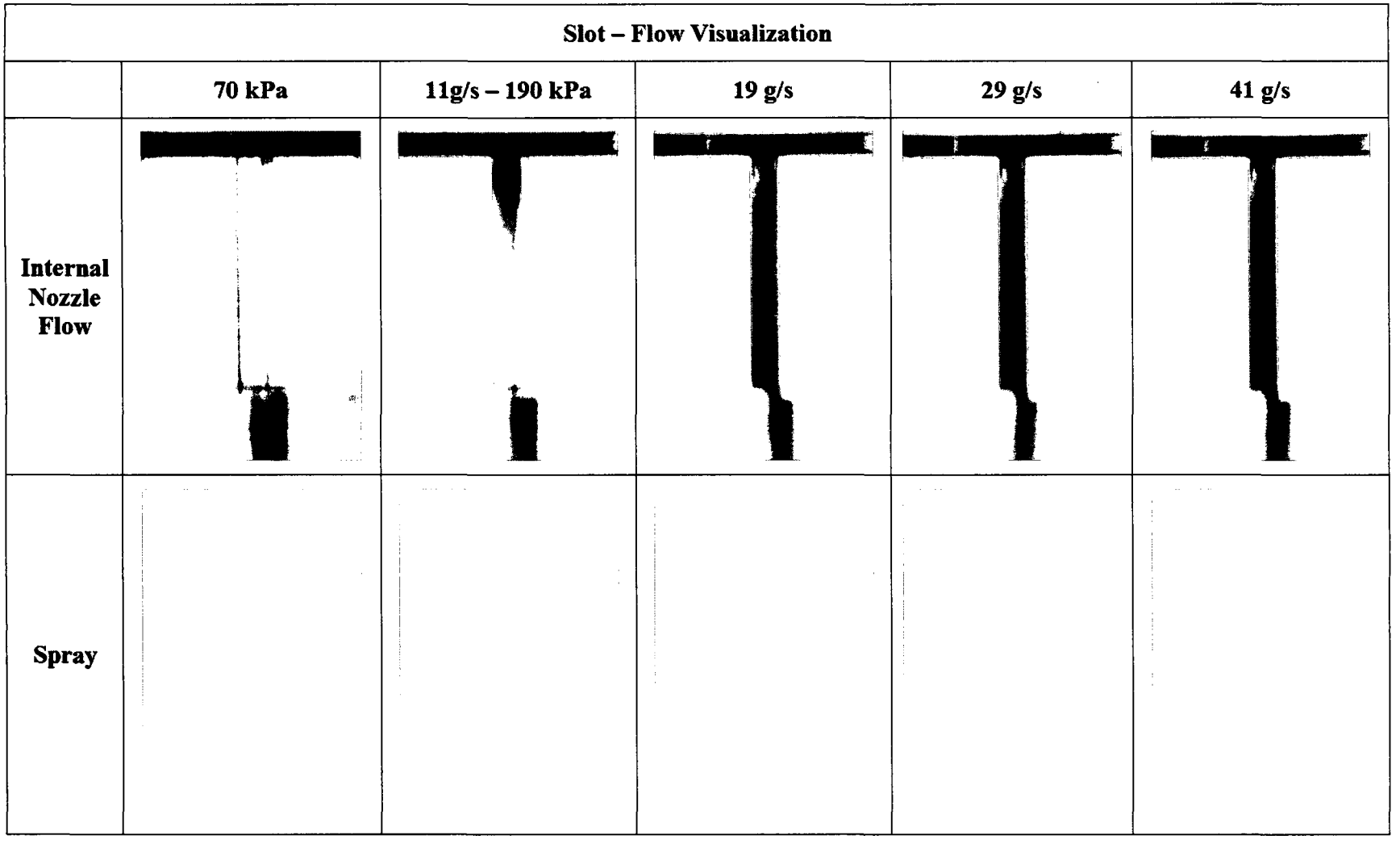

Figure 4.6: Internal nozzle flow and resulting spray for the injector with the slot obstruction. The image of the internal nozzle flow is a 75 μs exposure. The image of the spray is a 1/8000 second exposure.

Half – Flow Visualization					
	70 kPa	**9 g/s – 170 kPa**	**19 g/s**	**29 g/s**	**41 g/s**
Internal Nozzle Flow	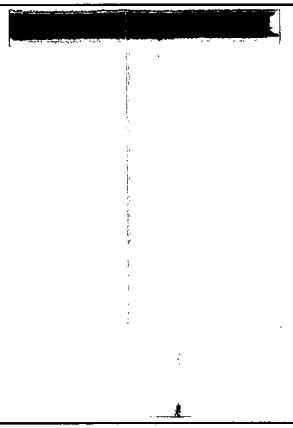	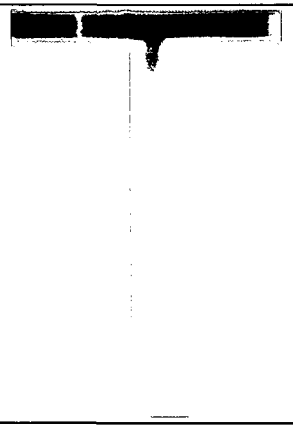	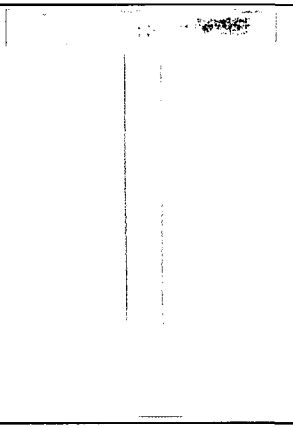	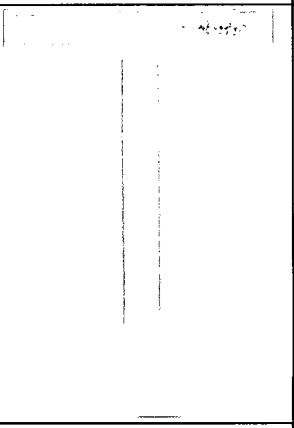	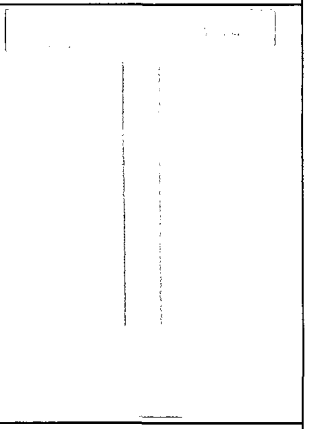
Spray	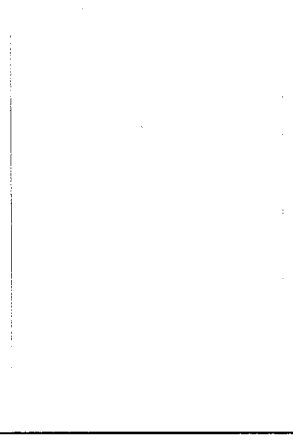	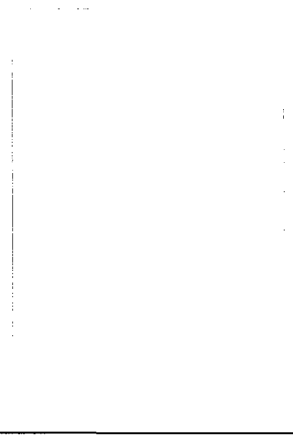	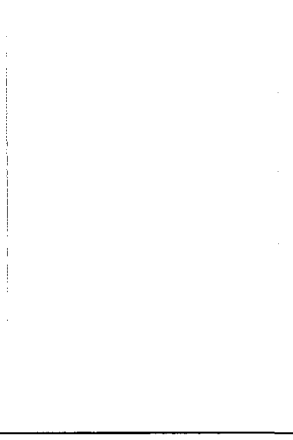	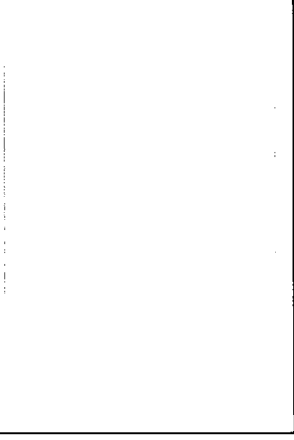	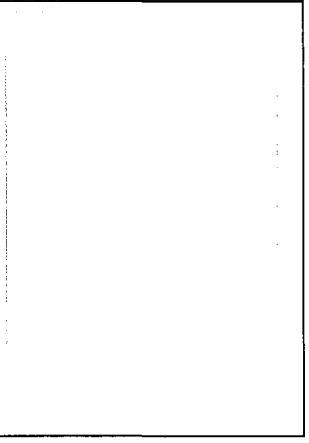

Figure 4.7: Internal nozzle flow and resulting spray for the injector with half of the nozzle obstructed. The image of the internal nozzle flow is a 75 μs exposure. The image of the spray is a 1/8000 second exposure.

The first column in Figures 4.3 to Figure 4.7 show a low flow condition with an injection pressure of approximately 70 kPa. Every nozzle configuration, except for the hole obstruction, appears to be completely transparent, showing a very smooth flow inside the injector. The resulting liquid jet for this flow condition is a column with little, if any, fluid break-up. Some unusual lines and bubbles can be seen on, and inside the acrylic wall. These lines are scratches on the surface of the injector that may have formed during day-to-day handling of the test equipment, whereas the internal inclusions might have been caused by stresses generated during the fabrication of the apparatus.

The second columns in Figures 4.3 – 4.7 display the flow conditions at which cavitation were first observed. Even with an injection pressure as low as 170 kPa, a change to the flow inside the nozzles is observed. Dark areas can be seen in the flow, which indicate that gas filled regions are present and that the flow is cavitating. The occurrence of the cavitation has an effect on the liquid jet for all flow configurations but with varying degrees of importance. For some of the cases, a drastic change in the spray is observed; for example, in the nozzle with the hole obstruction, the jet is converted from a liquid column to a spray. For others, such as the slot and half obstruction, the cavitation occupies less of the capillary portion of the injector, and the atomization is not as significant.

The final 3 columns of Figures 4.3 – 4.7 show the flow visualization results for fixed flow rates. For the slot, half, and screen obstructions, the cavitation bubbles have now completely filled the injector. The resulting spray is also improved: the cone angle has widened, in several areas the liquid column has been shattered and smaller droplets can be observed. The internal flows of the unobstructed and hole obstructed injectors,

however, now have completely different structures. For the former, the quantity of small cavitation bubbles is reduced, and, for the latter, one side of the passage appears to be gas filled while the other half is liquid filled. The unobstructed injector has two gas-filled regions near the entry to the capillary, with the one on the left side of the image being slightly larger. The sprays have also changed significantly for these two configurations. The unobstructed injector is producing a spray that is slightly asymmetric. An increased population of small droplets can now be seen at the edges of the spray, more so on the left hand side of image. The injector with the hole obstruction is no longer producing a spray. A long thin fluid column is now emerging from the injector with atomization occurring approximately 50 nozzle diameters downstream. Increasing injection pressure and flow rate does little to change this.

For the unobstructed injector, further increasing the pressure and flow rate results in an increase in the amount of cavitation observed in the nozzle, but there are no significant changes to the spray. The increase in flow rate is resulting in a denser spray, and the increase in the bulk exit velocity of the liquid is helping improve the atomization by increasing the shear forces between the fuel and the surrounding air.

4.2.2 High Speed Video

High speed video was collected for the flow inside the injector. The camera was set to collect images at a rate of 6000 frames per second. The images have an exposure time of 75 μs resulting in a time between exposures of approximate 92 μs.

The onset of cavitation for the unobstructed injector is shown in Figure 4.9. These images clearly illustrate the unsteadiness of this phenomenon. The location and quantity of cavitation bubbles can be seen to vary significantly. The screen and half obstructed injector show a more steady flow with the cavitation forming at the capillary inlet and convecting downstream. As the flow increases, the images show less unsteadiness in the flow for all conditions considered.

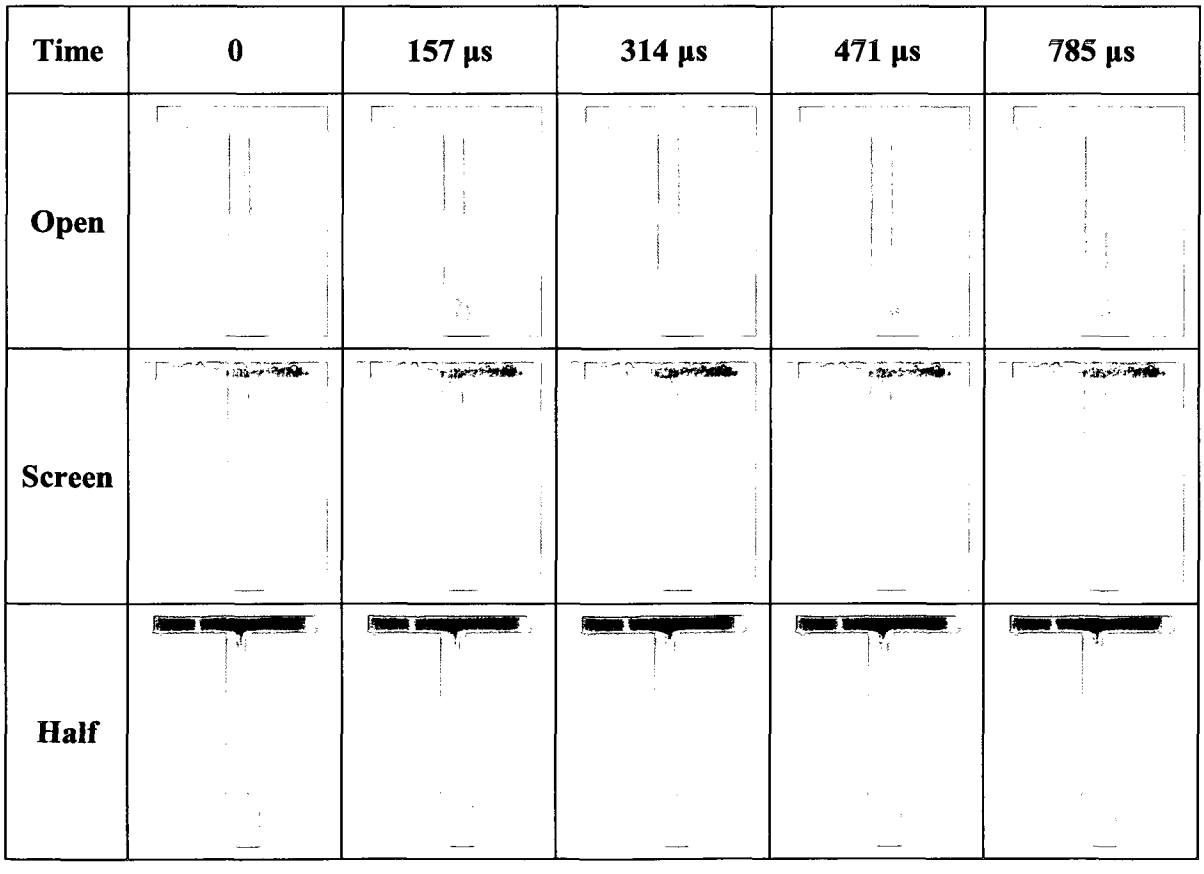

Figure 4.9: High speed images of the internal flow of an unobstructed, screen and half obstructed injectors at an injection pressure, at the onset of cavitation.

4.3 Spray Droplet Sizing and Velocity Results

4.3.1 Laser Diffraction Particle Sizing Results

Figures 4.10 and 4.11 display the droplet SMD measured by the laser diffraction for the unobstructed and screen obstructed injectors at various flow rates. The SMD is defined as

$$\text{SMD} = \frac{\sum d^3}{\sum d^2} \tag{4.1}$$

All measurements were taken at 100 mm downstream of the nozzle face. At each radial location, the droplet population was sampled for 60 s. These measurements were then averaged to generate the data plotted in Figures 4.20 and 4.21 (to be discussed later in this chapter).

Laser diffraction data are difficult to interpret because they correspond to spatial and temporal line of sight averages across the entire laser beam. As the laser beam has a thickness of 10 mm, and measurements were collected every 5 mm, this method does not offer precise information regarding a droplet population. Nevertheless, some useful information can be extracted. The most relevant piece of information offered by these data is that the average SMD of the droplets in the spray decreases with injection pressure. For the open injector this reduction is significant: the maximum SMD is reduced from 400 μm at an injection flow rate of 18 g/s to 70 μm at an injection flow rate of 56 g/s. For the screen injector the change is also significant, with the maximum SMD dropping from 400 μm to 160 μm with a similar change in flow rate. μs

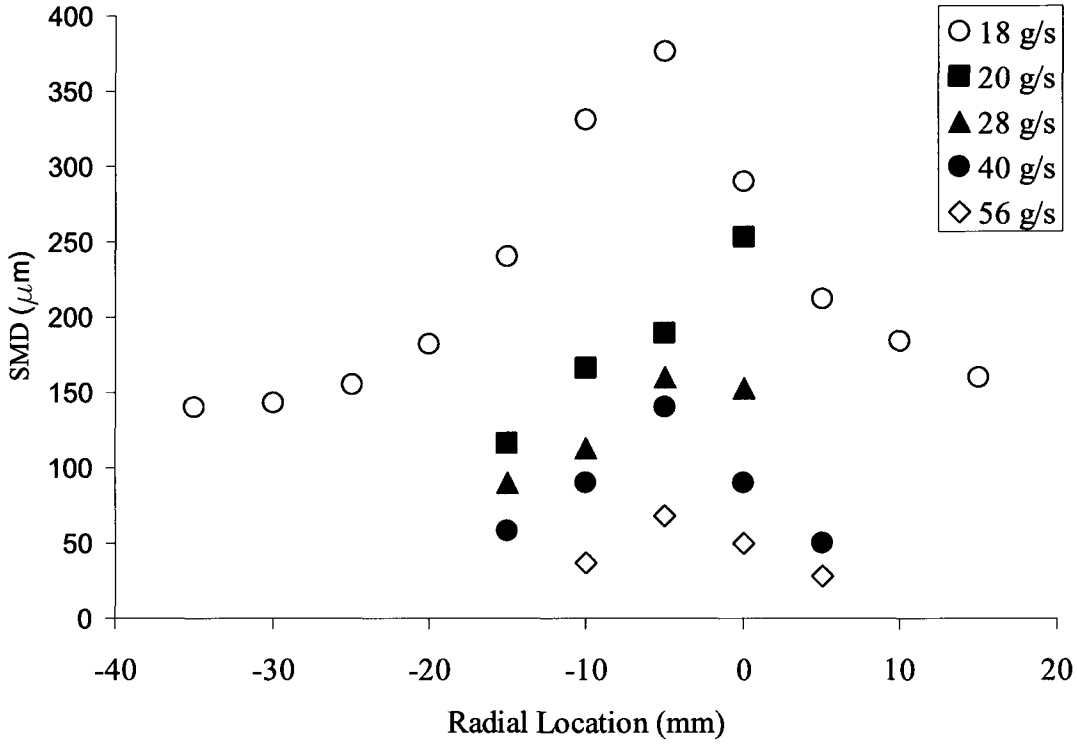

Figure 4.10: Unobstructed injector. Average droplet SMD with radial location measured by the laser diffraction at various injector flow rates at an axial distance of 100 mm.

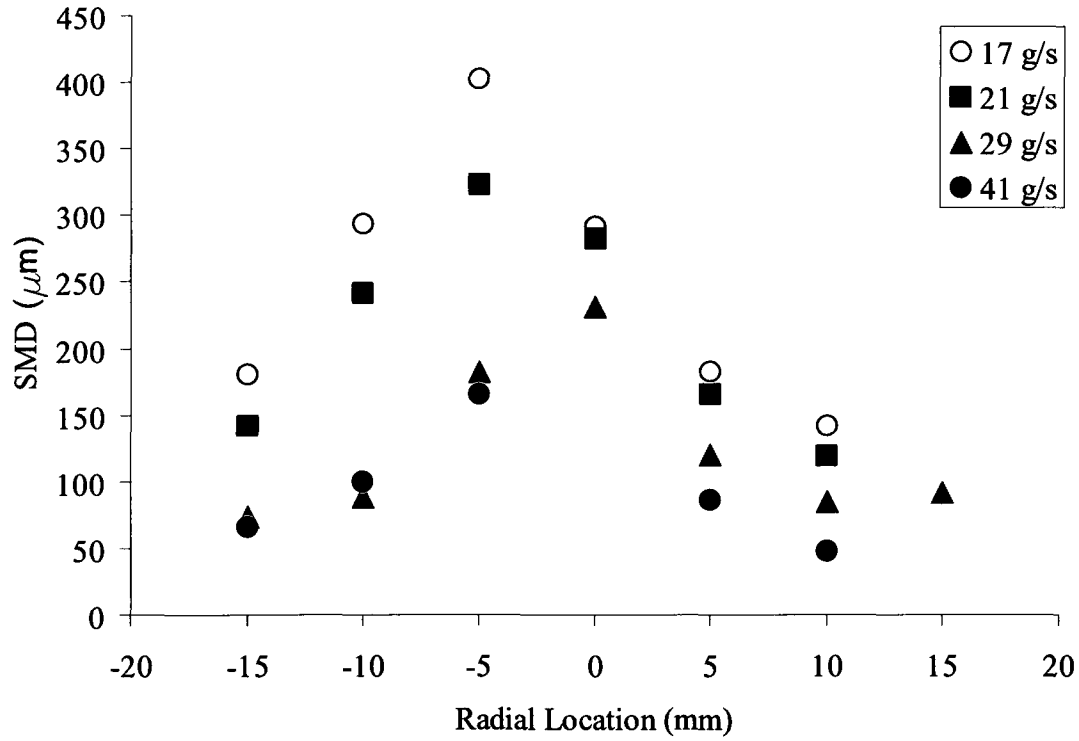

Figure 4.11: Screen injector. Average droplet SMD with radial location measured by the laser diffraction at various injector flow rates at an axial distance of 100 mm.

4.3.2 Phase Doppler Particle Analysis Data

PDPA data differ from laser diffraction measurements. The former are measurements of droplet size and velocity at a discrete location in space, whereas the latter are line of sight averages of only the droplet size. Measurements of the average droplet velocity and SMD for the two flow rates of 19 g/s and 29 g/s for the unobstructed, screen and half obstructed injectors are presented in Figures 4.12 to 4.23.

The velocity measurements confirm that increasing the flow rate results in faster droplet velocities. Furthermore, the faster droplet velocities are observed at the centre of the spray with the particle velocities approaching zero at the edge of the spray. These results are in agreement with results from the literature, specifically those by Stahl et al. (2006).

It is important to note that the spray axis does not always coincide with the geometric axis, as it was apparent in the flow visualization images. As a result, it became necessary to determine the location of the fastest moving particles, so that the true spray axis could be defined. The unobstructed and screen obstructed injectors produce sprays that are symmetric about the nozzle's geometric axis. The half unobstructed objector, however, produces a spray whose axis does not align with the nozzle, and is located 10 mm away from the geometric centreline at an axial location of 150 mm.

The measured droplet size distribution is also compatible with the expected trend: the average droplet diameter is reduced with an increase in liquid flow rate. Greater injector mass flows produce faster fluid exit velocities, which in turn result in larger shearing forces between the quiescent air and the liquid. These larger shearing forces fracture the liquid into smaller particles.

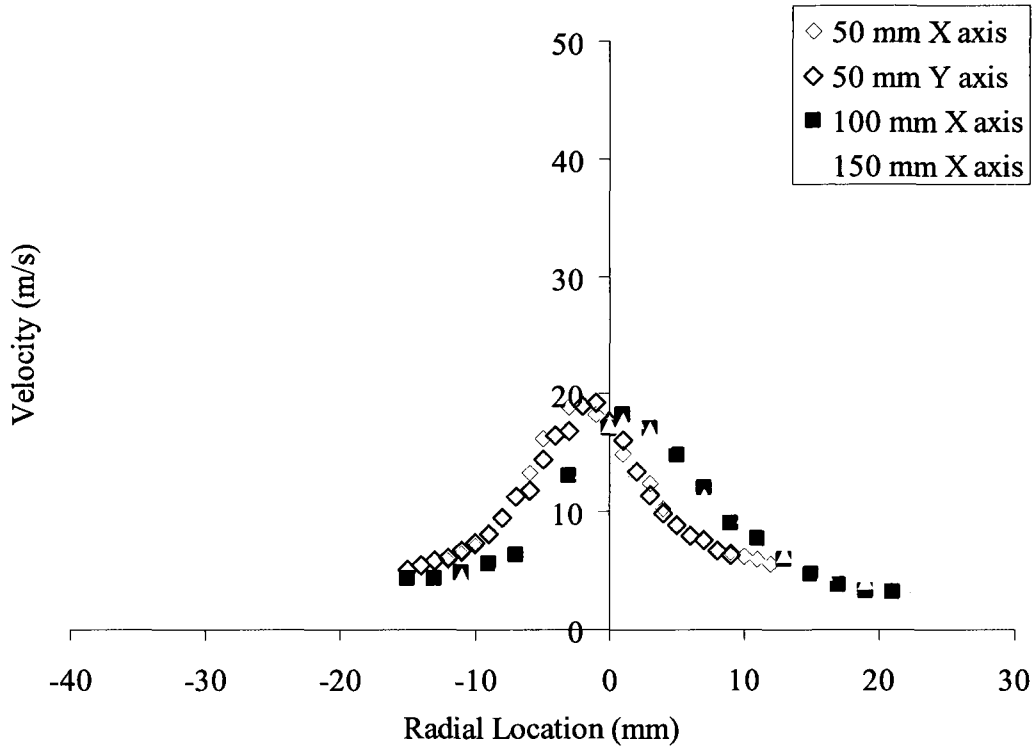

Figure 4.12: Unobstructed injector. Average droplet velocity with radial location measured by PDPA at various axial distances for a flow rate of 19 g/s and 212 kPa.

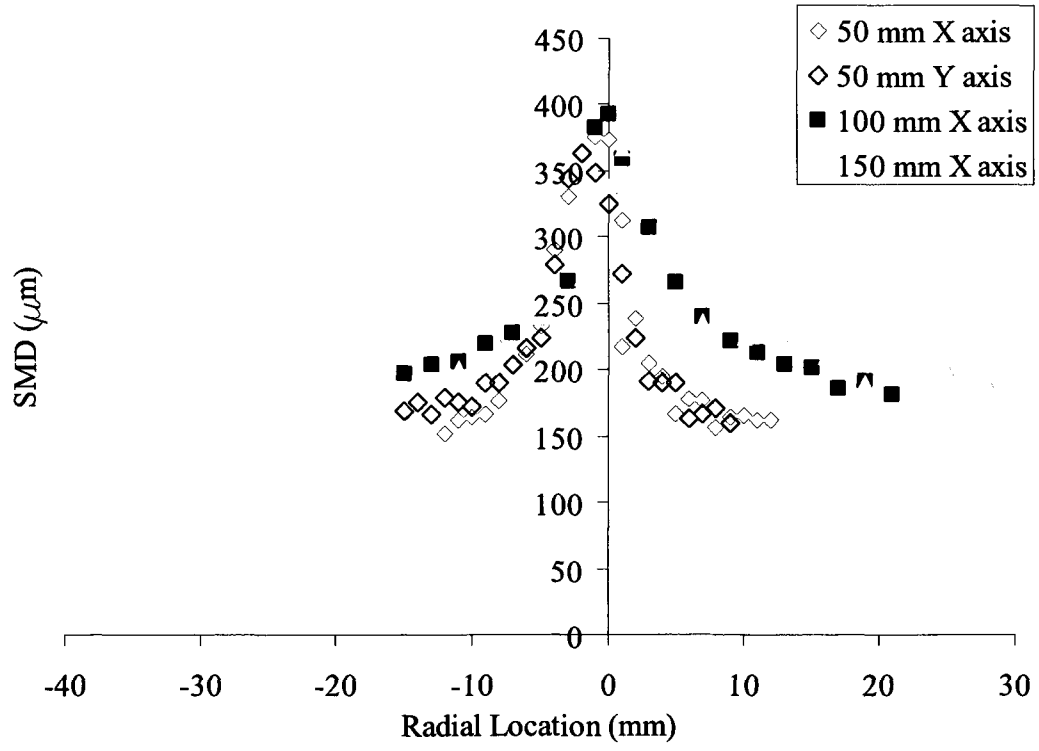

Figure 4.13: Unobstructed injector. Mean droplet SMD with radial location measured by PDPA at various axial distances for a flow rate of 19 g/s and 212 kPa.

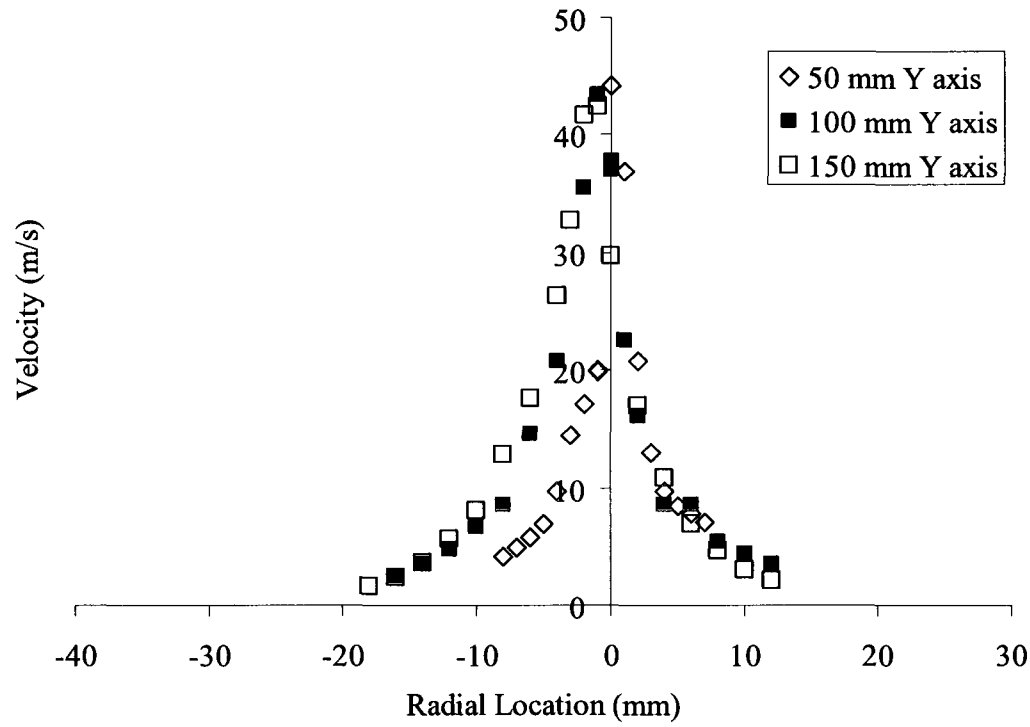

Figure 4.14: Unobstructed injector. Average droplet velocity with radial location measured by PDPA at various axial distances for a flow rate of 29 g/s and 687 kPa.

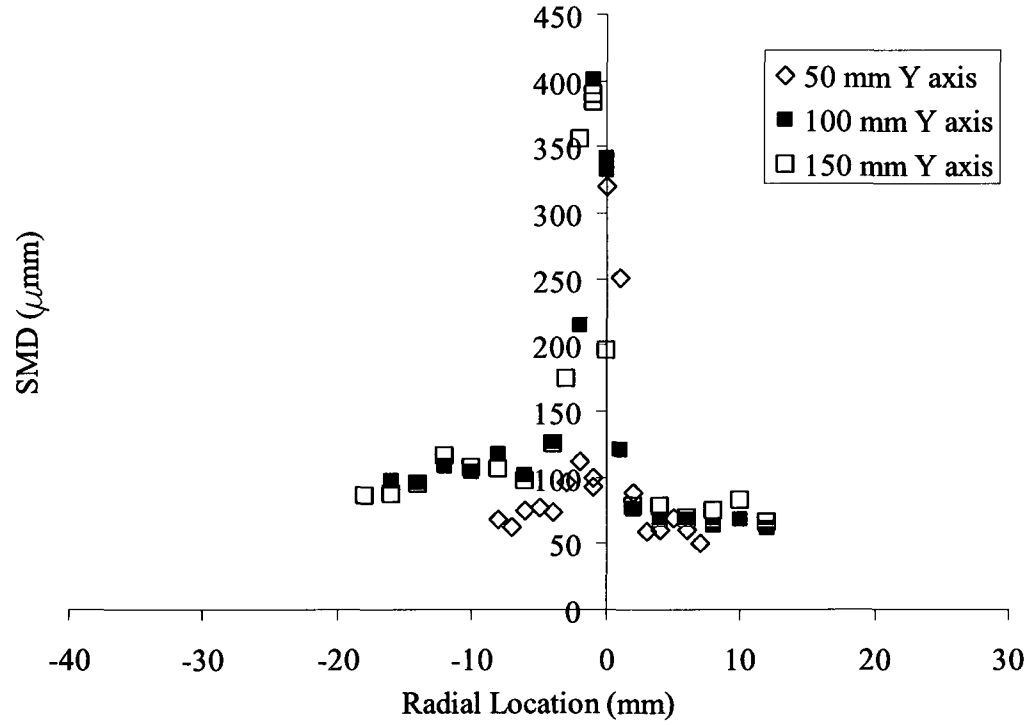

Figure 4.15: Unobstructed injector. Average droplet SMD with radial location measured by PDPA at various axial distances for a flow rate of 29 g/s and 687 kPa.

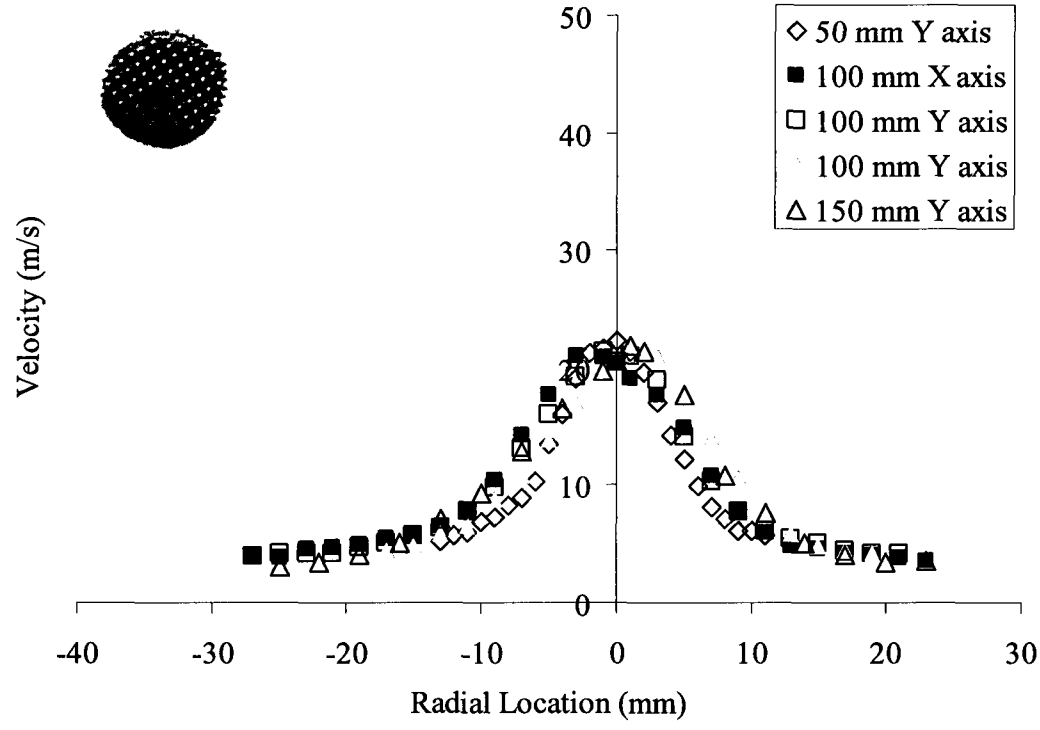

Figure 4.16; Screen obstruction. Average droplet velocity with radial location measured by PDPA at various axial distances for a flow rate of 19 g/s and 583 kPa.

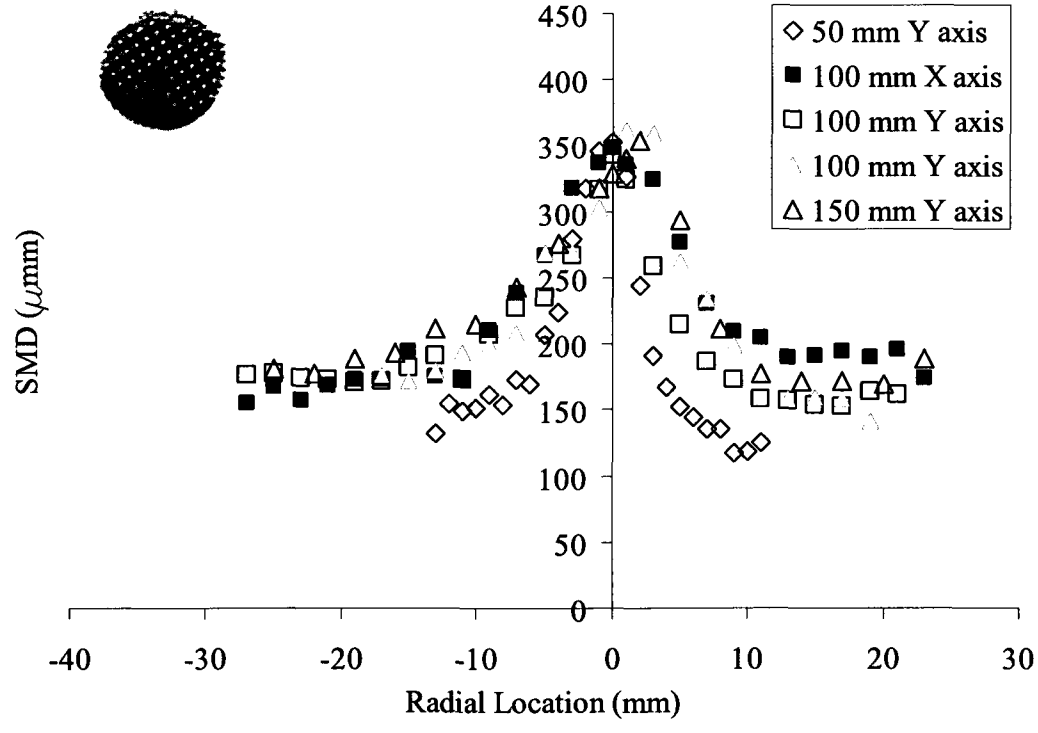

Figure 4.17: Screen obstruction. Average droplet SMD with radial location measured by PDPA at various axial distances for a flow rate of 19 g/s and 583 kPa.

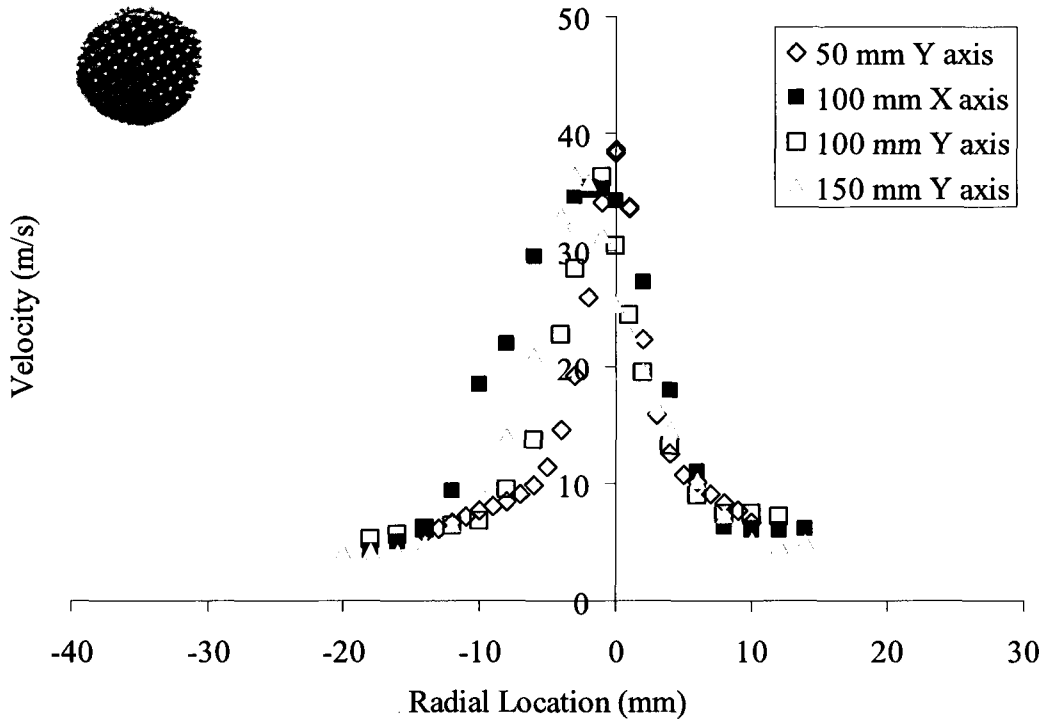

Figure 4.18: Screen obstruction. Average droplet velocity with radial location measured by PDPA at various axial distances for a flow rate of 29 g/s and1267 kPa.

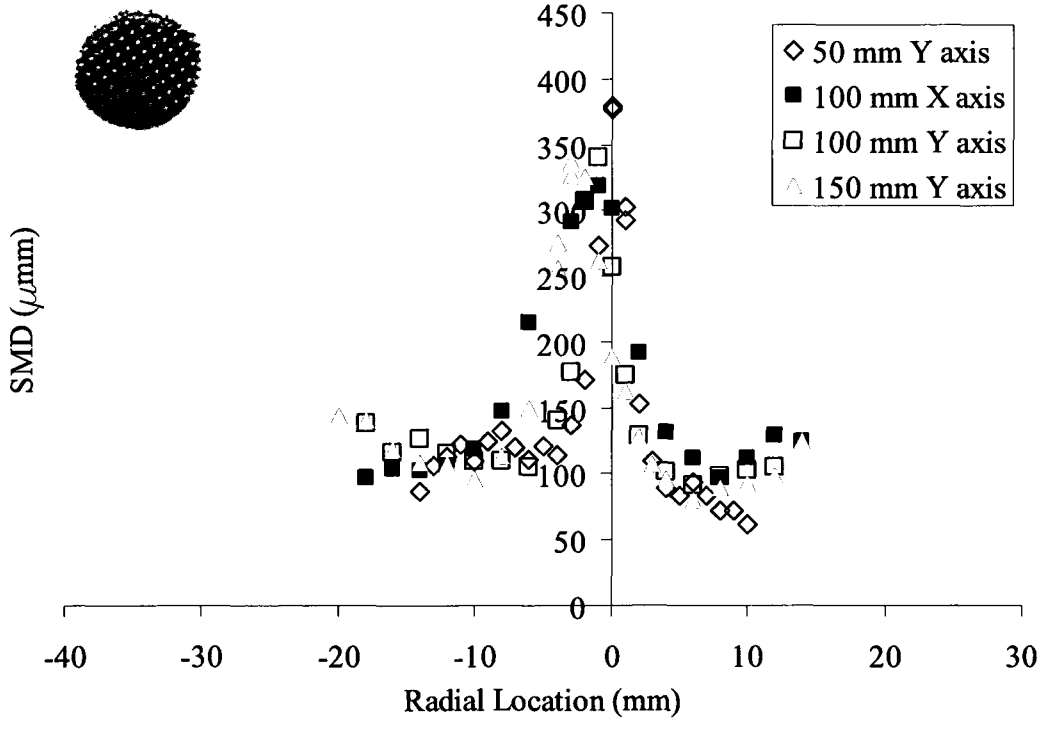

Figure 4.19: Screen obstruction. Average droplet SMD with radial location measured by PDPA at various axial distances for a flow rate of 29 g/s and1267 kPa.

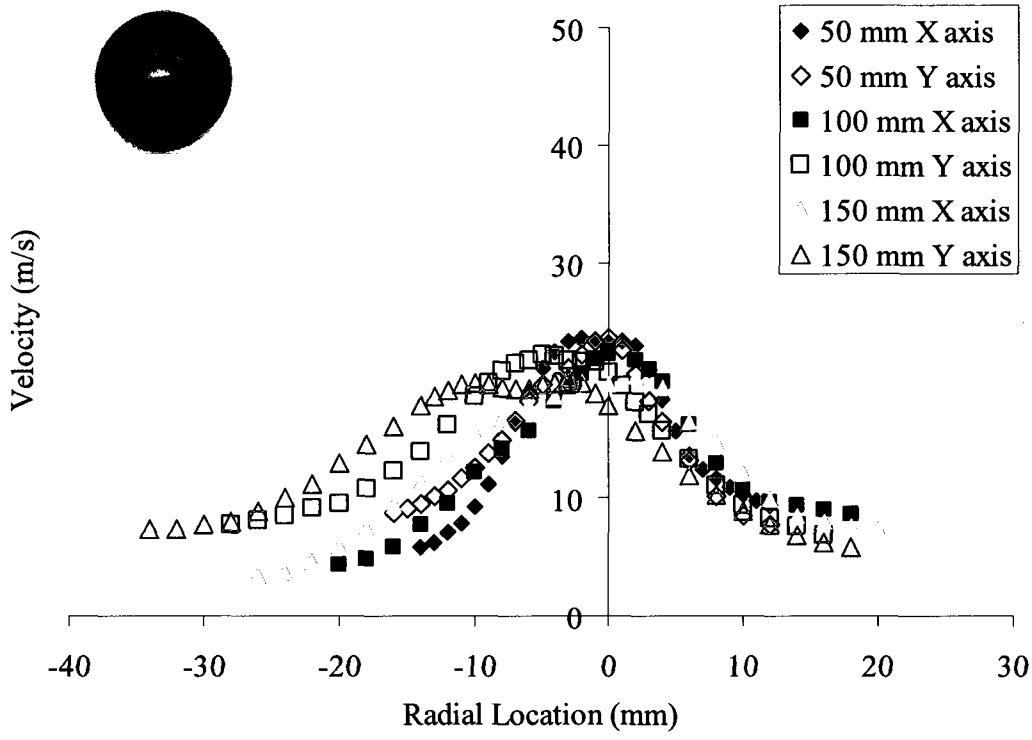

Figure 4.20: Half obstruction. Average droplet velocity with radial location measured by PDPA at various axial distances for a flow rate of 19 g/s and 1081 kPa.

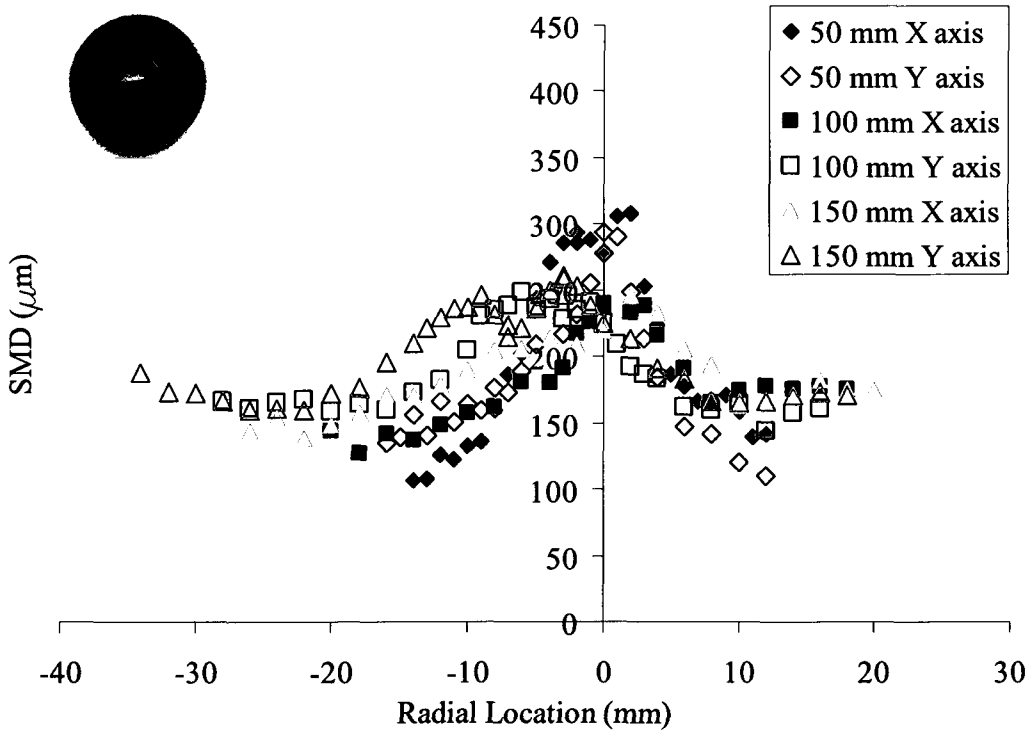

Figure 4.21: Half obstruction. Average droplet SMD with radial location measured by PDPA at various axial distances for a flow rate of 19 g/s and 1081 kPa.

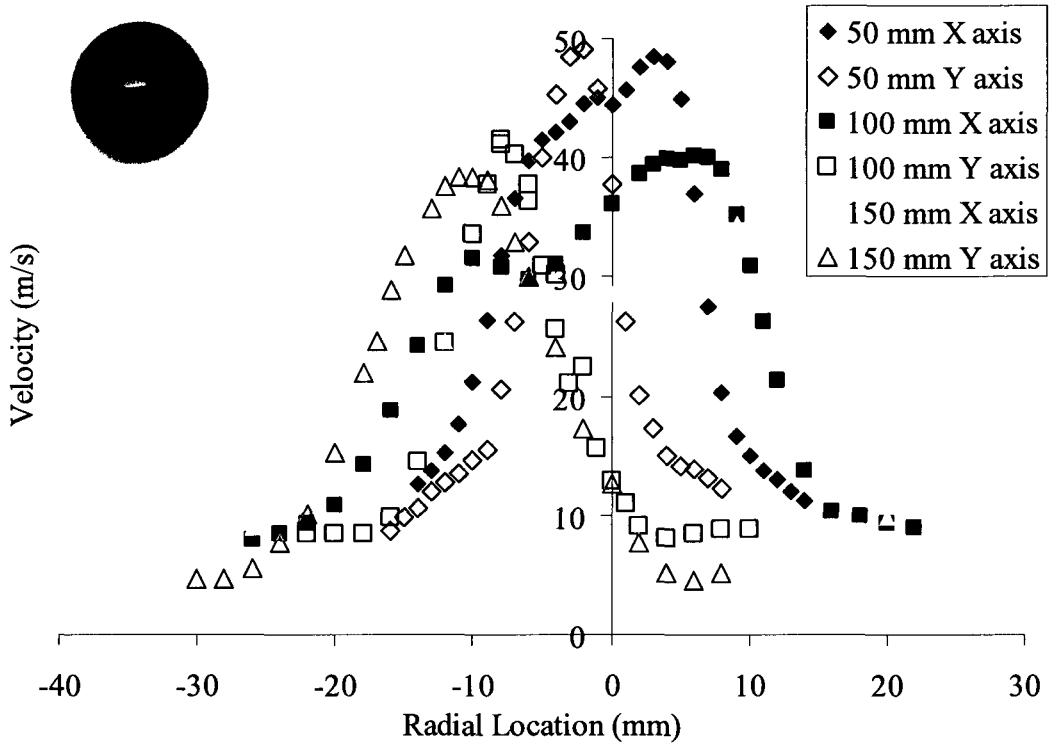

Figure 4.22: Half obstruction. Average droplet velocity with radial location measured by PDPA at various axial distances for a flow rate of 29 g/s and 2243 kPa.

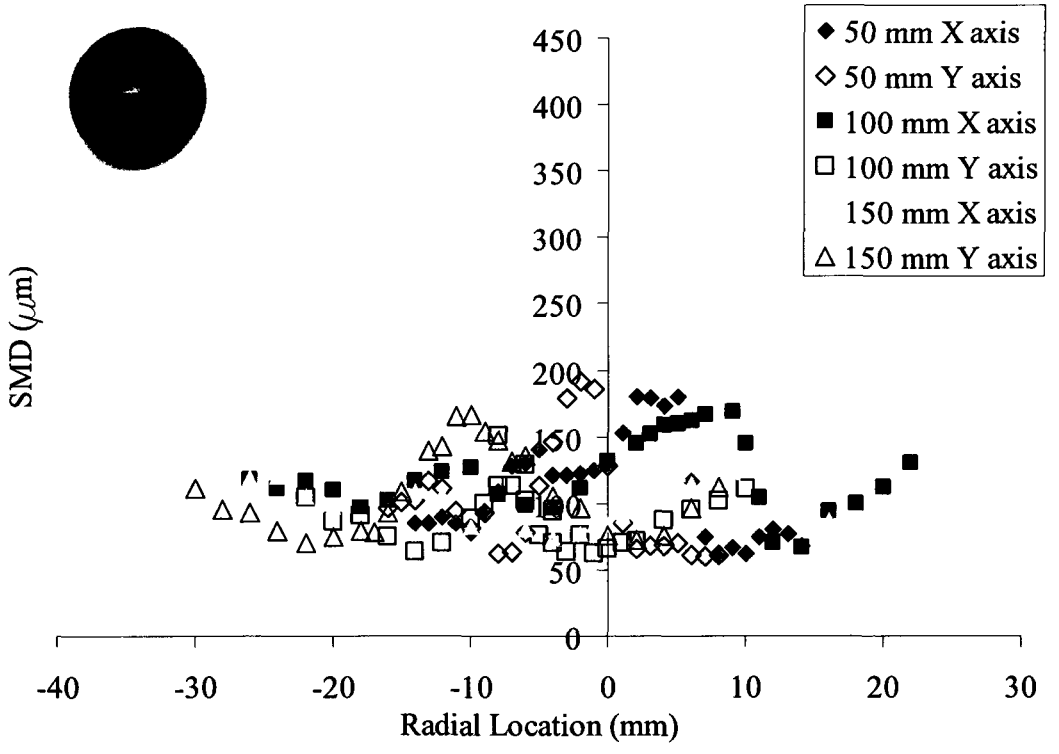

Figure 4.23: Half obstruction. Average droplet SMD with radial location measured by PDPA at various axial distances for a flow rate of 29 g/s and 2243 kPa.

Chapter 5 – Analysis and Discussion

5.1 Injector Flow Losses

The results of flow checks on the various injector configurations showed that, for a given pressure, the larger the restriction is, the lower the mass flow will be. A measure of the losses incurred by the addition of an obstruction is the discharge coefficient C_d. The discharge coefficients, calculated for all configurations and all flow conditions, are shown in Figure 5.1. All configurations exhibit the same trend: as the Reynolds number increases, the discharge coefficient decreases and approaches a constant value. The initial decrease of the discharge coefficient is associated with an increase in frictional losses, which stabilize at relatively large Reynolds numbers.

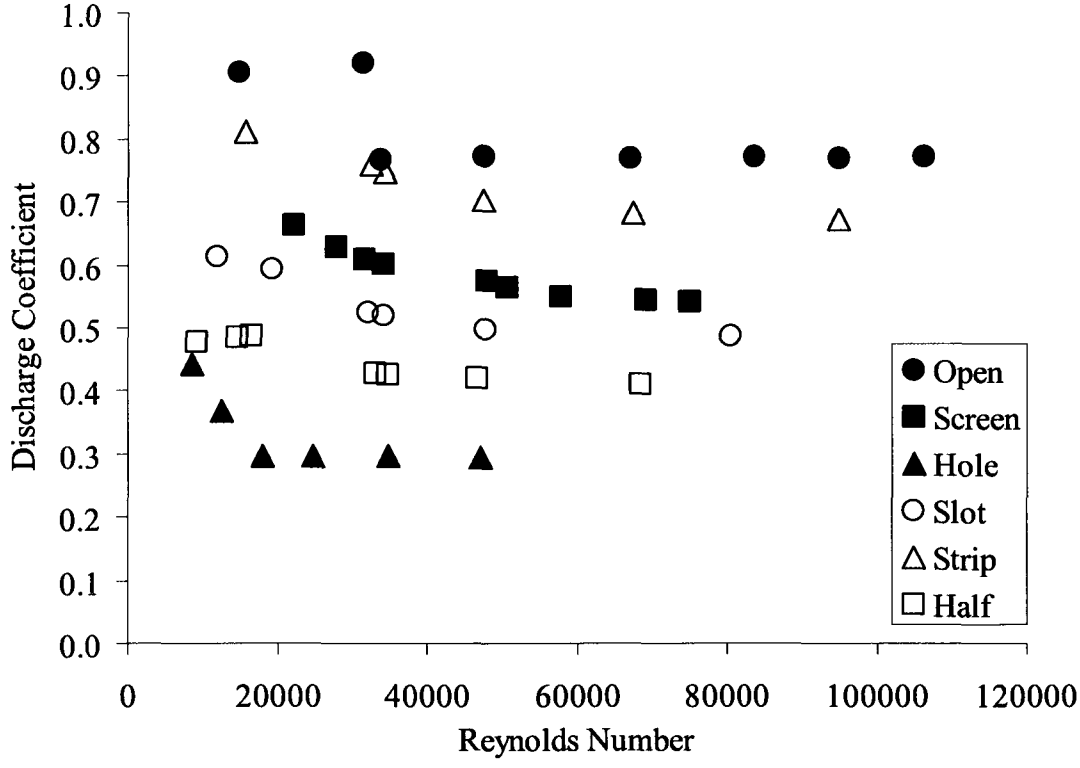

Figure 5.1: Discharge coefficients vs. Reynolds number for the tested injectors.

From Figure 5.1 the discharge coefficient of the unobstructed injector at high Reynolds numbers is approximately 0.8. Using equation (2.5) to predict the theoretical maximum C_d for this injector gives a value of 0.75. One possible explanation for this difference is that the injector used is not exactly a sharp-edged orifice, but as seen in Figure 3.2, the entry to the hole has a 0.3 mm radius. This geometry should have slightly lower losses than a sharp transition between the sac and capillary, resulting in a higher discharge coefficient. The uncertainty of the discharge coefficient was calculated for the open, screen and half obstructions, at the 19 g/s and 29 g/s condition. It was found to be no greater than +/- 0.032. A sample of the calculation is shown in Appendix A.

When the obstructions are introduced to the nozzle geometry, they result in more head loss and consequently reduce the discharge coefficient of the injector. In addition, the presence of the obstruction produced more cavitation, which effectively reduces the exit area of the injector, also reducing the discharge coefficient. With the current diagnostics it is impossible to separate how much of the reduction is in the discharge coefficient is due to the obstruction and how much is due to the increase in cavitation. It can be concluded that the cavitation is likely the larger component since the open area of the hole obstruction 6% greater than the half obstruction's, but the reduction in discharge coefficient once cavitation occurs is 25%.

5.2 Flow Visualization

Based on the flow visualization results presented in the last chapter, the internal injector flows can be classified into five categories. These are shown if Figure 5.2 along with their accompanying sprays. The first category is a non-cavitating flow and is of little interest in this work. It will occur in any injector at sufficiently low liquid flow rates. The resulting liquid jet is a column of fluid with no observable atomization.

In the second category, cavitation was observed to occur just downstream of the screen, slot and half obstructions. In these cases, the local pressure in the wake behind the obstruction is lower than the vapour pressure of the working fluid, causing the flow to cavitate. A large concentration of cavitation bubbles can be seen just downstream of the obstruction with a few bubbles propagating down the capillary. The effect on the spray is an improvement in atomization and widening of the spray cone angle.

The third category of internal flow observed is local cavitation formation at the entrance to the capillary. Similar to the previous case, the local pressure in the separated flow region just downstream of the sac is lower than the vapour pressure, resulting in cavitation. Also similar to the previous case, cavitation bubbles can be seen propagating downstream. The effect on the spray is an increase in atomization. Unlike the previous case, however, the exact circumferential location of cavitation is unclear. As a result, the spray will typically become asymmetrical. Furthermore, this cavitation mode is unstable. Pockets of gas may form in several locations, and then disappear, only to begin again at another location which will result in unsteady behaviour of the liquid jet.

The fourth category is "hydraulic flip". In this case, the flow appears to have separated completely from the capillary wall. The result is a suppression of the atomization with a smooth liquid column emerging from the injector.

The fifth category is the occurrence of a large amount of cavitation that appears to fill the capillary with vapour bubbles. Unfortunately, there is very little information in the images of this flow condition. The effect on the spray is a further increase in the atomization to the previous modes.

From the results shown in Table 4.1, the maximum velocity tested is 73 m/s. At this speed, a bubble that is following the flow will travel the length of the capillary in 137 μs, so that it may be photographed only once before it exits the injector. Furthermore, during the exposure time, it will travel a distance of 5.4 mm. This can explain why the dark lines appear inside the injector once cavitation has occurred. Even at the lower flow rates, the maximum acquisition time of the video camera is not fast enough to freeze the motion of the flow.

It should also be noted that the onset of cavitation typically occurs at a given pressure and not a particular mass flow rate. Furthermore, the cavitation mode does not appear to be firmly correlated with the flow rate. Figure 5.3 compares the internal flows of the unobstructed and screen obstructed nozzles. Despite having comparable flow rates, the two patterns of cavitation are drastically different. At the 13 g/s flow rate, in the unobstructed case there is a large amount of cavitation in the centre of the capillary, whereas for the screened injector the cavitation occurs at the entrance to the capillary. Increasing the flow rate to 29 g/s reduces the volume of gas in the unobstructed injector, but significantly increases the volume of gas for the screen injector.

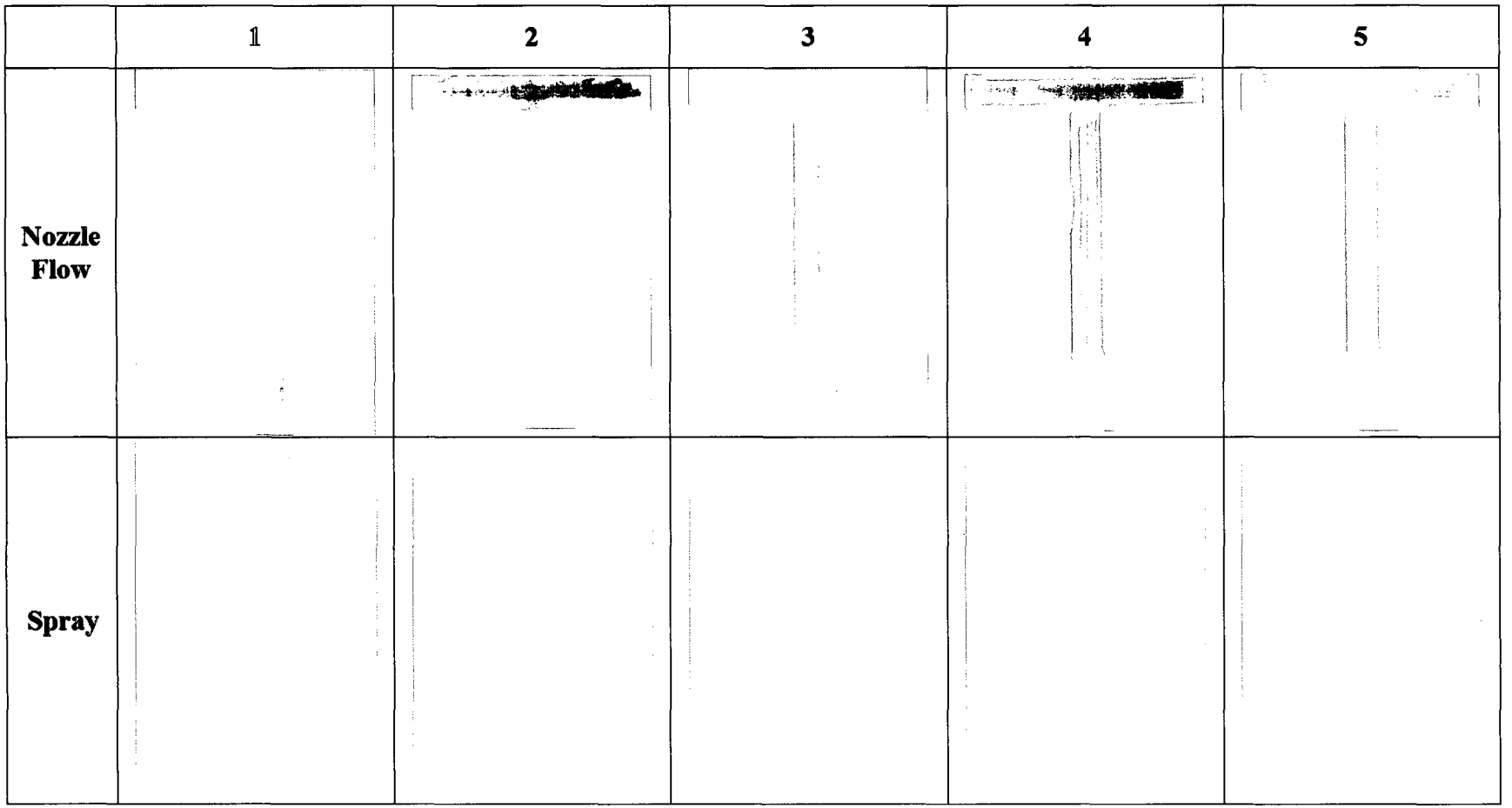

Figure 5.2: The five categories of internal nozzle flows. 1. No cavitation. 2. Onset of cavitation at the hole inlet due to obstruction. 3. Onset of cavitation with local separation. 4. Hydraulic Flip. 5. Capillary filled with cavitation bubbles.

Figure 5.4 illustrates how the images were processed for estimating the void fraction at the exit of the injector. The image is first cropped so that only the capillary is remaining. The image is then converted to grey scale. The intensity of each pixel in the last pixel row of this image is determined, and then averaged to determine the average pixel intensity across the exit plane of the injector. This value is then normalized by the average pixel intensity of the low flow case, which is free of cavitation, to determine percentage pixel intensity. Because the liquid appears light and the cavitation region appears dark, a percentage pixel intensity of 100% would indicate a flow that is 100% liquid, while a result of 0% would indicate a flow that is 100% gaseous. The results for the unobstructed, screen and half injectors are shown in Figure. 5.5.

Flow Condition	19g/s – 200 kPa	29 g/s
Unobstructed	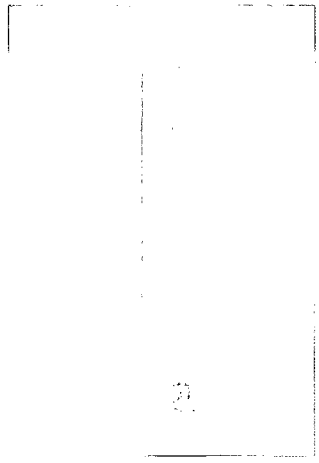	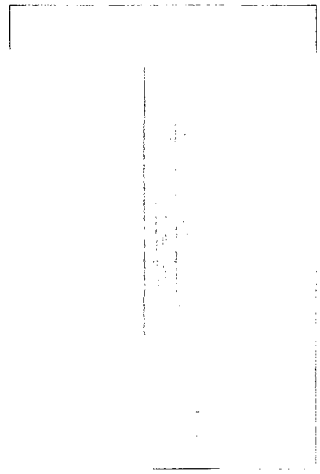
Flow Condition	**13g/s – 200 kPa**	**29 g/s**
Screen		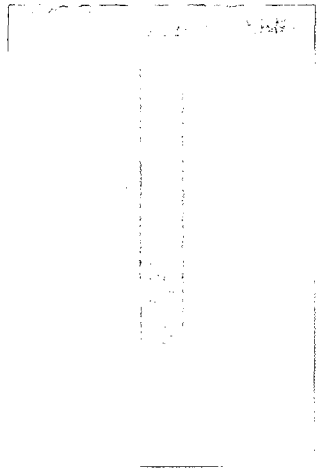

Figure 5.3: Unobstructed and screen obstructed injector internal cavitating flow structures.

Figure 5.4: Illustration of steps in the image processing.

	Unobstructed			Screen			Half		
Flow	19 g/s	29 g/s	40 g/s	19 g/s	29 g/s	40 g/s	19 g/s	29 g/s	40 g/s
Image of flow in capillary	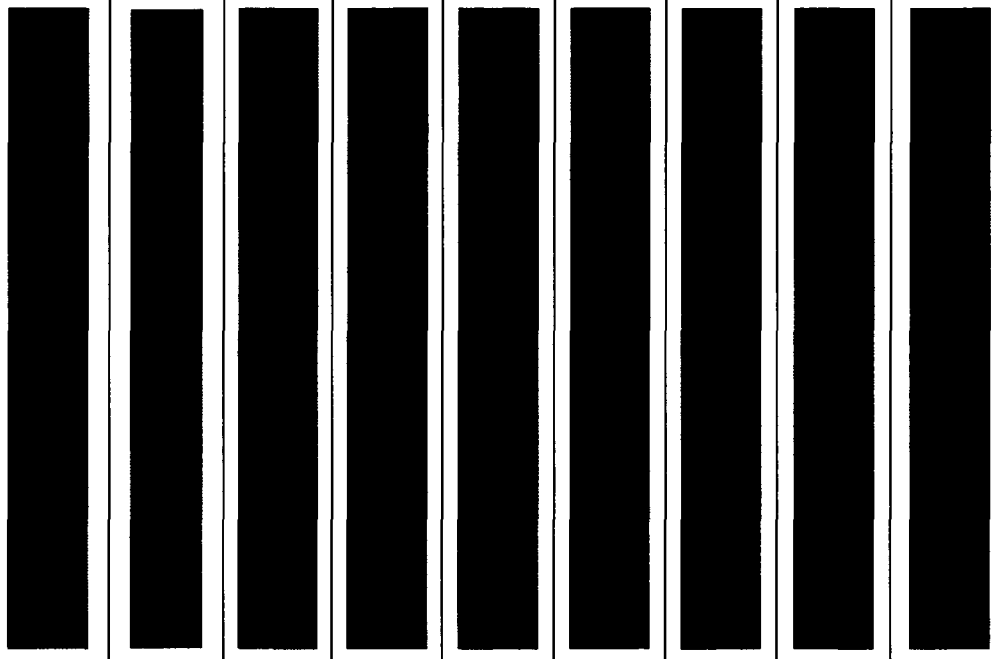								
Pixel intensity	56.83	51.28	40.50	46.31	36.44	31.88	33.96	28.88	27.88
% Pixel Intensity	89.76	81.00	63.97	73.15	57.56	50.35	53.65	45.63	44.04

Figure 5.5: Images of the flow in the capillary for the unobstructed, screen and half obstructed injector.

The results in Figure 5.5 indicate that the unobstructed injector has the least amount of cavitation, whereas the half obstructed injector has the most. This correlates with the discharge coefficients calculated in the previous section, as the unobstructed injector has the highest discharge coefficient and the half obstructed injector has the lowest one among the designs considered.

It is important to note that, while the percentage pixel intensity has some correlation to the gas fraction at the exit of the capillary, the previous analysis offers a

one-dimensional description of a two-dimensional flow. As the viewing plane is perpendicular to the exit plane, a cavitation bubble that is present anywhere in the capillary will result in a dark spot on the image. As a result, it is not possible to deduce the location and depth of that pocket of gas. An example is illustrated in Figure 5.6, in which both cases would give similar images, although the void fraction is much greater in the case on the left.

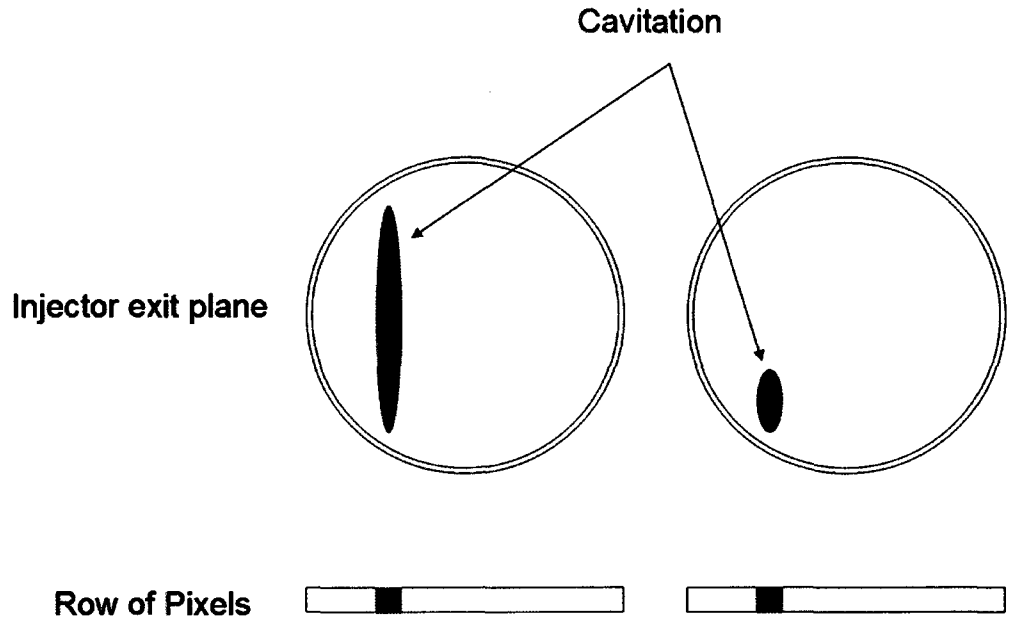

Figure 5.6: Demonstration of the limitations of image analysis.

Figures 5.6 – 5.8 show the internal nozzle flows and the corresponding sprays for the unobstructed, screen and meniscus obstructed injectors. Both sets of images were taken with the Nikon D70s digital SLR camera. These figures help to show that the stronger the obstruction was, the greater the cavitation would be, and consequently the better atomized the spray would become.

	Unobstructed					
	19 g/s		29 g/s		40 g/s	
	Capillary	Spray	Capillary	Spray	Capillary	Spray
Image	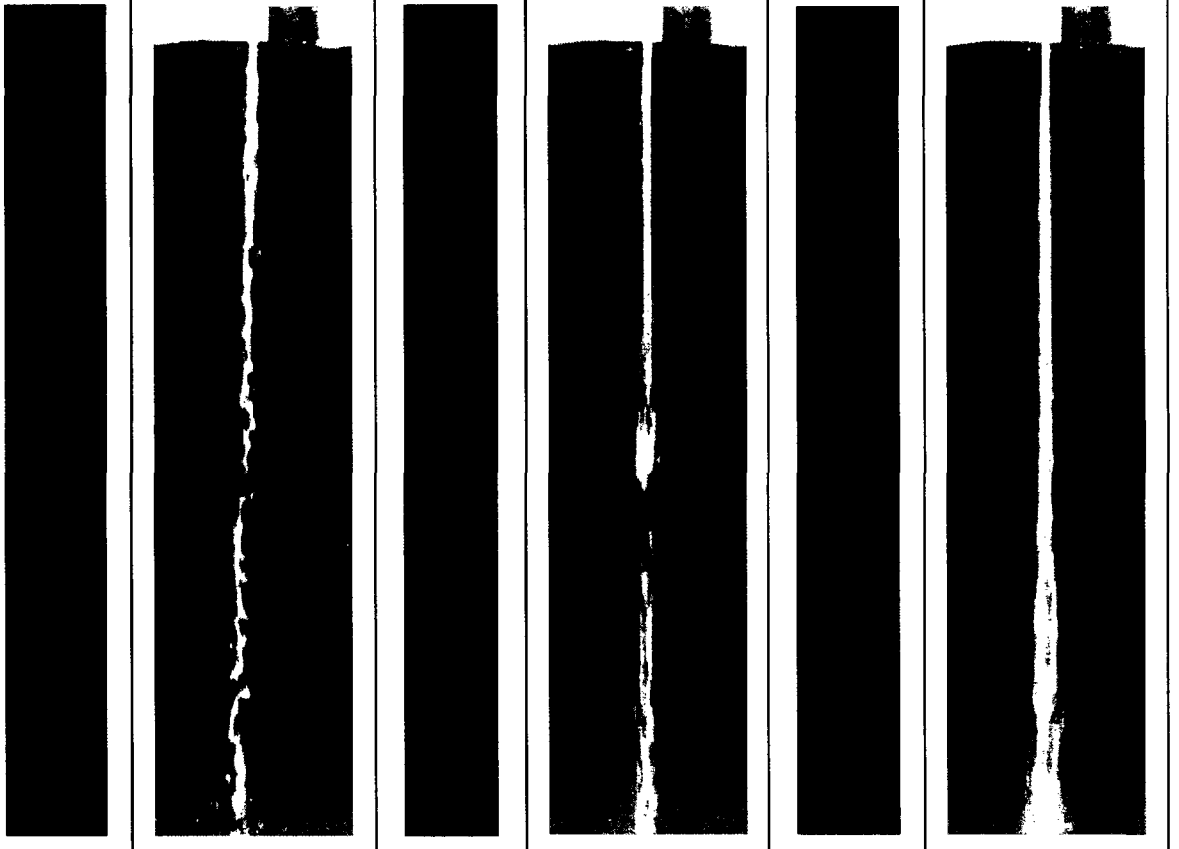					

Figure 5.7: Images of the flow in the capillary and the spray for the unobstructed injector.

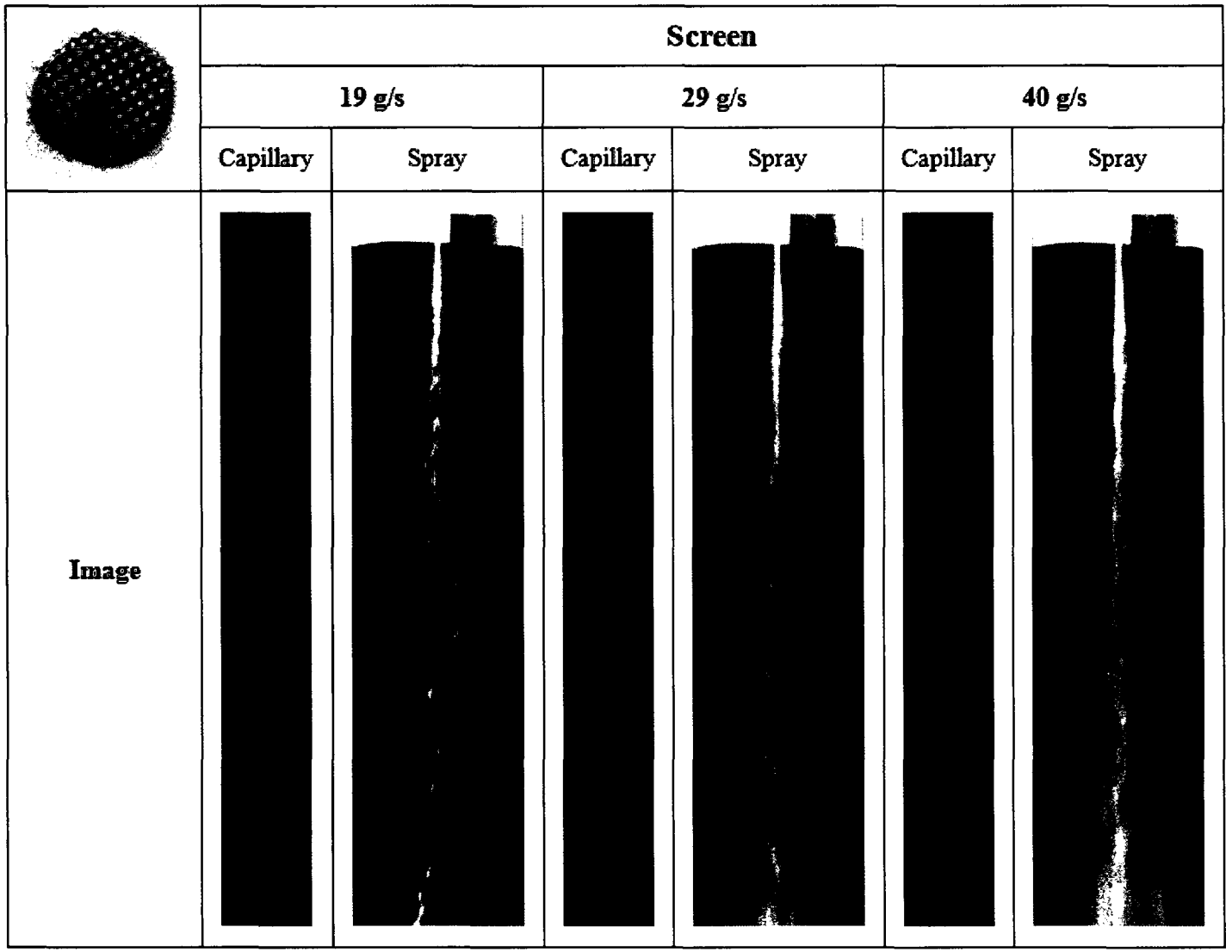

Figure 5.8: Images of the flow in the capillary and the spray for the injector with the screen obstruction.

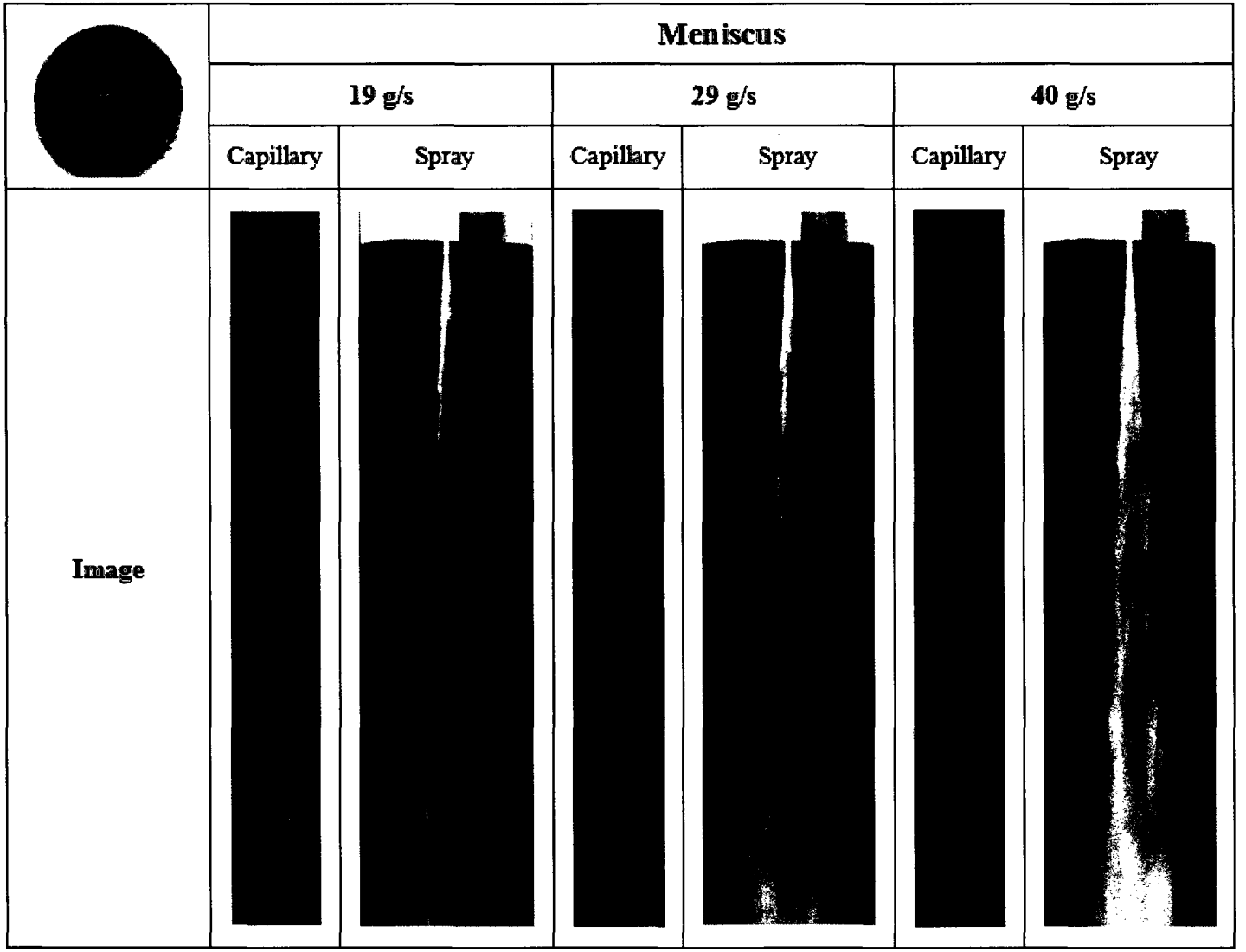

Figure 5.9: Images of the flow in the capillary and the spray for the injector with the meniscus obstruction.

5.3 Spray Droplet Sizing and Velocity

5.3.1 Laser Diffraction Particle Sizing

The droplet sizing results measured by laser diffraction for different nozzles are compared to results for the unobstructed nozzle at approximately the same mass flow rate in Figures 5.5 5.8. Despite the very different cavitation patterns inside these injectors, the droplet sizes are comparable, particularly near the edges of the spray.

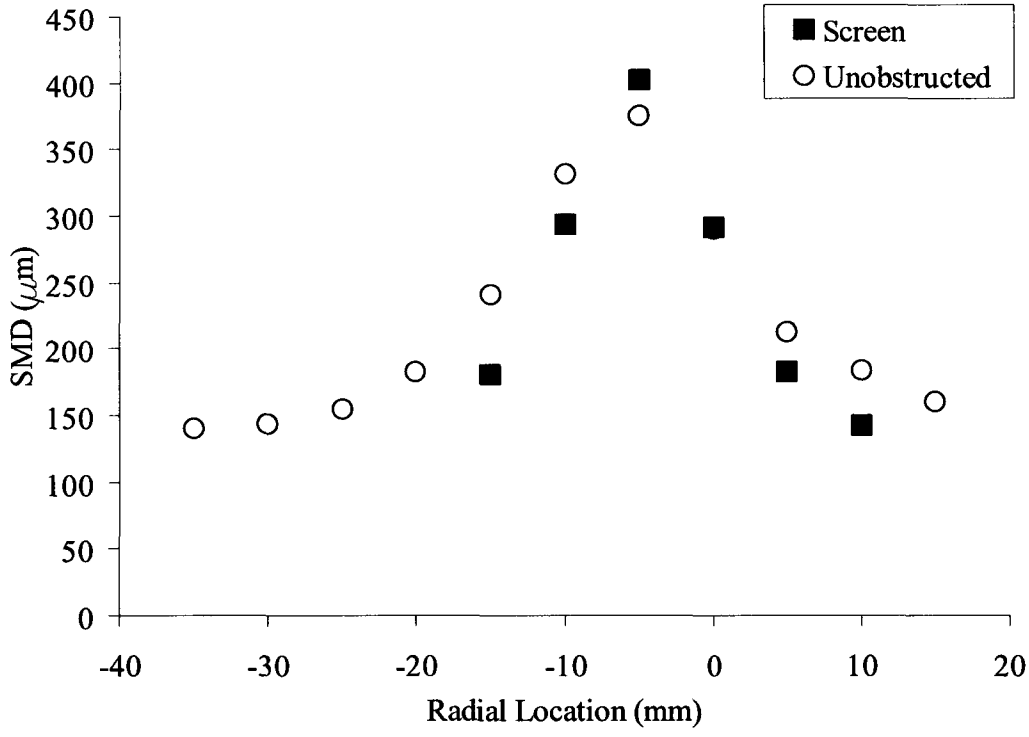

Figure 5.10: Average SMD with radial location measured by the laser diffraction at an axial distance of 100 mm. Unobstructed and screen injector mass flows 19 g/s and 17 g/s.

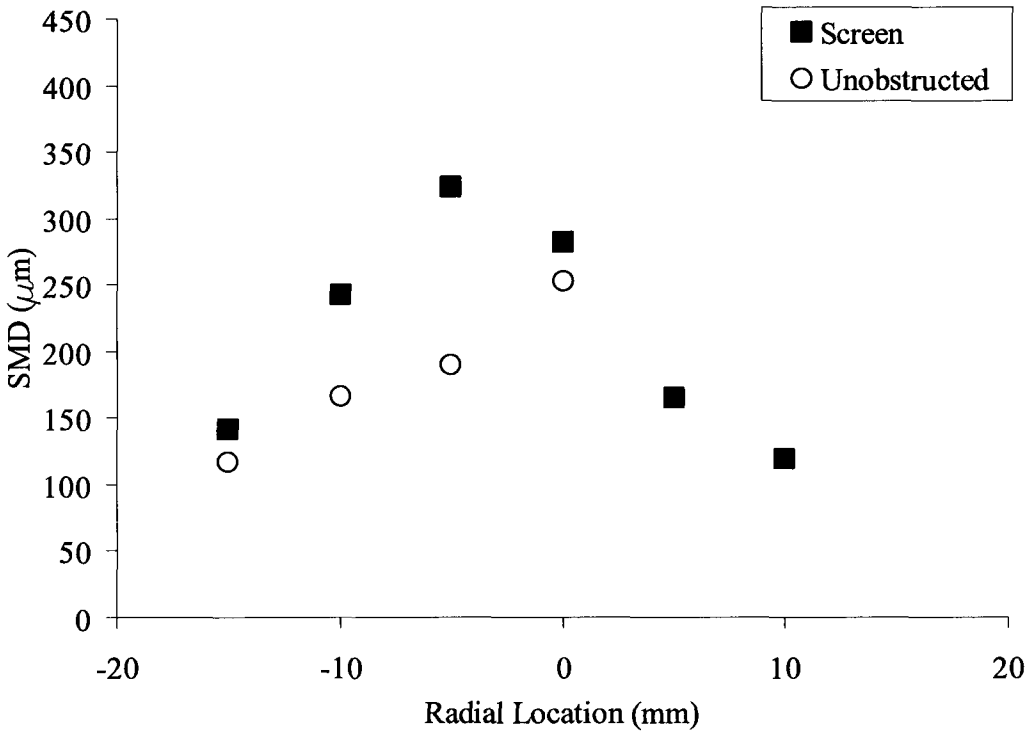

Figure 5.11: Average SMD with radial location measured by the laser diffraction at an axial distance of 100 mm. Unobstructed and screen injector mass flows 20 g/s and 21 g/s.

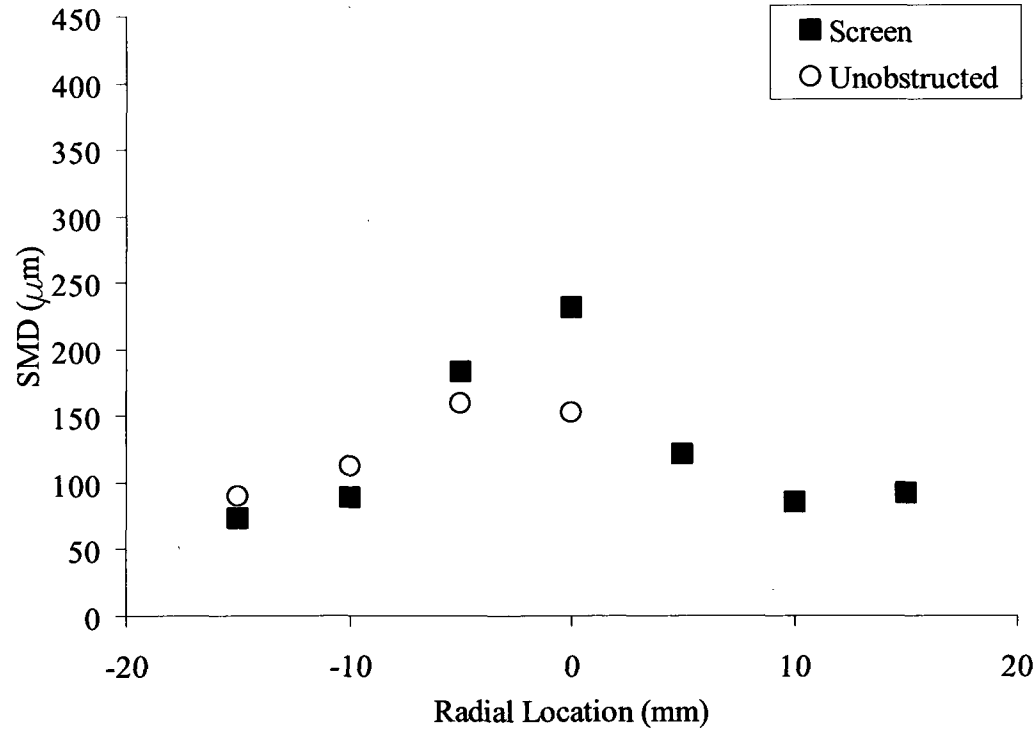

Figure 5.12: Average SMD with radial location measured by the laser diffraction at an axial distance of 100 mm. Unobstructed and screen injector mass flows 28 g/s and 29 g/s.

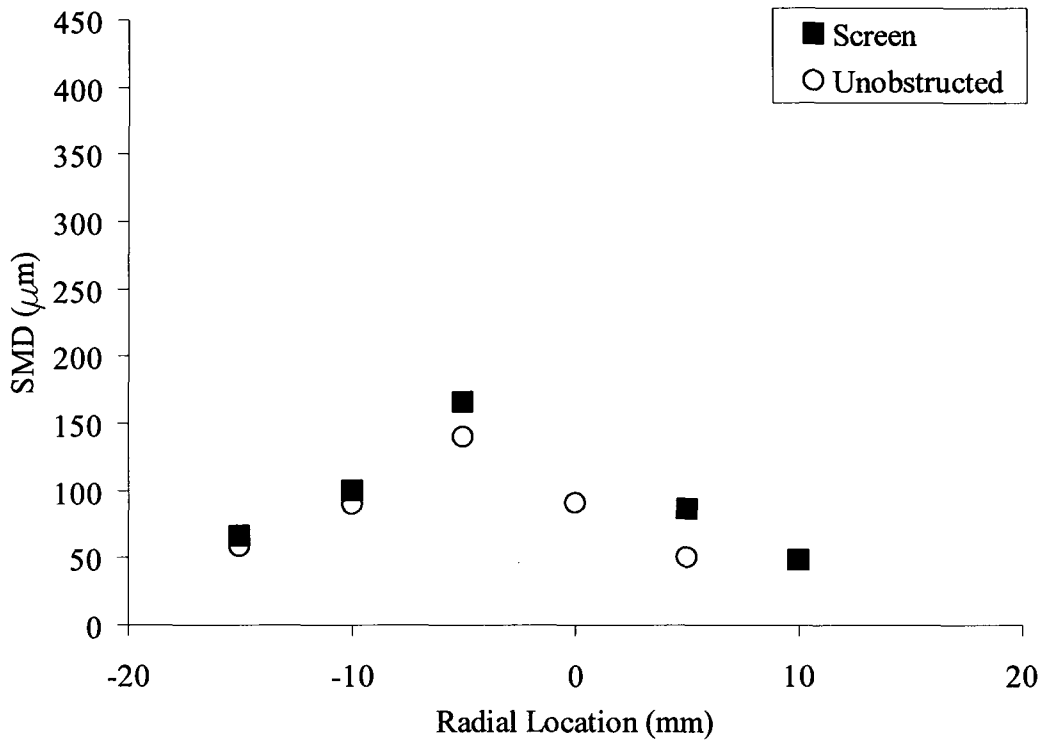

Figure 5.13: Average SMD with radial location measured by the laser diffraction at an axial distance of 100 mm. Unobstructed and screen injector mass flows 40 g/s.

Laser diffraction requires a minimum amount of scattered light in order to make a valid measurement. If there is not a large enough population of droplets to scatter this minimum amount, the measurements may not be reliable. This effectively determines the edge of the spray. Measurements were typically achievable at greater radial distances for the screened injector, indicating that it produces a wider spray. This correlates well with Figures 4.3 and 4.4 which show that the screened injector produces a spray with a wider cone angle at the higher flow rates.

5.3.2 Phase Doppler Particle Analysis Data

The average droplet velocities for the unobstructed, screen and half obstruction are compared at each axial location for the same two flow rates as those used in Figures 5.9

to 5.14. For ease of comparison, the radial profiles have been shifted laterally so that the origin coincides with the axis of the spray. The droplet velocities at any given radial location across the spray show the same trend: the unobstructed injector produces a spray with the slowest droplets, while the half obstruction produces a spray with the fastest droplets. This trend is the same as the trend of discharge coefficients: the open injector has the highest discharge coefficient and the half obstruction has the lowest one. Furthermore, the results shown in Figure 5.5 indicate that the half obstruction has the greatest amount of cavitation at the exit to the injector. This result supports the conclusion of Dumont et al. (2000) that an increase in cavitation decreases the nozzle's exit area, which in turn results in higher injection velocities.

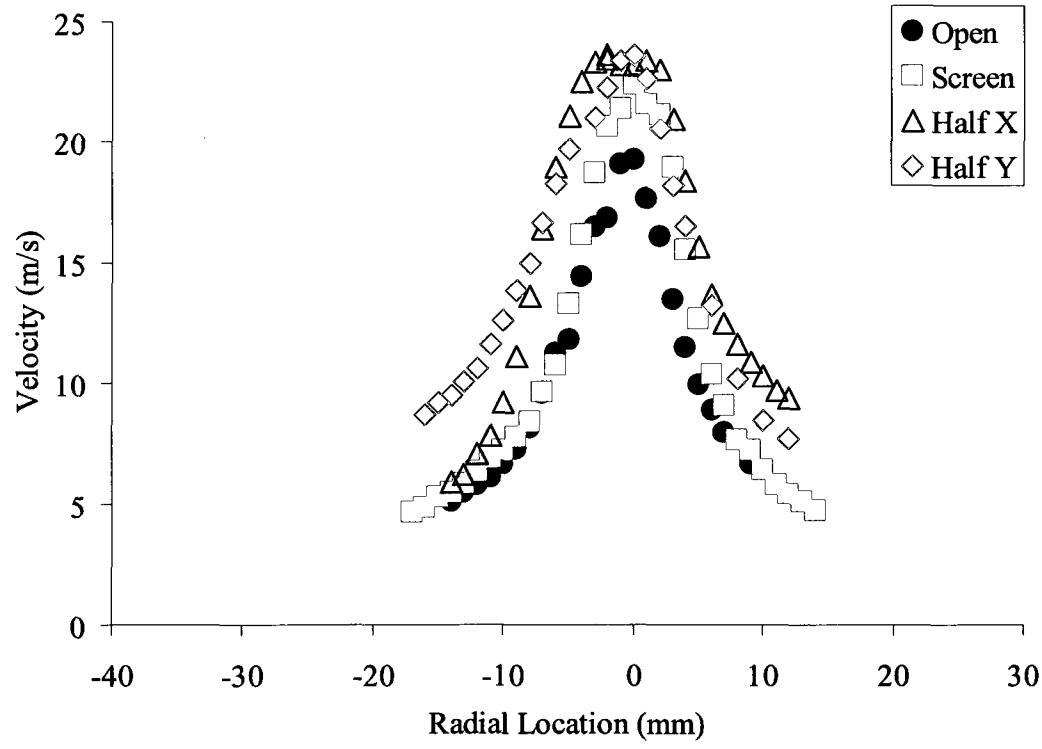

Figure 5.14: Summary average droplet velocity at an axial location of 50 mm measured by PDPA for unobstructed, screen and half obstructed injectors at 19 g/s flow condition.

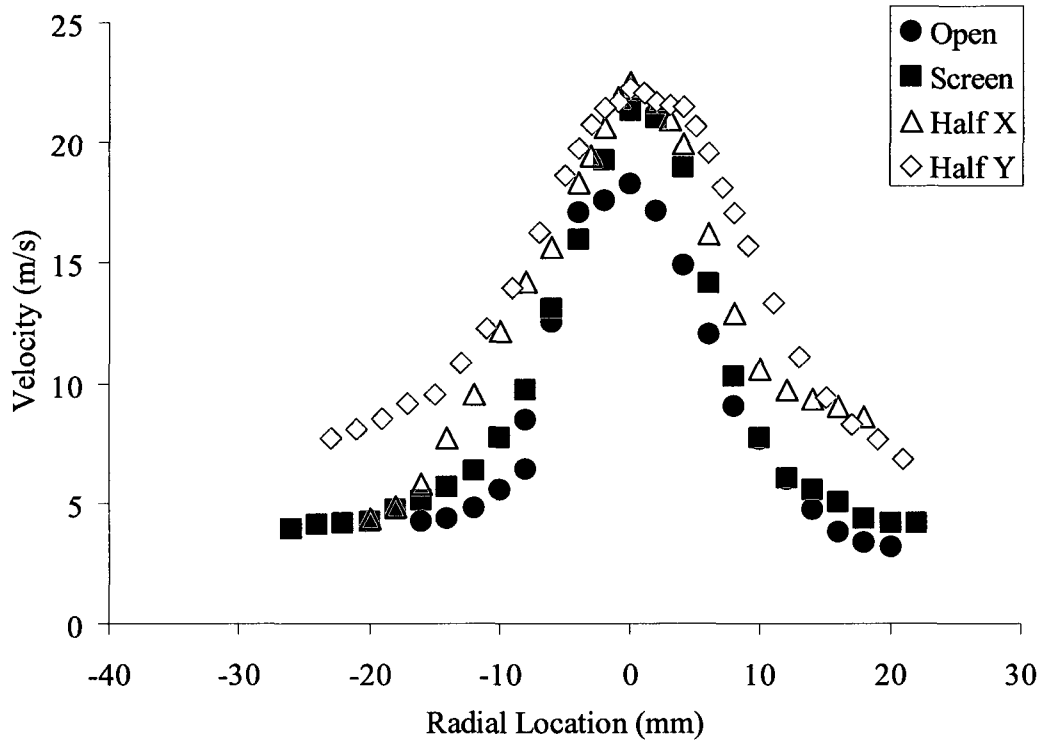

Figure 5.15: Summary average droplet velocity at an axial location of 100 mm measured by PDPA for unobstructed, screen and half obstructed injectors at 19 g/s flow condition.

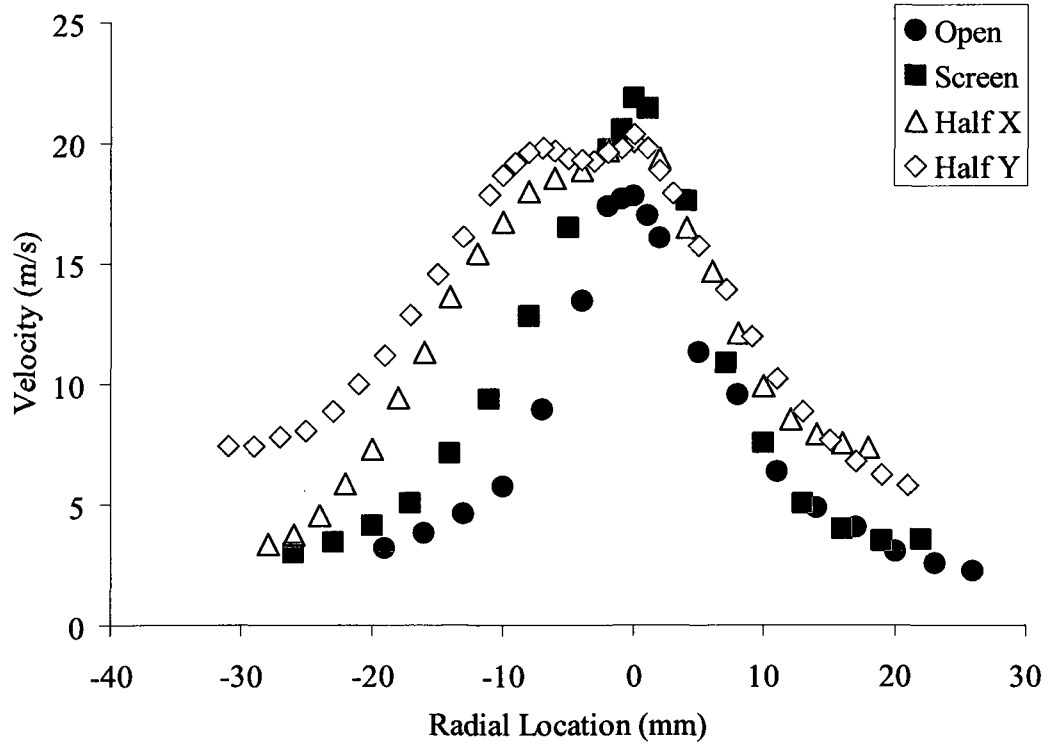

Figure 5.16: Summary average droplet velocity at an axial location of 150 mm measured by PDPA for unobstructed, screen and half obstructed injectors at 19 g/s flow condition.

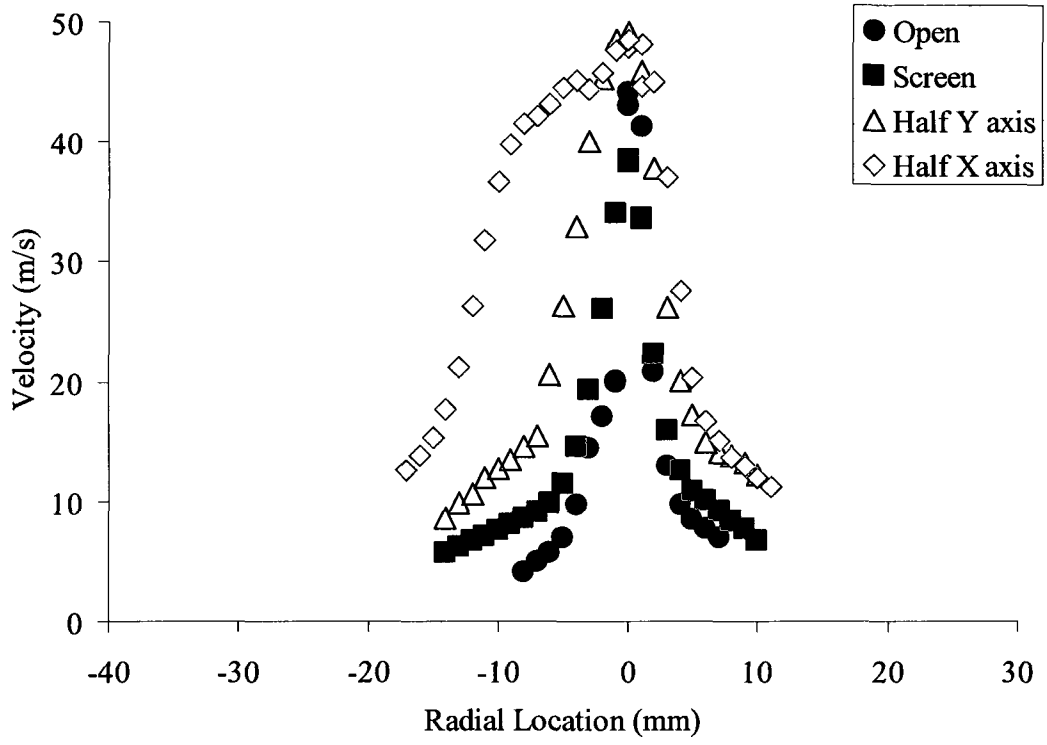

Figure 5.17: Summary average droplet velocity at an axial location of 50 mm measured by PDPA for unobstructed, screen and half obstructed injectors at 29 g/s flow condition.

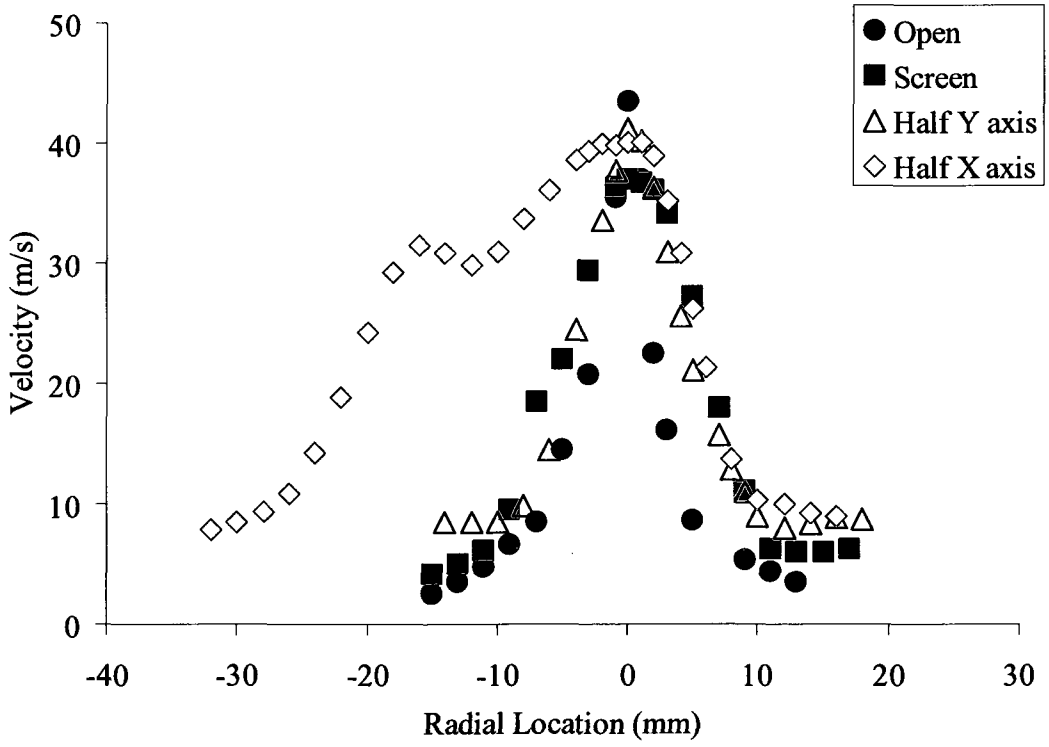

Figure 5.18: Summary average droplet velocity at an axial location of 100 mm measured by PDPA for unobstructed, screen and half obstructed injectors at 29 g/s flow condition.

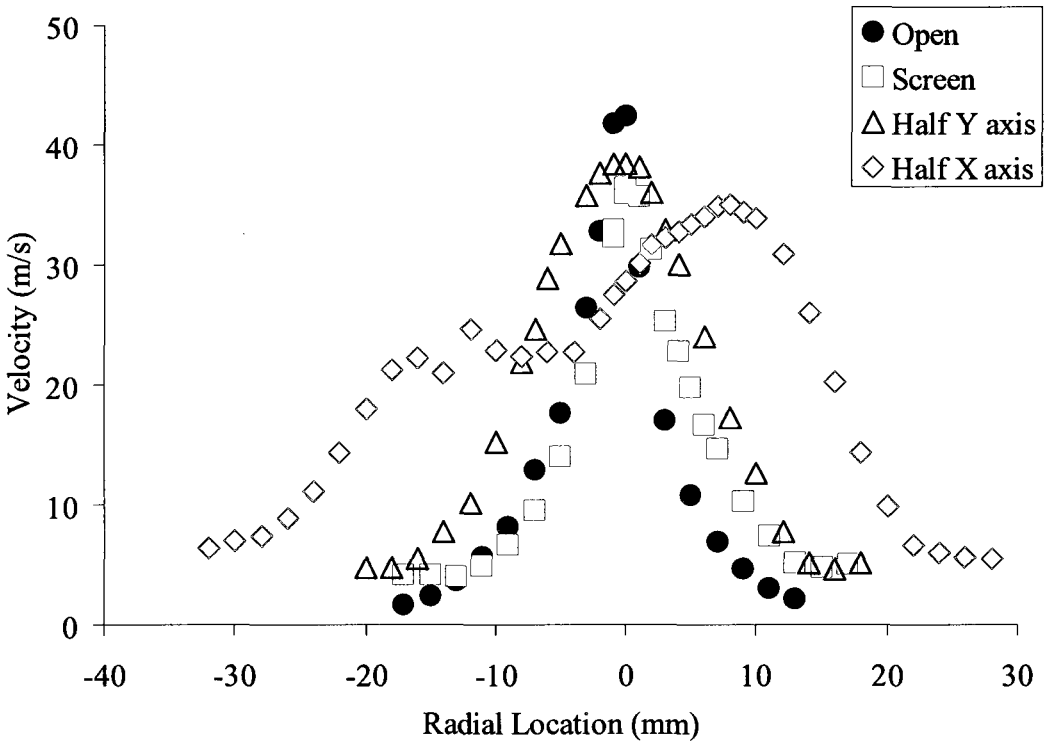

Figure 5.19: Summary average droplet velocity at an axial location of 150 mm measured by PDPA for unobstructed, screen and half obstructed injectors at 29 g/s flow condition.

The average droplet sizing results are shown in Figure 5.15 to 5.20. These data correlate well with the laser diffraction data, which indicated that the droplets increase in size from 100 μm at the edge of the spray to 350 μm at the centre. Droplet size is also observed to decrease as the flow rate increases. These results also correlate with the velocity data presented. The higher injection velocities result in larger shearing forces between the liquid and surrounding air, resulting in the production of smaller droplets.

It should be noted that measurements at the centre of the spray are the most challenging to make and have the highest uncertainty. The PDPA collects the light which is scattered by the droplets, and, because smaller droplets scatter less light, they are more difficult to detect. At the centre of the spray the beams have to penetrate a large volume of fluid to reach the sampling volume, and the light scattered by the droplets has to travel

through a large amount of fluid to reach the detector. Sufficiently small particles may not scatter light with enough intensity to reach the detectors and will go undetected, which would bias the SMD towards larger values.

The large particles detected at the centre of the spray may also be the results of the spray's liquid core not being completely atomized, as seen in flow visualization shown in Figure 2.8. The spray produced by the half obstruction shows droplets at the centre of the spray that are 100 μm to 200 μm smaller than those from the other injectors at every location except for the 50 mm plane at 19 g/s. This is a significant improvement in spray performance, as a shorter core break-up length would result in a wider cone angle, smaller droplets and an overall improvement in atomization.

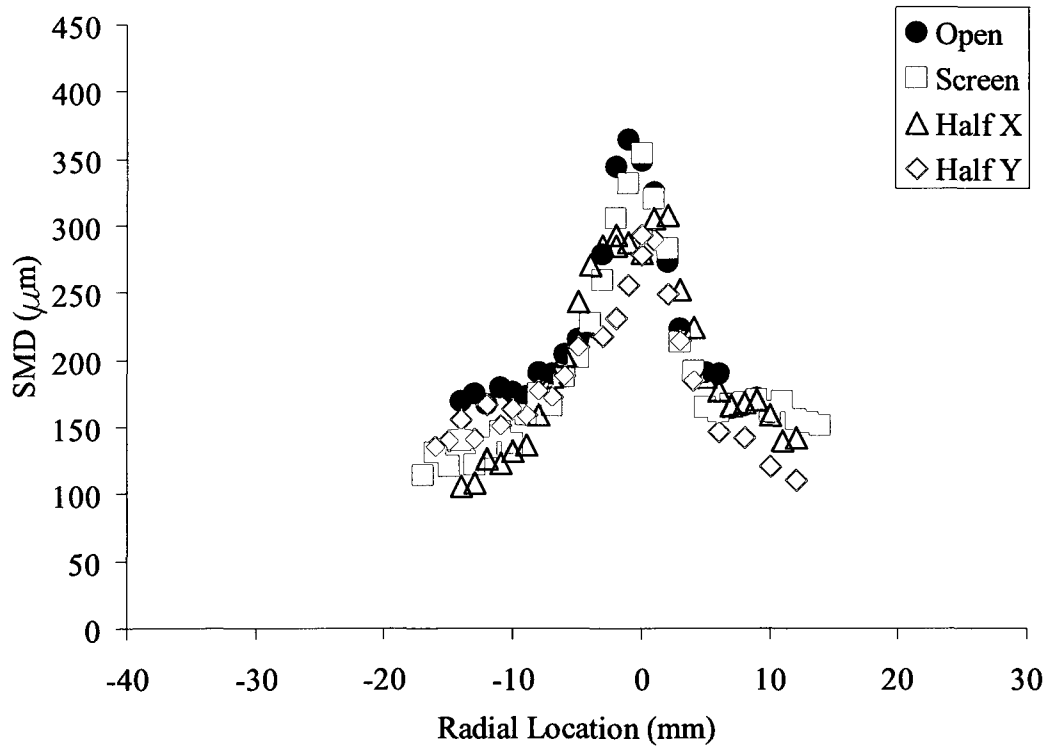

Figure 5.20: Summary average droplet SMD at an axial location of 50 mm measured by PDPA for unobstructed, screen and half obstructed injectors at 19 g/s flow condition.

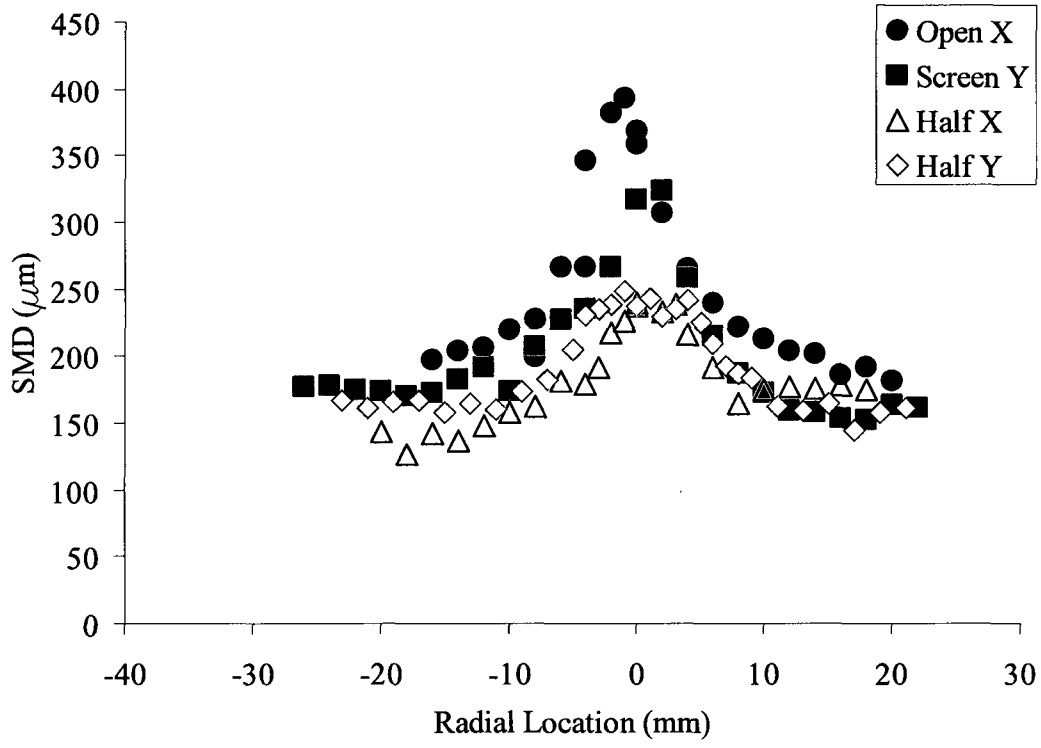

Figure 5.21: Summary average droplet SMD at an axial location of 100 mm measured by PDPA for unobstructed, screen and half obstructed injectors at 19 g/s flow condition.

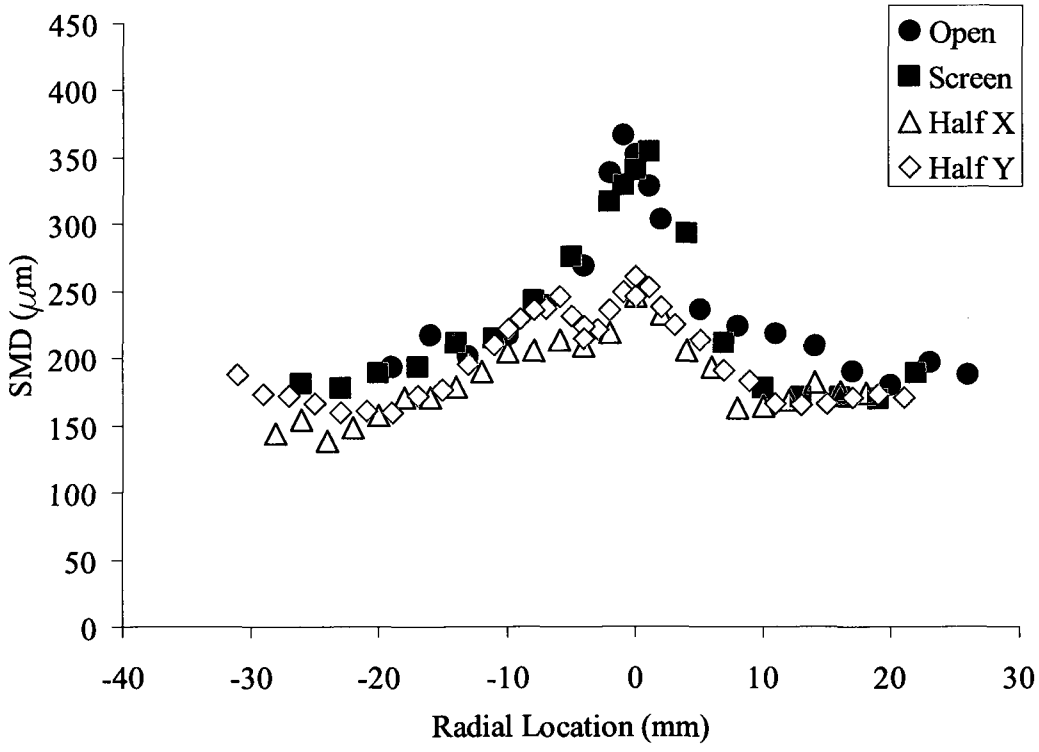

Figure 5.22: Summary average droplet SMD at an axial location of 150 mm measured by PDPA for unobstructed, screen and half obstructed injectors at 19 g/s flow condition.

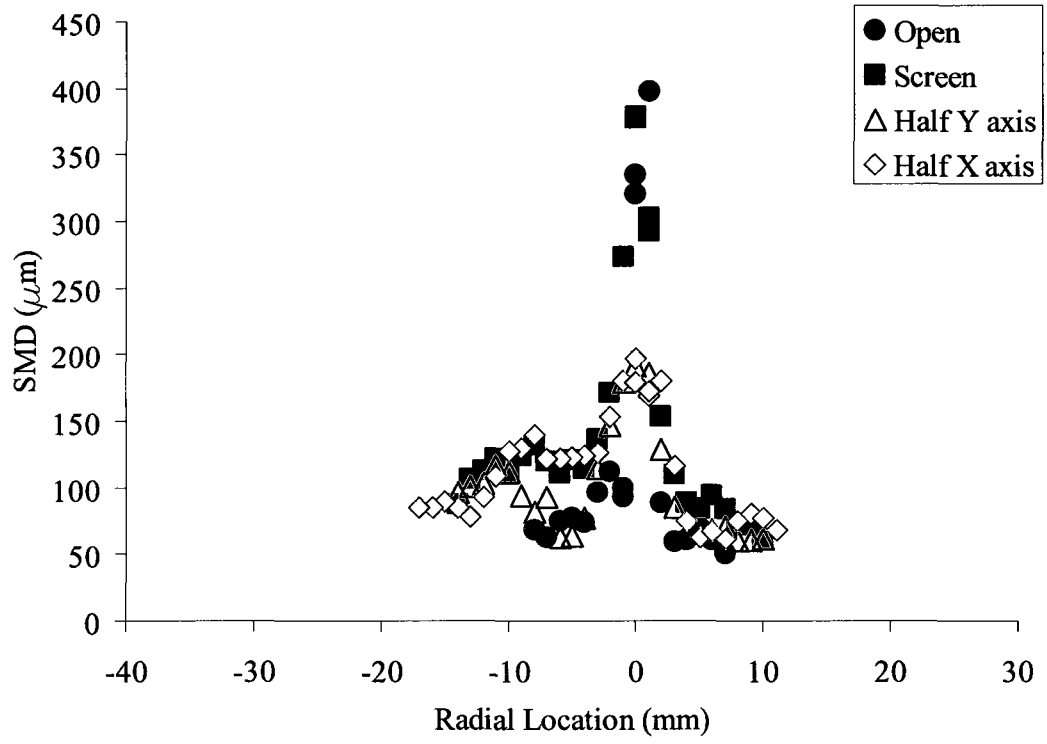

Figure 5.23: Summary average droplet SMD at an axial location of 50 mm measured by PDPA for unobstructed, screen and half obstructed injectors at 29 g/s flow condition.

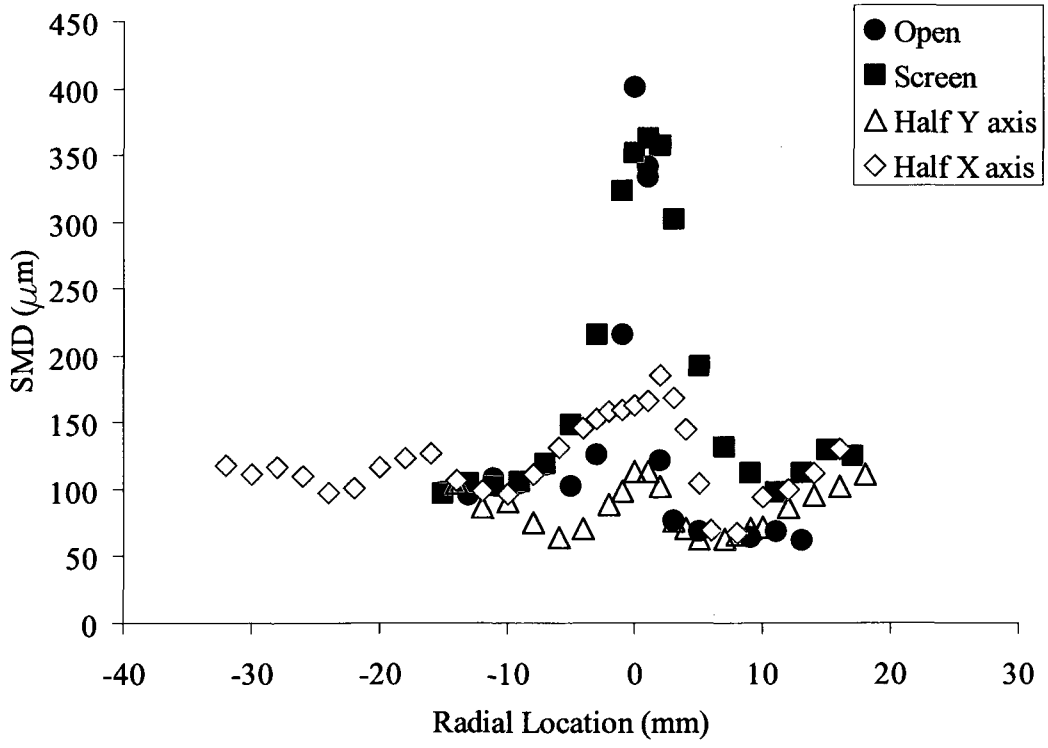

Figure 5.24: Summary average droplet SMD at an axial location of 100 mm measured by PDPA for unobstructed, screen and half obstructed injectors at 29 g/s flow condition.

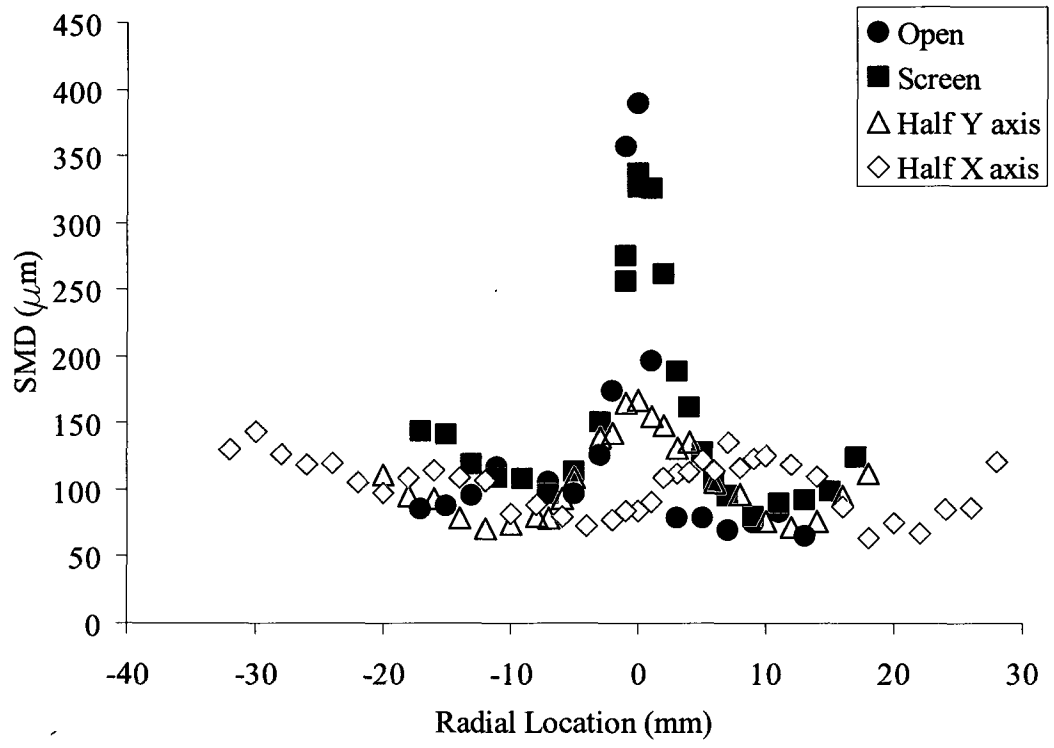

Figure 5.25: Summary average droplet SMD at an axial location of 150 mm measured by PDPA for unobstructed, screen and half obstructed injectors at 29 g/s flow condition.

Several researchers have measured the droplets produced by injectors comparable to the ones used in the present study (Stahl et al., 2006; Tamaki et al., 2000; Kawasara et al., 1992). Unfortunately, it is difficult to compare droplet sizes in different studies, because there are always differences, however slight, in injector geometry, working fluid, diagnostics, measurement locations, as well as countless other factors that could affect the presented results. Within this uncertainty, the data presented in this work correlate well with those by Stahl et al. (2006) and Kawasara et al. (1992). The latter authors used water as the test liquid and a nozzle with a 0.3 mm diameter; using PDPA, they measured an average droplet size of 150 μm at 1500 mm from the nozzle exit.

5.4 Cone Angle

The cone angle 2α is defined in Figure 5.21 (Lefebvre, 2001). Photographic methods are often used for determining cone angle, but there are several complications to this approach. Typically, the cone angle will appear to increase as the camera shutter speed decreases. In addition, the longer the shutter remains open, the noisier the images would become, making their analysis difficult as discoloured pixels could be mistaken for droplets. Furthermore, small droplets at the edge of the spray could go undetected. The lighting choice could also affect the cone angle by failing to illuminate the spray evenly. Lastly, photographic methods will be unable to correctly measure the cone angle of a spray that is not symmetric, unless several photographs are taken from different locations. In order to avoid these problems, the spray cone angle was determined using a combination of the velocity and data rate results collected by PDPA.

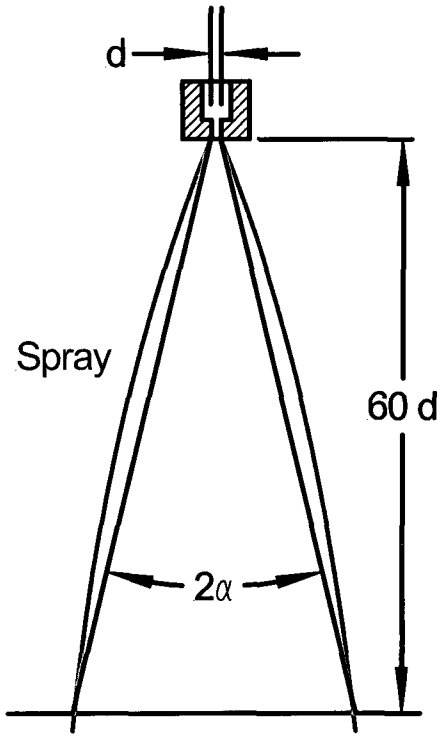

Figure 5.26: Definition of cone angle (Lefebvre (2001)).

Figure 5.22 shows the typical data collection rate of the PDPA as the probe is traversed across the spray. The edge of the spray was determined by a linear extrapolation of the last two points on the curve to a data rate of 1 Hz as shown in Figure 5.22. The edges of the spray were determined at all three planes tested, which were 50, 100 and 150 mm away from the nozzle exit plane. These edges were then used to determine the cone angle at an axial distance of 60 mm by interpolating a parabolic fit to the three measured values. A summary of the cone angle results is shown in Table 5.1.

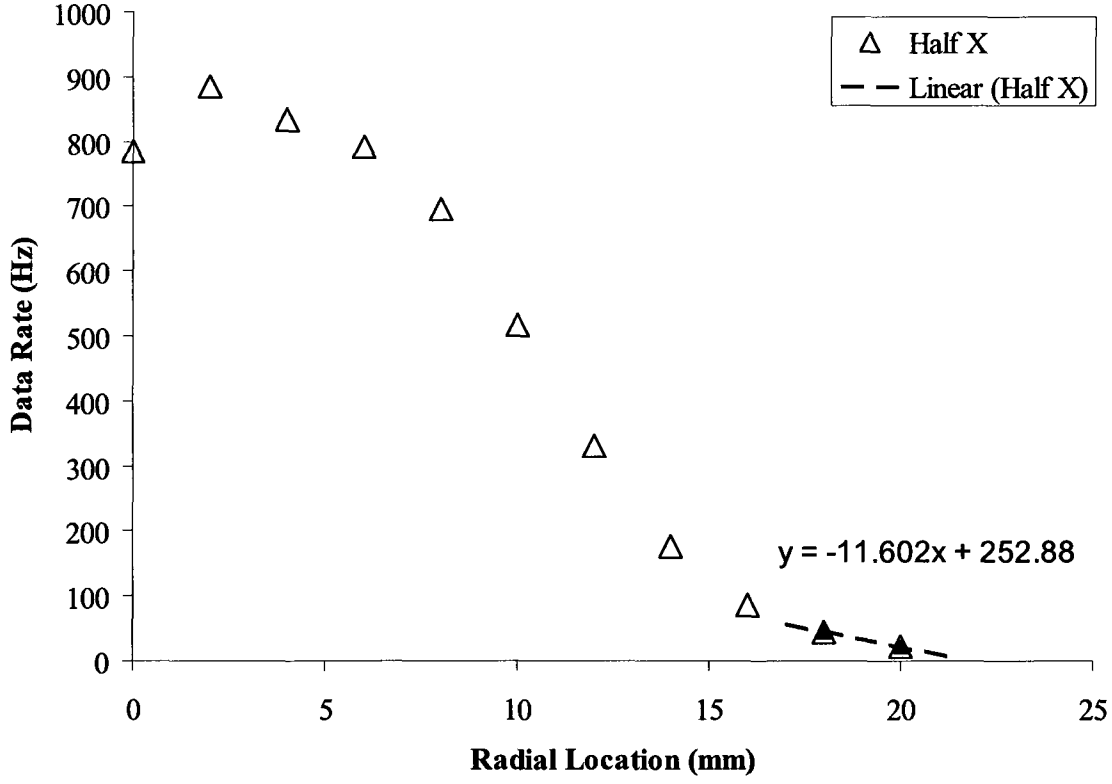

Figure 5.27: Data rate with radial location for PDPA on the half obstructed injector at the 150 mm axial location for the 19 g/s flow condition.

	Flow	19 g/s		29 g/s	
Injector	**Location (mm)**	**X**	**Y**	**X**	**Y**
Unobstructed	**50**	30.67°	32.52°	17.19°	
	100	23.12°	25.74°	16.06°	
	150	16.78°	16.78°	12.07°	
	60	28.91°	31.47°	17.09°	
Screen	**50**	37.01°		28.56°	
	100	29.04°	21.90°	18.02°	
	150	19.53°		13.38°	
	60	35.57°	32.80°	26.05°	
Half	**50**	31.16°	32.77°	32.01°	27.64°
	100	22.69°	26.00°	27.4°	18.73°
	150	18.56°	20.8°	23.3 °	14.69°
	60	31.24°	29.23°	31.04°	25.56°

Table 5.1: Summary of the cone angle measurements 2α.

Several correlations for the spray cone angle of a plain-orifice atomizer have been proposed (Reitz and Bracco, 1979; Abramovich, 1963; Ohrn et al., 1991). Unfortunately none of them takes into consideration the internal flow of the injector or the occurrence of cavitation. The results of the present work correlate well with those of Hiroyasu and Arai (1980), who argue that the spray cone angle is the result of complex interactions between turbulence, discharge coefficient and jet break-up length, which are all affected by the injector geometry and the Reynolds number. Their injector, which had a length to diameter ratio of 10 matching the one in the present work, had spray cone angles of approximately 35° and 20° degrees for flows corresponding to Reynolds numbers 30,000 and 100,000, respectively, which roughly correspond to the flow rates 19 g/s and 29 g/s in the present tests.

Chapter 6 – Conclusions and Recommendations for Future Work

The objective of this study was to examine the effects of different obstructions inserted between the sac and the capillary of a pressure atomizer on its performance. Three configurations were studied in detail, including a screen obstruction, an insert that blocked half of the entrance to the capillary, and an unobstructed injector. Without an obstruction, the flows inside the injector cavitated at low injection pressures. Under these conditions, the location at which the cavitation forms moves with time, and results in an unsteady asymmetrical spray. As the flow rate is increased, the cavitation forms in a more predictable way, and the spray's behaviour also becomes less erratic.

When an obstruction is introduced in the nozzle, there are several changes to the injector's performance. These include the following.

1. A decrease in the discharge coefficient.
2. An increase in the amount of cavitation.
3. An increase in spray cone angle.
4. A decrease in droplet Sauter-mean diameter.
5. An increase in droplet velocity.

The presence of the obstruction also fixes the location where cavitation occurs, making the spray more predictable in shape, but not necessarily symmetrical. The screen obstruction resulted in a more symmetric spray; however, the opposite is true for the half obstruction. This asymmetry becomes more pronounced with an increase in flow rate.

The cavitation was found to occur in 4 different modes depending on the fluid mass flow rate and type of obstruction. These include:

1. Onset of cavitation at the hole inlet due to the obstruction.

2. Onset of cavitation with local separation points.

3. Hydraulic flip, when the flow separates completely from the passage walls.

4. Drastic cavitation that fills the injector with small cavitation bubbles.

The resulting droplets produced by the atomizer were measured at 50, 100 and 150 mm downstream of the nozzle face. Their size was found to decrease as the mass flow increased for all injector designs. The addition of an obstruction reduces the discharge coefficient and thus increases the amount of pressure required to deliver the required amount of fuel. When the sprays from the various injector designs are compared based on mass flow rate, the droplet sizes were comparable, with the half obstruction generating the smallest droplets and the unobstructed nozzle the largest ones. The reduction in droplet size is most significant at the centre of spray. This is a noteworthy result, as it indicates that the obstructions reduce the break-up length of the jet, and are enhancing the atomization.

The obstructed injectors produced smaller droplets but they also required an increase in injection pressure. Equation (2.29) can be used to calculate the diameters of round, unobstructed cavitating injectors that would have the same pressure loss as the obstructed injectors that were tested. Doing so for the test conditions of this study gives orifice diameters of between 0.86 mm and 0.80 mm for the screen and half obstructions, respectively. A useful additional experiment would be to build injectors of this size and compare the sprays that they produce to those of the obstructed injectors. This would

make it possible to determine whether the additional complexity of adding an obstruction to the injector would result in an improved performance by comparison with an unobstructed design that produces the same pressure drop.

The exact mechanism by which atomization is being enhanced is not completely understood. Certainly how the cavitation is formed and develops in the nozzles plays a large role in the spray structure, because for the injectors tested atomization always occurred when cavitation was present. In order to gain a better understanding of how these internal flows and different cavitation modes affect the spray, improved qualitative and quantitative measurements of the flows inside the injector are required. This should include several tests to measure the liquid and gas flows inside the nozzle. Additional high speed photography using reduced exposure times and faster frame rates to better visualize the flow structures inside the injector is needed. Measuring the pressure inside the injector would also be useful in confirming more precisely where cavitation is likely to develop. It is also recommended that future studies match the index of refraction of the working fluid to that of the injector. This will allow for better images of the internal flow structures as well as facilitating the measurement of the velocities and the sizes of the cavities inside the injector.

Void fraction measurements at the exit of the atomizer to determine the actual effective area of the nozzle once the flow has cavitated would be required to better calculate the exit velocity. This could possibly be achieved by doping the liquid with a fluorescent dye and exciting the mixture with the appropriate laser light. Then, one could determine the volume of liquid inside the capillary, by measuring the intensity of the collected light, which would be proportional to the concentration of the fluorescent agent.

In conjunction with the internal flow measurements, information about the region of the spray close to the injector exit is also important in understanding the relationship between the cavitation and the spray that is formed downstream. Gaining some insight as to how the cavitation bubbles exit the injector is of importance as well, in particular, how these pockets of gas affect the core of the emerging jet. This is crucial in understanding the means by which the cavitation improves the jet break-up.

For the present experiment, the various injector designs have different discharge coefficients. As a result, it can not be determined conclusively whether or not the improvement in atomization is simply a result of the cavitation reducing the exit area which causes the flow to accelerate, or by some other means. A future experiment could employ two injectors in which only one is cavitating. The geometries of these nozzles could be selected such that they have the same discharge coefficients and exit velocities despite the very different internal flows. By characterizing the sprays of the two injectors, conclusions could be drawn as to the effect of the cavitation.

References

Abramovich, G. N. (1963). *Theory of Turbulent Jets*. Cambridge, Massachusetts.: MIT Press.

Arai, M., M. Shimizu, and H. Hiroyasu (1985). Break-up length and spray angle for high speed jet. In *Proceedings of the 3rd International Conference on Liquid Atomization and Spray Systems*, London.

Arai, M., M. Shimizu, and H. Hiroyasu (1991). Similarity between the break-up lengths of a high speed liquid jet in atmospheric and pressurized conditions. In *Proceedings of the 5th International Conference on Liquid Atomization and Spray Systems*, Gaithersburg, Maryland.

Baron, T. (1949). Technical report No. 4, University of Illinois.

Berrocal, E. (2006). Multiple scattering of light in optical diagnostics of dense sprays and other complex turbid media. Ph.D. thesis, Cranfield University.

Castelman, R. A. (1931). The mechanism of the atomization of liquids. *J. Res. Natl. Bur. Stand. 6 281*, 369-376.

Chaves, H., M. Knapp, A. Kubitzek, F. Obermeier and T. Schneider (1995). Experimental study of cavitation in the nozzle hole of diesel injector using transparent nozzles. *SAE Paper 950290.*

Chigier, N. (2006). Challenges for Future Research in Atomization and Spray Technology. In *Proceedings of the 10th International Conference on Liquid Atomization and Spray Systems*, Kyoto, Japan.

Dumont, N., O. Simonin and C. Habchi (2000). Cavitating flow in diesel injectors and atomization: a bibliographical review. In *Proceedings of the 8th International Conference on Liquid Atomization and Spray Systems*, Pasadena, California.

Eisenklam, P., and P. C. Hooper (1958). Min. of Supply DGGW Rept. EMR/58/JRL/42.

ElKotb, M. M., M. F. Elbahar, T. I. Sabry, S. A. Wilson (1992). Phase-shift doppler anemometer measurements of diesel spray behavior in open combustion chambers. *Atomization and Sprays 2*, 367-383.

Grant, R.P. and S. P. Middleman (1966). Newtonian Jet Stability. *AIChe J 12 4*, 669-678

Haenlein, A. (1932). Disintegration of a liquid jet. *NACA Tech Memo 659.*

Hall, G. W. (1963) Analytical determination of the discharge characteristics of cylindrical-tube orifices. *Journal of Mechanical Engineering Science 5*, 91-97.

He, L. and F. Ruiz (1995). Effect of cavitation on flow and turbulence in plain orifices for high-speed atomization. *Atomization and Sprays 5*, 569-584.

Hiroyasu, H. (2000). Spray breakup mechanism from the hole-type nozzle and its applications. *Atomization and Sprays 10*, 511-527.

Hiroyasu, H. and M. Arai (1980). Fuel spray penetration and spray angle in diesel engines. *Transactions of the Society of Automotive Engineers Japan 21*, 5 - 11.

Hiroyasu, H., M. Arai, and M. Shimizu (1991). Break-up length of a liquid jet and internal flow in a nozzle. In *Proceedings of the 5th International Conference on Liquid Atomization and Spray Systems*, Gaithersburg, Maryland.

Hiroyasu, H., M. Shimizu and M. Arai (1982). The Break-up of high speed jet in a high pressure gaseous atmosphere. In *Proceedings of the 2nd International Conference on Liquid Atomization and Spray Systems*, Madison, Wisconsin.

Karasawa, T., M. Tanaka, K. Abe, S. Shiga, and T. Kurabayashi (1992). Effect of nozzle configuration on the atomization of steady spray. *Atomization and Sprays 2*, 411-426.

Lefebvre, A. H. (1989). *Atomization and Sprays*. New York, U.S.A.: Hemisphere.

Mahoney, T. J. and M. A. Sterling (1978). The break up length of laminar Newtonian liquid jets in air. In *Proceedings of the 1st International Conference on Liquid Atomization and Spray Systems*, Tokyo, Japan.

McCarthy, M. J. and N. Malloy (1974), A Review of stability of liquid jets and the influence of nozzle design. *Chemical Engineering Journal 7,* 1-20.

Mehta, K. D. (1977). The aerodynamic design of blower tunnels with wide-angle diffusers. *Progress in Aerospace Sciences 18,* 59-120.

Miesse, C. C (1955). Correlation of experimental data on the disintegration of liquid jets. *Industrial Engineering and Chemistry 47 (9)*, 1690-1701.

Nurick, W. H. (1976). Orifice cavitation and its effect on spray mixing. *Journal of Fluids Engineering 98*, 681-687.

Ruiz, F. (1991). A Few Useful Relations for Cavitating Orifices. In *Proceedings of the 5th International Conference on Liquid Atomization and Spray Systems,*Proc. ICLASS-91, pp. 595-602, Gaithersburg, Maryland.

Ohnesorge, W. (1936). Formation of drops by nozzles and the breakup of liquid jets, *Zeitschrift für Angewandte Mathematik und Mechanik 16 (Applied Mathematics and Mechanics 16),* 355-358.

Ohrn, T. R., D. W. Senser, and A. H. Lefebvre (1991a). Geometrical effects on discharge coefficients for plain-orifice atomizers. *Atomization and Sprays 1*, 137-153.

Ohrn, T. R., D. W. Senser, and A. H. Lefebvre (1991b). Geometrical effects on spray cone angle for plain-orifice atomizers. *Atomization and Sprays 1*, 253-268.

Plateau, J. (1873). *Statique Experimentale et Theorique des Liquides Soumis aux Seules Molecularies*, Gauthier-Villars, Paris.

Rayleigh, Lord. (1878). On the instability of liquid jets. *Proceedings of the London Mathematical Society 10 (4).*

Rayleigh, Lord. (1892). The instability of a liquid jet. *Philosophical Magazine 34 (153).*

Reitz, R. (1978). Atomization and other breakup regimes of a liquid jet. PhD thesis, Princeton University.

Reitz, R. and F. V. Bracco. (1979). On the dependence of spray angle and other spray parameters on nozzle design and operating conditions, *Society of Automotive Engineers* Paper 790494

Rupe, J. H. (1962). Jet Propulsion Laboratory Report No. 32-207

Savart F. (1833). Ann. Chim. 53, 337.

Schmidt, D. P. and M. L. Corradini (1997). Analytical prediction of the exit flow of cavitating orifices, *Atomization and Sprays 7.* 603-616.

Smith, S. W. J. and H. Moss (1917) Experiments with mercury jets, *Proc. Roz. Soc A/93.* 373-393 29.

Spikes, R. H. and G. A. Pennington (1959). Discharge coefficients of small submerged orifices. *Proceedings of the Institution of Mechanical Engineers 173.* 661-664.

Stahl, M. B. GnirB, N. Damaschke and C. Tropea (2005). Laser Doppler measurements of nozzle flow and optical characterization of the generated spray, In *Proceedings of the 20th Annual Conference on Liquid Atomization and Spray Systems - Europe,* Orleans, France.

Stahl, M., N. Damaschke, and C. Topea (2006). Experimental investigation of turbulence and cavitation inside a pressure atomizer and optical characterization of the generated spray, In *Proceedings of the 10th International Conference on Liquid Atomization and Spray Systems,* Kyoto, Japan.

Schweitzer, P. H. (1937). Mechanism of disintegration of lquid jets. *Journal of Aplied Physics 8*, 513-521.

Nishida, K., S. Ceccio, D. N. Assanis, N. Tamaki, and H. Hiroyasu (1997). Characterization of Cavitation Flow in a Simple Hole Nozzle. In *Proceedings of the 7th International Conference on Liquid Atomization and Spray Systems,* Seoul Korea.

Tamaki, N., K. Nishida, M. Shimizu, and H. Hiroyasu (1998). Effects of cavitation and internal flow on atomization of a liquid jet. *Atomization and Sprays 8 (2)*, 179-197.

Tamaki, N., K. M. Shimizu, and H. Hiroyasu (2000). Enhanced atomization of a liquid jet by cavitation in a nozzle hole. In *Proceedings of the 8th International Conference on Liquid Atomization and Spray Systems,* Passedena, California.

Tamaki, N., M. Shimizu, and H. Hiroyasu (2001). Enhancement of the Atomization of a Liquid Jet by Cavitation in a Nozzle Hole, *Atomization and Sprays 11 (2)*, 125-137.

Tamaki, N., I. Yoshiaki, and H. Akihiko (2006). Practical study on high-dispersion atomization enhancement nozzle (Effects of ambient pressures on atomization of spray and application to actual diesel nozzle), In *Proceedings of the 10th International Conference on Liquid Atomization and Spray Systems,* Kyoto, Japan.

Tanasawa, Y. and S. Toyoda (1954). Trans Jpn Soc Mech 20, 300.

Tanner, F. (2004). Development and validation of a cascade atomization and drop breakup model for high-velocity dense sprays. *Atomization and sprays 14*, 20–32.

Tavoularis, S. (2005). *Measurements in Fluid Mechanics*. New York, U.S.A.: Cambridge University Press.

Weber, K. (1931). Disintegration of Liquid Jet. Zeitschrift *für angewandte Mathematik und Physik 11 (Journal of Applied Mathematics and Physics 11)*, 136.

Winklhofer, E. (1997). Velocities and structure or atomizing diesel sprays. In *Proceedings of the 13th Annual Conference on Liquid Atomization and Spray Systems – Europe,* Florence, Italy.

Wu, P., R. F. Miranda and G. M. Faeth (1995). Effects of initial flow conditions on primary break up of non-turbulent and turbulent round liquid jets. *Atomization and Sprays 5,* 175-196.

Yoshikawa, Y., T. Kawashima and K. Yanaida (1964). Tohoku Kozan (J. Tohoku Mining Soc. 11, 1964, 37.

Appendix A – Uncertainty Calculations

Uncertainty of the Linear Motion System

Based on a test of the linear motion system the largest bias, *b*, observed for the x, y, and z axies were:

$b_x := 0.065$ $b_y := 0.1$ $b_z := 0.355$

The standard deviation of these biases:

$\sigma_x := 0.019$ $\sigma_y := 0.018$ $\sigma_z := 0.103$

This gives the following precision limits:

$p_x := 2 \cdot \sigma_x$ (A.1)

$p_y := 2 \cdot \sigma_y$ (A.2)

$p_z := 2 \cdot \sigma_z$ (A.3)

So the total uncertainty, u, of the position of the linear motion system for each axis is:

$u_x := \sqrt{b_x^2 + p_x^2}$ (A.4)

$u_y := \sqrt{b_y^2 + p_y^2}$ (A.5)

$u_z := \sqrt{b_z^2 + p_z^2}$ (A.6)

The uncertainty on the relative position, u_{rel}, can be shown to be:

$u_{x\_rel} := \sqrt{2\left(b_x^2 + p_x^2\right)}$ (A.7)

$u_{y\_rel} := \sqrt{2\left(b_y^2 + p_y^2\right)}$ (A.8)

$u_{x\_rel} = 0.106$

$u_{y\_rel} = 0.15$

Uncertainty of Discharge Coefficient

Injector Geometry: do, Ao are the injector diameter and area respectively.

$d_o := 1.1\text{mm}$

$$A_o := \frac{\pi}{4} \cdot d_o^{\,2} \qquad \text{(A.9)}$$

Fluid Properties whereρ, is the fluid density.

$$\rho := 770 \frac{\text{kg}}{\text{m}^3}$$

Biases given by manufacturer for pressure transduce, bp and mass flow meter, bm.

$b_P := 8600\text{Pa}$ $\qquad$ $b_m := 0.000063 \frac{\text{kg}}{\text{s}}$

Sample calculation for the open Injector - 19g/s Flow Condition

Measured mass flow rate and pressure

$P_o := 350754\text{Pa}$ $\qquad$ $m_a := 0.0201 \frac{\text{kg}}{\text{s}}$

Precision of the measurement based on experimental repeatability

$p_P := 1370\text{Pa}$ $\qquad$ $p_m := 0.000071 \frac{\text{kg}}{\text{s}}$

The discharge coefficient calculated at this condition would be

$$C_d := \frac{1}{A_o \cdot \sqrt{2 \cdot \rho}} \cdot \frac{m_a}{\sqrt{P_o}} \qquad \text{(A.10)}$$

$C_d = 0.91$

Partial derivative of discharge coefficient with pressure for precision and bias respe

$$C_{dPp} := -\frac{m_a}{2 \cdot A_o \cdot \sqrt{\rho}} \cdot \left(\frac{1}{\sqrt{P_o^{\,3}}} \right) p_P \qquad \text{(A.11)}$$

$$C_{dPb} := -\frac{m_a}{2 \cdot A_o \cdot \sqrt{\rho}} \cdot \left(\frac{1}{\sqrt{P_o^{\,3}}} \right) b_P \qquad \text{(A.12)}$$

Partial derivative of discharge coefficient with mass flow for precision and bias respectively

$$C_{dmp} := -\frac{1}{A_o \cdot \sqrt{2 \cdot P_o \cdot \rho}} \cdot p_m \qquad (A.13)$$

This give the precision and bias limits as:

$$p_{Cd} := \sqrt{C_{dmp}^{\ 2} + C_{dPp}^{\ 2}} \qquad (A.14)$$

Resulting in a total uncertainty of:

$$u_{Cd} := \sqrt{p_{Cd}^{\ 2} + b_{Cd}^{\ 2}} \qquad (A.15)$$

$u_{Cd} = 0.017$

Uncertainty of Malvern Particle Sizing

The manufacturer quotes the accuracy and precision to be better than +/- 1% of the Dv50, where Dv50 is the droplet size representing half of the volume of the dr population.

The largest Dv50 encountered during the experiment was

$Dv50 := 464.949\mu m$

$b_{Dv50} := 0.01 \cdot Dv50$

$p_{Dv50} := 0.01 \cdot Dv50$

The relationship between the Dv50 and SMD can be determined if the droplet size distribution is known. This is not the case, as the distribution is different from loc to location. However, the Dv50 is always great the SMD. Thus, the uncertainty o the Dv50 will provided a conservative estimate for the SMD.

$$u_{SMD} := \sqrt{b_{Dv50}^{2} + p_{Dv50}^{2}} \qquad (A.16)$$

$u_{SMD} = 6.575\mu m$